Exploring the Dynamics of Red Blood Cell Aggregation in Microcirculation: A Physics and Artificial Intelligence Approach

Dissertation
zur Erlangung des Grades
des Doktors der Naturwissenschaften
der Naturwissenschaftlich-Technischen Fakultät
der Universität des Saarlandes

von
Julie MARTIN-WORTHAM

Grenoble (France)
2023

Tag des Kolloquiums:	21.12.2023
Dekan:	Prof. Dr. Ludger Santen
Berichterstatter:	Prof. Dr. Christian Wagner Prof. Dr. Thomas Podgorski Prof. Dr. Lars Kästner
Weitere Mitglieder:	Prof. Dr. Pavlik Lettinga Dr. Badr Kaoui
Vorsitz:	Prof. Dr. Sabine Rolland

UNIVERSITÄT DES SAARLANDES

Université Grenoble Alpes

THÈSE

Pour obtenir le grade de

DOCTEUR DE L'UNIVERSITÉ GRENOBLE ALPES
et de l'UNIVERSITE DE LA SARRE

École doctorale de Physique
Spécialité : Physique pour les Sciences du Vivant
Unité de recherche : Laboratoire de Rhéologie et Procédés en co-tutelle avec Experimentalphysik

Exploration de la Dynamique de l'Agrégation des Globules Rouges dans la Microcirculation : Une Approche Fondée sur la Physique et l'Intelligence Artificielle

Exploring the Dynamics of Red Blood Cell Aggregation in Microcirculation : A Physics and Artificial Intelligence Approach

Présentée par :

Julie MARTIN-WORTHAM

Direction de thèse :

Thomas PODGORSKI Directeur de recherche, Laboratoire Rhéologie et Procédés, UGA	Co-Directeur de thèse
Christian WAGNER Professeur des universités, Experimentalphysik, UdS	Co-Directeur de thèse

Thèse soutenue publiquement le **21/12/2023**, devant le jury composé de :

Sabine ROLLAND Professeure des universités, Laboratoire 3SR, UGA	Présidente du jury
Thomas PODGORSKI Directeur de recherche, Laboratoire Rhéologie et Procédés, UGA	Co-Directeur de thèse
Christian WAGNER Professeur des universités, Experimentalphysik, UdS	Co-Directeur de thèse
Pavlik LETTINGA Professeur des universités, KU Leuven / Forschungszentrum Jülich	Rapporteur
Badr KAOUI Chargé de recherche, Laboratoire de Biomécanique et Bioingénierie, UTC	Rapporteur
Lars KAESTNER Professeur des universités, Experimentalphysik, UdS	Examinateur

Invités :

Gwennou COUPIER Directeur de recherche, Laboratoire Interdisciplinaire de Physique, UGA	

Université franco-allemande
Deutsch-Französische Hochschule

This thesis was funded by the Franco-German University (UFA), the Centre National de Recherche Scientifique (CNRS) and the University of Saarland (UdS).

Cette thèse a été subventionnée par l'Université franco-allemande (UFA), le Centre National de Recherche Scientifique (CNRS) ainsi que l'Université de la Sarre (UdS).

Diese Arbeit wurde von der Deutsch-Französischen Hochschule (DFH), dem Centre National de Recherche Scientifique (CNRS) und der Universität des Saarlandes (UdS) finanziert.

"There are times in life when people must know when not to let go. Balloons are designed to teach small children this."

Terry Pratchett

Abstract

Exploring the Dynamics of Red Blood Cell Aggregation in Microcirculation: A Physics and Artificial Intelligence Approach

by Julie Martin-Wortham

Examining the characteristics and behavior of red blood cells (RBCs) enables insights into fundamental aspects of blood circulation as well as specific disorders such as sickle cell disease, as observed through the examination of cell shape, or the identification of inflammation or sepsis via the erythrocyte sedimentation rate, a measure closely associated with aggregation rate. Building upon this fundamental and clinical significance, this doctoral work takes a multi-physics approach involving biology, fluid and solid mechanics and computer science, to study the RBCs in flow in capillaries at a microscopic scale.

A first part focuses on the distribution of RBCs at an *in vitro* micro-bifurcation considering the influence of aggregation rates tuned by Dextran. Experimental investigations demonstrate that the presence of aggregation amplifies the non-homogeneous distribution of RBCs, highlighting the significant impact of aggregation forces on the observed Zweifach-Fung effect. These findings enhance our understanding of the complex interplay between aggregation and microvascular flow dynamics.

The second part of this doctoral research addresses the development of a high-throughput automatic shape recognition system for RBCs. A novel digital signal generation and processing approach combining optical spatial amplitude modulation and artificial intelligence is proposed, presenting a concept for an imaging tool capable of capturing RBCs in flow without the need for complex cameras or sophisticated optical setups. By utilizing simple cell fingerprints derived from intensity-modulated signals generated through a 2D binary slit mask, image reconstruction of RBCs in microfluidic flow is achieved.

Overall, the combination, in this PhD, of experimental investigations and innovative imaging techniques provides insights into the behavior of RBCs at a microscopic scale. These findings contribute to the fields of blood rheology, microfluidics, and biomedical research, with implications for the development of improved diagnostic tools and therapeutic interventions.

Résumé

Exploration de la Dynamique de l'Agrégation des Globules Rouges dans la Microcirculation : Une Approche Fondée sur la Physique et l'Intelligence Artificielle

par Julie Martin-Wortham

L'étude des caractéristiques et du comportement des globules rouges (GR) permet de comprendre des aspects fondamentaux de la circulation sanguine ainsi que des troubles spécifiques tels que la drépanocytose, observée par l'examen de la forme des cellules, ou l'identification de l'inflammation ou de la septicémie par le biais de la vitesse de sédimentation des érythrocytes, une mesure étroitement associée au taux d'agrégation. S'appuyant sur cette importance fondamentale et clinique, ce travail de doctorat adopte une approche multi-physique impliquant la biologie, la mécanique des fluides et des solides et l'informatique, pour étudier l'écoulement des GR dans les capillaires à l'échelle microscopique.

Une première partie se concentre sur la distribution des GR à une microbifurcation *in vitro* en tenant compte de l'influence des taux d'agrégation réglés par le Dextran. Les études expérimentales démontrent que la présence d'agrégats amplifie la distribution non homogène des GR, soulignant l'impact significatif des forces d'agrégation sur l'effet Zweifach-Fung observé. Ces résultats améliorent notre compréhension de l'interaction complexe entre l'agrégation et la dynamique du flux microvasculaire.

La deuxième partie de cette recherche doctorale porte sur le développement d'un système de reconnaissance automatique de la forme des GR à haut débit. Une nouvelle approche de génération et de traitement de signaux numériques combinant la modulation d'amplitude spatiale optique et l'intelligence artificielle est proposée, présentant un concept pour un outil d'imagerie capable d'imager des GR en mouvement sans avoir recours à des caméras complexes ou à des configurations optiques sophistiquées. En utilisant des empreintes cellulaires simples dérivées de signaux modulés en intensité générés par un masque 2D binaire à fentes, la reconstruction d'images de GR dans un flux microfluidique est réalisée.

Dans l'ensemble, la combinaison, dans cette thèse, d'études expérimentales et de techniques d'imagerie innovantes permet de mieux comprendre le comportement des GR à l'échelle microscopique. Ces résultats contribuent aux domaines de la rhéologie sanguine, de la microfluidique et de la recherche biomédicale, avec des implications pour le développement d'outils de diagnostic et d'interventions thérapeutiques améliorés.

Zusammenfassung

Erforschung der Dynamik der Aggregation roter Blutkörperchen in der Mikrozirkulation: Ein Ansatz aus Physik und künstlicher Intelligenz

von Julie Martin-Wortham

Die Untersuchung der Eigenschaften und des Verhaltens roter Blutkörperchen (Erythrozyten) ermöglicht Einblicke in grundlegende Aspekte des Blutkreislaufs sowie in spezifische Erkrankungen wie die Sichelzellkrankheit, die durch die Untersuchung der Zellform beobachtet werden kann, oder die Identifizierung von Entzündungen oder Sepsis durch die Erythrozytensedimentationsrate, ein Maß, das eng mit der Aggregationsrate verbunden ist. Aufbauend auf dieser grundlegenden und klinischen Bedeutung verfolgt diese Doktorarbeit einen multiphysikalischen Ansatz, der Biologie, Strömungs- und Festkörpermechanik und Informatik umfasst, um die Erythrozyten in der Strömung in Kapillaren auf mikroskopischer Ebene zu untersuchen.

Ein erster Teil konzentriert sich auf die Verteilung der Erythrozyten an einer Mikroverzweigung *in vitro* unter Berücksichtigung des Einflusses der durch Dextran eingestellten Aggregationsraten. Experimentelle Untersuchungen zeigen, dass das Vorhandensein von Aggregation die inhomogene Verteilung von Erythrozyten verstärkt und den signifikanten Einfluss von Aggregationskräften auf den beobachteten Zweifach-Fung-Effekt hervorhebt. Diese Ergebnisse verbessern unser Verständnis des komplexen Zusammenspiels zwischen Aggregation und mikrovaskulärer Flussdynamik.

Der zweite Teil dieser Doktorarbeit befasst sich mit der Entwicklung eines automatischen Hochdurchsatz-Formerkennungssystems für Erythrozyten. Es wird ein neuartiger digitaler Ansatz zur Signalerzeugung und -verarbeitung vorgeschlagen, der optische räumliche Amplitudenmodulation und künstliche Intelligenz kombiniert und ein Konzept für ein Bildgebungsinstrument vorstellt, mit dem Erythrozyten im Fluss erfasst werden können, ohne dass komplexe Kameras oder ausgefeilte optische Anordnungen erforderlich sind. Durch die Verwendung einfacher Zell-Fingerabdrücke, die aus intensitätsmodulierten Signalen abgeleitet werden, die durch eine binäre 2D-Schlitzmaske erzeugt werden, wird eine Bildrekonstruktion von Erythrozyten im mikrofluidischen Fluss erreicht.

Insgesamt bietet die Kombination aus experimentellen Untersuchungen und innovativen Bildgebungsverfahren in dieser Doktorarbeit Einblicke in das Verhalten von Erythrozyten auf mikroskopischer Ebene. Diese Erkenntnisse tragen zu den Bereichen Blutrheologie, Mikrofluidik und biomedizinische Forschung bei und haben Auswirkungen auf die Entwicklung verbesserter Diagnoseinstrumente und therapeutischer Interventionen.

Acknowledgements

This thesis has been quite the adventure, filled with all sorts of unexpected situations and I have learned a lot from every experience. And thus I would like to express my sincere gratitude to all those who have supported and contributed to the completion of this work. Without their guidance, encouragement, and assistance, this research endeavor would not have been possible. First I would like to thank my two supervisors. Ma profonde gratitude donc à Thomas Podgorski, pour ta précieuse écoute et ta disponibilité, que ce soit sur le plan scientifique ou humain. Tes conseils éclairés et nos échanges fructueux ont été une source inestimable de connaissances, de motivation et de réconfort tout au long de cette aventure. Je me considère extrêmement chanceuse d'avoir pu bénéficier de ta direction éclairée et bienveillante. I am immensely grateful for the guidance of Christian Wagner, of course particularly during my time in Germany. Working under your supervision was incredibly enriching, both in terms of learning the fundamentals and publishing our results.

I have met more people during this PhD than I thought I was socially able to handle, and yet I did not implode. I want to warmly thank all of them. I would not have adapted to life in Germany without the help of my colleagues from Saarbruecken, who made the atmosphere so often pleasant : Asena Abaye, Zakaria Boujja, Revaz Chachanidze, Alexis Darras, Thomas Fischer, Elke Huschens, Thomas John, Alexander Kihm, Oliver Köhn, Karin Kretsch, Sylvain Losserand, Javad Najafi, Steffen Recktenwald, Greta Simionato and Doriane Vesperini. There, I worked in close collaboration with Lars Kaestner and Stephan Quint, whose valuable skills and ambition made the AI cell-builder possible. I extend my gratitude a bit more towards my officemates : Rishab Handa and François Yaya. You helped me open my shell, I could not have possibly joined any after-work drink or coffee talk without you.

Joining the lab in Grenoble during COVID was not easy, but it was worth it a million times. So much that I extended my PhD to stay a bit longer with all my coworkers : Paul Aguirre, François Bergerot, Didier Blésès, Hugues Bodiguel, Frédéric Bossard, Mathilde Challamel, Ana Chitanu, Clément De Loubens, Mai Duong, Teko Ekoué, Nadia El Kissi, Saïd Elmarhoum, Lydia Esteban, Maxime Facon, Eric Faivre, Sylvie Garofalo, Emilie Guilbert, Valentin Hote, Frédéric Hugenell, Louise Infuso, Mohamed Karrouch, Samuel Mandin, Dacil Idaira Yanez Martin, Lorenzo Metilli, Frédéric Pignon, Midhun Puthumana, Béatrice Razafindramangafara, Denis Roux, Xavier Salas Barzola, Emeline Talansier, Olivier Tramis, Khadija Trigui, François Truong, Vincent Verdoot and Alice Vilotte. It was quite incredible to work in place where everyone was always happy to see each other. My colleagues here saw me through the dreadful part of mansucript writing. I alternately shared laughs, cries, despair and confidence with them, and I cannot express the depth of my gratitude. Thank you for your kindness, the little chitchats and the warm welcome each day I picked the office as my writing spot. Ma productivité quotidienne n'aurait pas remercié le fait que je partage mon bureau avec Diego Milan et pourtant il est probable que je ne serais pas arrivé au bout de ma rédaction

sans lui. Que ce soit pour nous distraire mutuellement dans la bonne humeur, pour nous consoler de nos choix de vie qui nous ont ammenés devant ces maudites feuilles blanches à remplir de résultats, ou juste partager ce qui nous venait en tête, je ne regrette aucune seconde de cette plus tellement nouvelle amitié. Il n'y a pas que le LRP dans la vie, je remercie vivement Gwennou Coupier pour ses conseils, son regard neuf sur une soutenance précédemment répétée cent fois et l'agréable expérience d'organiser un colloque sous sa direction.

I would like to express my sincere thanks to Pavlik Lettinga and Badr Kaoui for reviewing this thesis, and to Sabine Rolland and Lars Kaestner for kindly agreeing to serve on my thesis committee.

Je tiens à exprimer toute ma gratitude envers Noémie Aubel et Erika Piras, dont l'aide médicale a été inestimable. Elles ont été une lumière qui guide dans les abysses.

Je souhaite évidemment remercier mes amis qui m'ont aidée à ne pas perdre la tête. Chloé partageait ma douleur, l'a réduite au passage et en prime est venue me soutenir en chair et en os le jour de la soutenance. Amandine et Maude m'ont soutenue et encouragée de loin. Les séances (quasi) hebdomadaires de jeux de rôle avec Jérémy, Antoine, Marc, Valentin et Louis m'ont donné des bouffées de rêve et de rire. L'entrain de Dylan remet toujours du baume au coeur. Flo a un peu joué mon coach de vie et mon éponge à idées noires. Le groupe Lyonnais de la Quarantaine a débarqué par une agréable surprise dans mon quotidien. I would never have reached any confidence in my level of spoken English (and gaming skills) without my friends from the far away land of Eorzea. It is a real delight to chat with all of you, even when we don't play. Ne serait-ce que pour avoir supporté mes sautes d'humeur, mais aussi pour m'avoir encouragée, m'avoir estimée, pour m'avoir écoutée parler l'obscur langage de physicienne, merci Martin.

Enfin, je remercie chaleureusement ma famille : mes grands-parents, mes parents, Laura, qui m'ont toujours soutenue. Je ne me suis jamais sentie complètment seule, malgrès la distance, et c'est grâce à vous que je suis fière de présenter dans ce manuscrit mes travaux.

It was absolutely breathtaking to notice how many of my friends and family joined the videocall for my defense. I hope everyone either learned something or was simply not bored.

Contents

List of Figures

List of Tables

List of Abbreviations

2D	**Two-D**imensional
3D	**Three-D**imensional
ADC	**A**nalog-to-**D**igital **C**onverter
AI	**A**rtificial **I**ntelligence
ANN(s)	**A**rtificial **N**eural **N**etwork**(s)**
BSA	**B**ovine **S**erum **A**lbumine
CDL	**C**ell-**D**epleted **L**ayer
CFL	**C**ell-**F**ree **L**ayer
CNN	**C**onvolutional **N**eural **N**etwork
CTC(s)	**C**irculating **T**umor **C**ell**(s)**
Dex70	**Dex**tran **70** kDa
EFS	**E**tablissement **F**rançais du **S**ang (French blood establishment)
GAN(s)	**G**enerative **A**dversarial **N**etwork**(s)**
Hb	**H**emoglo**b**in
Ht	**H**ematocri**t**
HTFC(s)	**H**igh **T**hroughput **F**low **C**ytometer**(s)**
LASER	**L**ight **A**mplification by **S**timulated **E**mission of **R**adiation
MSE	**M**ean **S**quared **E**rror
OD	**O**ptical **D**ensity
PBS	**P**hosphate-**B**uffered **S**aline
PDMS	**P**oly**D**i**M**ethyl**S**iloxane
PTFE	**P**oly**T**etra**F**luoro**E**thylene
RBC(s)	**R**ed **B**lood **C**ell**(s)**
ROI	**R**egion **O**f **I**nterest
rcf	**r**elative **c**entrifugal **f**orce
UV	**U**ltra **V**iolet
WBC(s)	**W**hite **B**lood **C**ell**(s)**

Units

Symbol	In *Système International* unit	Name	Quantity
°C	[K]	Celsius degree	temperature
b	$[kg \cdot m^{-1} \cdot s^{-2}]$	bar	pressure
Da	[kg]	Dalton	molecular weight
fps	$[s^{-1}]$	frame per second	frame rate
Hz	$[s^{-1}]$	Hertz	frequency
K	[K]	Kelvin	temperature
kg	[kg]	kilogram	mass
L	$[m^3]$	Liter	volume
m	[m]	meter	distance
Osm	[-]	Osmole	osmotic concentration
Pa	$[kg \cdot m^{-1} \cdot s^{-2}]$	Pascal	pressure
rcf	$[m \cdot s^{-2}]$	relative centrifugal force	acceleration
s	[s]	second	time
SPS	$[s^{-1}]$	Sample Per Second	rate

Introduction

Blood is a vital biological fluid that plays a crucial role in maintaining the health and homeostasis of most animal species by transporting oxygen, nutrients, metabolic waste and by regulating temperature. While some aquatic species, such as jellyfishes and corals, do not possess blood or any similar fluid [1], blood in other species can vary greatly in its composition and properties. For example, ice-fish blood is characterized by its low hemoglobin concentration [2], and various animal classes like birds, typically own nucleated red blood cells [3][4]. However, this thesis will focus specifically on human blood and aims to contribute to specific aspects of the understanding of blood properties.

The dynamics and rheology of blood at different scales, from single cell mechanics up to flows in complex vessel networks has been the topic of intense research since the pioneering works of Poiseuille[5] and has attracted a renewed interest in the past decades thanks to the rapid development of new techniques, including microfluidics, numerical simulation and interdisciplinary synergies. Many recent developments focus on the link between red blood cell properties and blood flows at larger scale in healthy and pathological situations. For instance, several pathologies can alter RBC mechanical properties, shape and interactions with direct consequences on their ability to flow through capillary networks to perform their function and on blood rheological properties.

In this work, we focus on two studies aiming at improving our understanding of blood flows in the microcirculation by analysing the influence of RBC aggregation on their distribution in capillary bifurcations as well as proposing new tools for diagnostic purposes thanks to a RBC shape classification and reconstruction technique based on artificial intelligence.

The aggregation of red blood cells (RBCs) is a complex phenomenon that has a significant impact on the fluid dynamics of blood and its ability to transport oxygen and nutrients throughout the body. A first aim of this thesis is to contribute to the investigation of the underlying physical mechanisms of RBC aggregation and how it affects the rheological properties and fluid dynamics of blood, as well as the influence of external factors and aggregate size on the process. More specifically, we focus on the influence of RBC aggregation on the hematocrit separation at capillary bifurcations. Indeed, at the scale of small vessels (capillary networks), it is well known that the distribution of RBCs is not homogeneous, which has consequences on oxygen transport and availability for instance. As it is suspected that RBC aggregation may increase

these heterogeneities. This thesis provides a first quantitative assessment of this phenomenon.

The second aspect of this work takes advantage of the rapid development of Artificial Intelligence (AI) techniques in the domain of image and signal processing to set up a rapid and efficient flowing cell classification technique and image reconstruction that could form the basis of a new flow cytometry principle. It focuses on the shape of RBCs flowing in capillaries, which is itself a marker of their mechanical properties and may reveal pathological situations.

This manuscript is organized as follows : it will begin by providing a background on blood, including its properties as a non-Newtonian fluid, its general behavior, and the various components that make it up. The focus will then shift to RBCs, which are essential for oxygen transport and play a key role in the aggregation process. This chapter will also cover the phenomenon of aggregation and its impact on blood circulation and microcirculation, which is of particular interest in the study of microfluidics. The next part of this chapter will delve into the field of microfluidics, which involves the study of fluid flow at the microscale. This includes the analysis of flow dynamics in small channels, the behavior of suspensions of particles and microflow, and the effect of migration and cell-free layers on the distribution of RBCs. The chapter will also cover the Fahraeus effect, which is the phenomenon of a decreased RBC concentration in the outer layer of a blood vessel due to the decrease in radius, and its impact on bifurcation.

The following chapter will focus on the distribution of aggregated RBCs at a microbifurcation. This study will involve the use of chip design and fabrication, blood sample preparation, and an experimental setup to measure the flux and velocity of RBCs. The results will be compared with and without aggregation and will take into account the influence of large and small vessels, as well as the plasma skimming effect. The chapter will also discuss the equilibrium position of RBCs in a microchannel and the impact of shear rate on the distribution.

The final chapter of the thesis will cover the use of image and signal processing with artificial intelligence to recreate pictures of red blood cells from a 1D signal. This will involve the use of convolutional neural networks (CNN), image processing techniques, and the training of an artificial neural network to classify and reconstruct RBC images. The chapter will cover the characterization of RBCs based on their shape, length/width ratio, and light reflection and absorption properties. The study will also simulate the use of a single photosensor to capture RBC images, and the use of a mask for classification and image reconstruction. The results will be analyzed and compared with different mask patterns, and the quality of the reconstructed images will be assessed using image classification. The conclusion will summarize the findings of the study and discuss future perspectives, such as the use of generative adversarial networks (GANs) and the construction of a more advanced experimental setup.

Through this research, we hope to gain a greater understanding of this vital biological fluid and its potential to improve human health and well-being. Overall, this thesis aims to better understand the aggregation of red blood cells and its impact on the distribution of RBCs in microcirculation, as well as to develop a method to recreate images of RBCs using artificial intelligence. The research will involve a combination of biology, physics, and computer science to provide a comprehensive understanding of the subject matter. The results of this research have the potential to contribute to the development of new diagnostic and therapeutic tools for blood disorders such as sickle cell anemia and thrombosis.

Chapter 1

Background

1.1 Blood

The human body contains a vast network of blood vessels that transport blood throughout the body, carrying oxygen and nutrients to the body's tissues, removing metabolic waste products and regulating body temperature. The total volume of blood in a human body can be estimated at around 70 mL/kg for men and 65 mL/kg for women [6]. Blood is composed of a liquid phase called plasma, which contains dissolved ions, hormones and proteins, and a cellular phase, which consists of red blood cells, white blood cells and platelets.

Red blood cells, also known as erythrocytes, are responsible for carrying oxygen from the lungs to the tissues and carbon dioxide from the tissues to the lungs. They contain a protein called hemoglobin, which binds to oxygen and gives blood its characteristic red color. White blood cells, or leukocytes, are involved in the immune system and play a key role in fighting infections and diseases. Platelets, also known as thrombocytes, are essential for blood clotting and hemostasis.

The rheology of blood, or its flow properties, is of particular interest in the field of medicine and physiology. The viscosity, or resistance to flow, of blood plays a crucial role in the circulatory system, with abnormal viscosity levels being associated with various health conditions such as cardiovascular disease and blood disorders. Additionally, the rheology of blood can also provide important insights into the micro-mechanics of blood flow at the cellular level, which is useful in the development of medical devices such as artificial heart pumps.

In this chapter, we will delve deeper into the intricacies of human blood, examining its composition, properties and functions in detail. Through this research, we hope to gain a greater understanding of this vital biological fluid and its potential to improve human health and well-being.

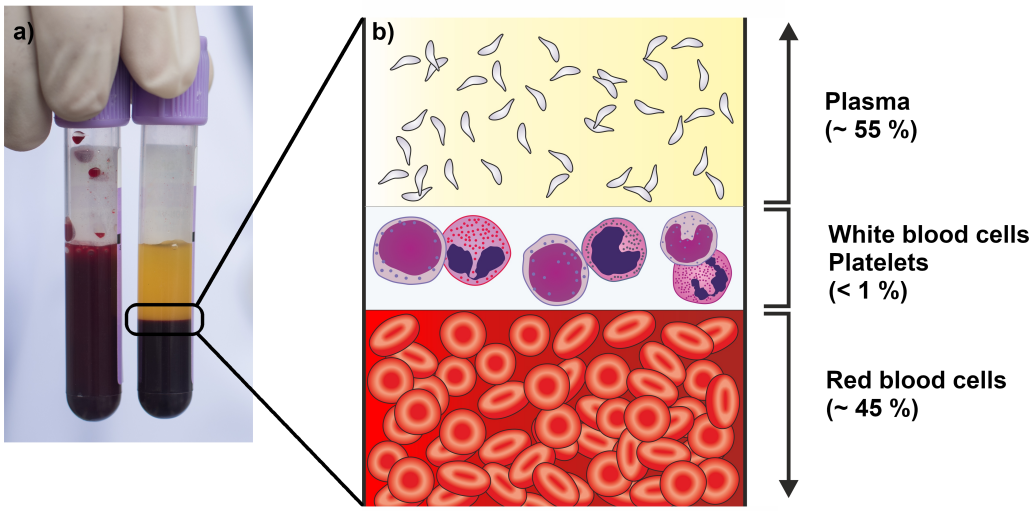

Figure 1.1: Centrifuged blood. a) Comparison of a blood sample before (left) and after (right) centrifugation. b) After centrifugation, the supernatant is the plasma, containing proteins, the pellet is composed of the red blood cells and the layer at the interface is called the buffy coat and contains the white blood cells and the platelets.

1.1.1 Blood composition

Plasma

More than half of the total volume of human blood is comprised of plasma (Figure 1.1), which mainly consists of water, accounting for approximately 90 % of its composition. Plasma is a crucial component that carries a wide range of proteins, nutrients, and hormones. The primary protein found in plasma is albumin, present at concentrations ranging from 35 to 50 g/L. Albumin plays a key role in maintaining the colloid osmotic pressure of the plasma, which helps regulate fluid balance in the body at around 25 mmHg [7][8], corresponding to an osmolality at 290 mOsm/kg. Additionally, albumin acts as a transporter for various substances, including fatty acids, hormones and drugs [9].

Globulins, the second most prominent protein family, are present in the plasma at concentrations between 30 and 45 g/L [8]. Apart from their function as carriers for other proteins, globulins also contribute to immune system responses [10].

Fibrinogen is another relevant protein, within the range of 1.5-4 g/L in plasma at physiological concentration and is the main factor of aggregation of the red blood cells [11][12]. It is also an important ingredient in coagulation processes that involve the formation of fibrin clots.

The plasma maintains a balanced pH of around 7.4 due to the presence of ions. Additionally, the plasma density is approximately 1030 kg/m^3.

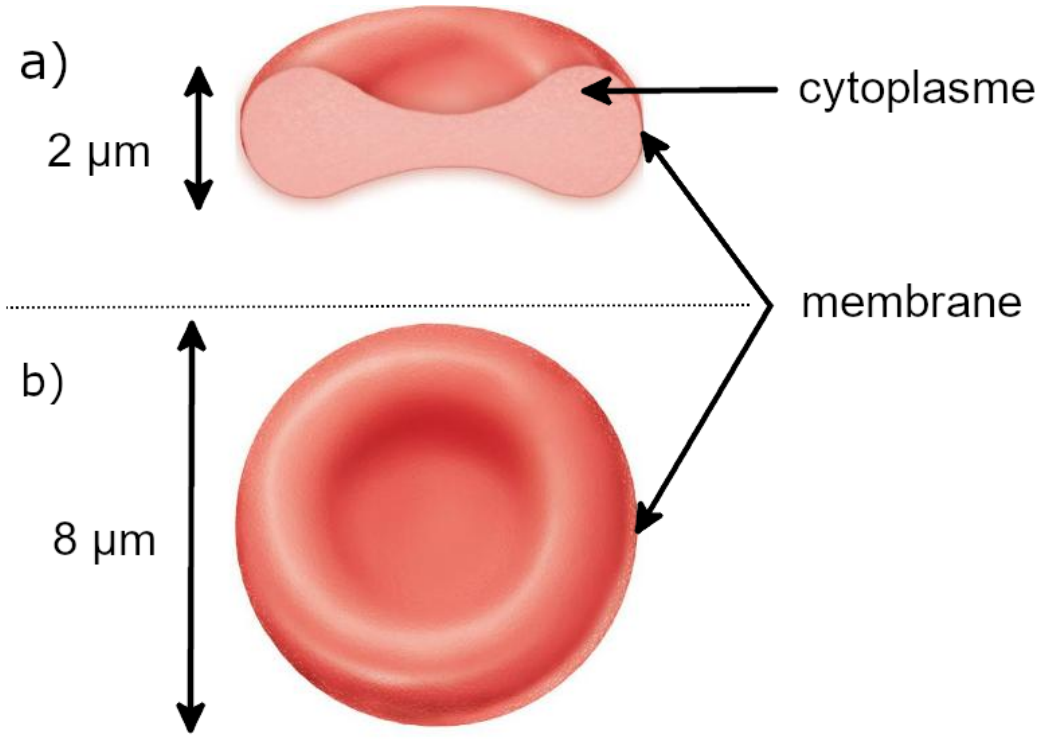

Figure 1.2: Illustration of a RBC shape at rest; a) cross-section of a side view; b) overhead view

Red blood cells

The hematocrit is the volume ratio of erythrocytes, or red blood cells (RBCs), in blood. The average hematocrit ranges from 41% to 50% for men and from 36% to 48% for women. In human blood, the main elements of mature RBCs are their cytoplasm and their membrane. The cytoplasm contains the hemoglobin, the oxygen-transport protein responsible of the red color of the blood. The membrane of the RBCs is a complex structure. The proteic cytoskeleton supports a lipid bilayer around which the glycocalyx (the pericellular matrix) is located. At rest, an RBC has a biconcave shape with a diameter of approximately 8 µm and a width of 2 µm (Figure 1.2). This singular shape is the result of its volume, around 90 pL, the surface of its membrane, about 136 μm^2, and the membrane elasticity. It especially increases the gas exchanges between the inside of the RBC and its surroundings and thus helps the transport of CO_2 and O_2. As a first approximation, the RBC membrane can be considered inextensible/incompressible, however its ability to bend and the deflated shape of RBCs make them highly deformable, allowing them to go through the capillaries, which can be narrower than the RBC's diameter.

Other elements

The remaining blood components represent less than 1 % of the blood volume. The leucocytes, the family of the different white blood cells, circulate through the body via both the blood and the lymphatic systems and are part of the

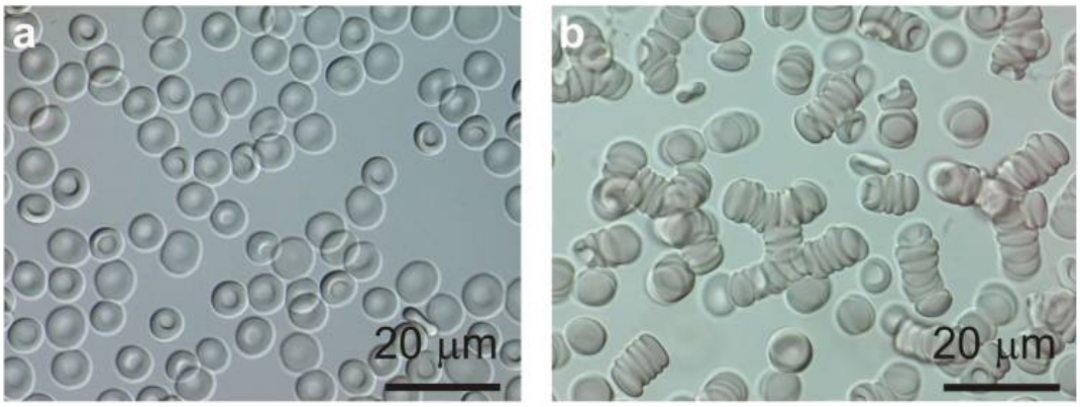

Figure 1.3: Image of RBCs (a) in a buffer solution (b) forming rouleaux in a 20 mg/ml dextran solution in a Petri dish. Reprinted from Brust, Aouane, Thiébaud, *et al.* [13].

immune response. The thrombocytes, more commonly known as platelets, are vesicles that ensure coagulation.

1.1.2 General rheological behavior of blood

Most of the models consider in the vascular system that plasma alone behaves essentially like a Newtonian fluid, meaning it follows Newton's law of viscosity :

$$\tau = \mu \times \dot{\gamma} \tag{1.1}$$

where τ is the shear stress, $\mu = 1.20$ mPa.s the estimated viscosity of plasma at 37 °C and $\dot{\gamma}$ the shear rate. However viscoelastic properties of the plasma have been highlighted due to the presence of certain proteins [14][15] at high shear rates, that can be reached in the microvascular network.

Additionally, the presence of cells in the plasma at high concentration will obviously affect the hemorheology at both macroscopic and microscopic scales. Thus, the behavior of blood at high shear rates (of the order of $\dot{\gamma} = 100$ to 1000 s^{-1}, in vessels highly bigger than the cells like arteries or veins, can still be assumed as Newtonian, but with a modified viscosity of $\mu = 3$ to 4 mPa.s [16].

However, as RBCs are highly deformable particles that can also form aggregates as we shall see below, blood is actually a non-Newtonian fluid with a strong shear-thinning behavior, as long as we consider flow in confined channels or lower shear rates (<100 s^{-1}), as first quantified by Chien [17] (Figure 1.4).

1.2 Aggregation

RBCs tend spontaneously to form clusters in a stack shape, called rouleaux (Figure 1.3). The stacks can organize themselves to build a network. The

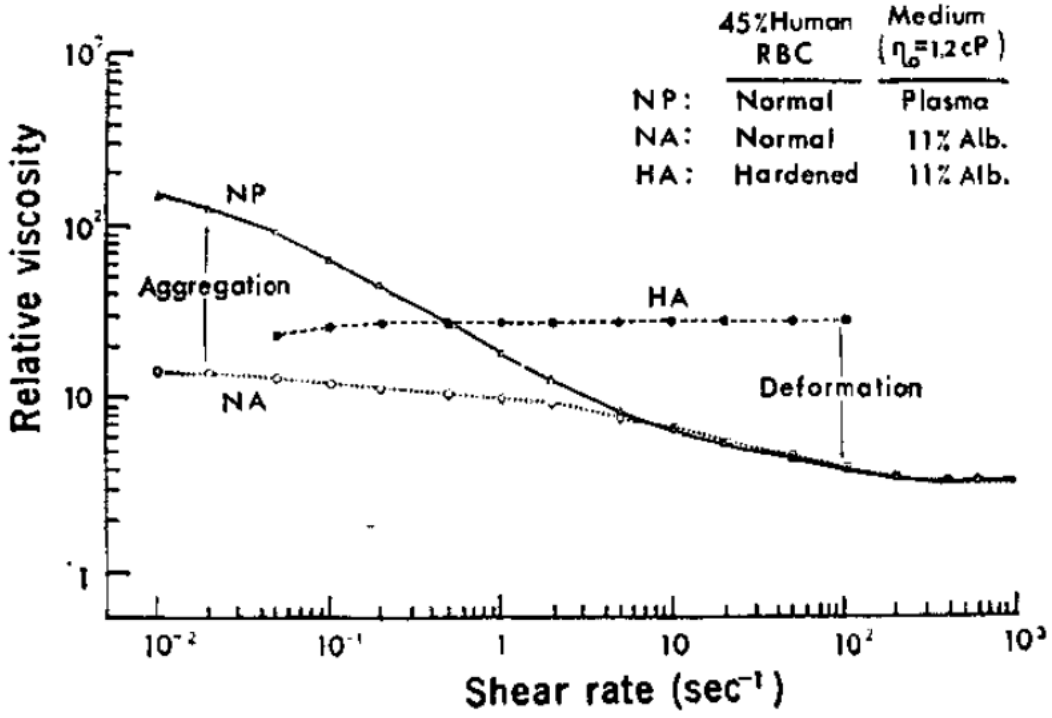

Figure 1.4: Comparison of viscosity of RBC suspensions at 45 % Ht, normalized by plasma viscosity, as a function of the shear rate, for RBC suspended in plasma (normal blood, NP), in 11 % albumin (without aggregation, NA) and glutaraldehyde-stiffened RBCs in albumin (HA). Reprinted from Chien [17].

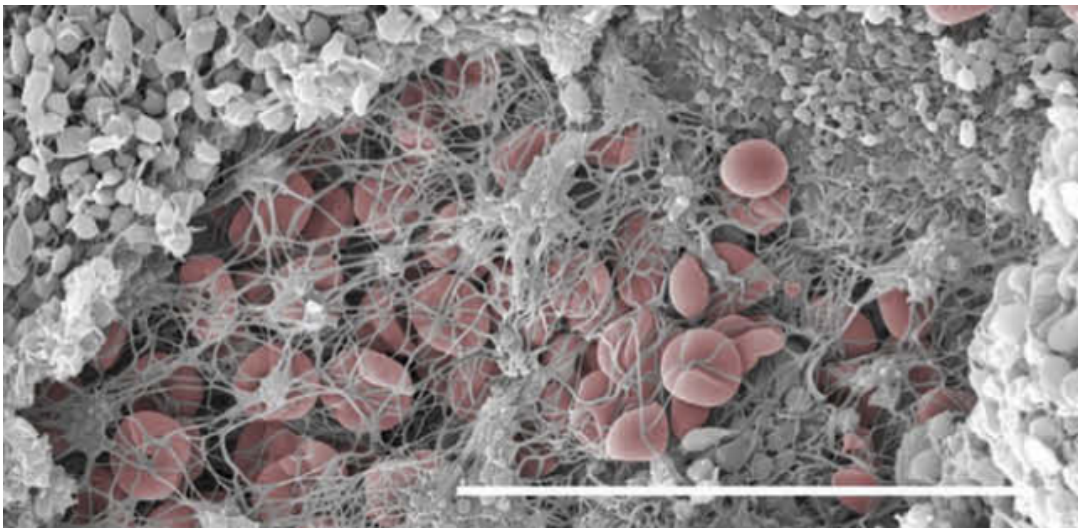

Figure 1.5: Scanning electron microscopy image of a thrombus. RBCs are pseudo-colored in red. Scale bar is 30 µm. Reprinted from Tomaiuolo, Litvinov, Weisel, *et al.* [18]

aggregation index (which can be defined, for instance, as the fraction of aggregated cells) varies according to numerous parameters, such as species, individual, position in the circulatory system, state of health, etc. This phenomenon is fundamentally different from coagulation. On one hand, coagulation is the formation of a blood clot (Figure 1.5, or thrombus, an unorganized cluster of RBCs and platelets in a fibrin network (a fibrous protein obtained from the fibrinogen polymerization). Coagulation is an irreversible phenomenon.

On the other hand, aggregation is entirely reversible, involves only interactions between RBCs and is largely the result of the presence of fibrinogen, although other proteins in plasma can influence lightly the aggregation index. It occurs at low shear-rate and when hydrodynamic stresses that tend to dissociate RBC clusters are sufficiently low. The aggregation index is often measured in medical blood tests by observing the sedimentation rate of RBCs, rouleaux falling faster than single RBCs. It is often, but not systematically, correlated to a high level of fibrinogen and is generally considered a non-specific indicator of inflammation.

Aggregation is considered as the principal cause of the shear-thinning behavior of blood as shown in Figure 1.4. The network of rouleaux created at very low shear-rate increases the viscosity and when the network then the rouleaux themselves are broken, as the shear rate increases, the viscosity decreases.

1.2.1 Models of aggregation

Several studies have been leaded to understand and characterize the underlying aggregation mechanisms. The two main identified mechanisms, which are not mutually exclusive, are bridging and depletion. The two models rely

on the presence of macro-molecules surrounding the RBCs. In blood, this macro-molecule is the fibrinogen, but for studying purpose, the use of Dextran as a model molecule has been investigated since the beginning of the century. Dextran can be produced with different molecular weights thus allowing a better understanding of the models of aggregation. The relation between aggregation and concentration in Dextran presents in this case a bell-shape curve (Figure 1.6 (left)), reaching a maximum at an optimal concentration of Dextran, depending on its molecular weight. With fibrinogen, the variation of the interaction energy with concentration is more monotonous in the physiological range ($1.5 - 4$ g/L) but also exhibits a bell-shaped behavior at higher concentrations which are more difficult to reach due to solubility limitations [13], [19], [20] (Figure 1.6 (right)).

Bridging consists on the adsorption of macro-molecule on the RBCs membrane, physically linking the RBCs together. There is no consensus on whether the binding is specific [21][22] or not [23]. There are then two theories on the source of the bell-shape. The first, presented by Jan and Chien [21], considers the electrostatic repulsive force. It increases when more Dextran is adsorbed on the cells' membrane until it counteracts the binding force. The second explanation relies on the limited binding spots available on the RBC membrane. Once the surface is saturated, it cannot bind with the macro-molecules present on another RBC, assuming there is no steric interaction between the macro-molecules.

The second model, known as depletion, arises from the difference in osmotic pressure created by the exclusion of macro-molecules around the immediate vicinity of RBCs [24]. To illustrate this concept in a simplified manner, we can consider a basic model where both macro-molecules and RBCs are seen as non-deformable spheres. When two RBCs approach each other closely, the surrounding medium lacks sufficient space for the Dextran molecules, resulting in a disparity in osmotic pressure. This difference in pressure tends to keep the RBCs in close proximity to each other, thereby contributing to the aggregation phenomenon. More refined models have been developed, based on the shape of the molecules and the cells [25] or the partial penetration of the Dextran into the glycocalyx [26].

1.2.2 Blood circulation

Circulatory system

The cardiovascular system is a complex network of vessels of different sizes from a few µm up to a cm or more in diameter. Figure 1.7 (left) illustrates its different parts : the pulmonary circulation from the right heart to the lungs and then to the left heart to release carbon dioxide and oxygenate the RBCs, and the systemic circulation from the left heart to rest of the body and then to the right heart to irrigate the different organs, delivering oxygen and collecting carbon dioxide. A RBC travels the whole loop in a minute on average.

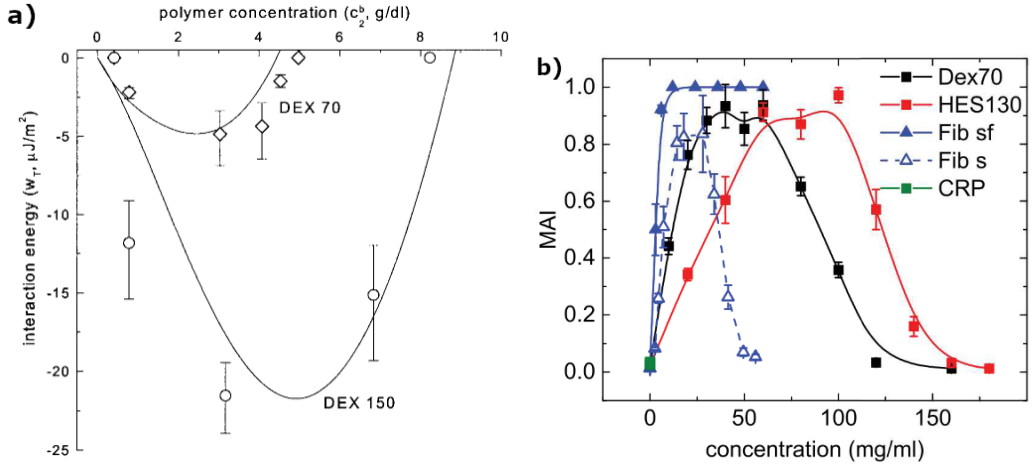

Figure 1.6: a) Comparisons between calculated (solid lines) and experimental (data points from Buxbaum, Evans, and Brooks [27]) values of interaction energy (w_T) for RBC suspended in various concentrations of Dextran 70 kDa or Dextran 150 kDa. Reprinted from Neu and Meiselman [28]. b) Microscopical aggregation indice versus the concentration of macromolecule; Dextran 70 kDa (black curve), HES 130 kDa (red curve), saltfree (filtered) Fibrinogen (blue, filled triangles), Fibrinogen as delivered by Sigma Aldrich with approx. 40 % salt (empty triangles) and C-reactive protein (green). Error bars represent the standard deviation of measurements for at least three healthy donors. Reprinted from Flormann [20]. Lines are guides to the eye.

The oxygenated blood goes through the arteries then the arterioles and the capillaries. In the capillary network occur the gaseous exchanges, the deoxygenated blood then goes through the venules and finally the veins to reach the left heart. The network including arterioles, capillaries and venules is called the microcirculatory system (Figure 1.7 (right)). It is a complex network, very asymmetrical, consisting in a succession of bifurcations and junctions.

The vessels within the macrocirculatory system exhibit diameters ranging from millimeters to tens of millimeters, in stark contrast to the microcirculation, where vessel diameters are on the order of ten microns (Figure 1.8). In smaller vessels, blood cannot be considered a homogeneous fluid as in large arteries and veins and its cellular nature has to be taken into account. This substantial difference in size leads to distinct characteristics of the blood flow, depending on the specific segment of the circulatory system under consideration. Considering the Reynolds number and the Womersley number is an effective approach to analyze the predominant forces in each case.

Reynolds number Re quantifies the predominance of the inertial forces over the viscous forces, with $Re = \rho.u.w/\mu$ where w is the diameter of the vessel, $\rho = 1060\ kg \cdot m^{-3}$ is the density of the blood, $\mu \approx 3$ mPa.s is the viscosity of blood and u is the characteristic velocity of the flow. In the macrocirculation, $Re > 150$ while in microcirculation $Re < 0.75$, which means the flow follows the laws of microfluidics as we shall detail below.

Womersley number α is used to characterize a pulsatile flow, where $\alpha = w/2 \cdot (\omega\rho/\mu)^{1/2}$, where $\omega = 20\ rad.s^{-1}$ is the pulsation for a pulse of 60 beats per

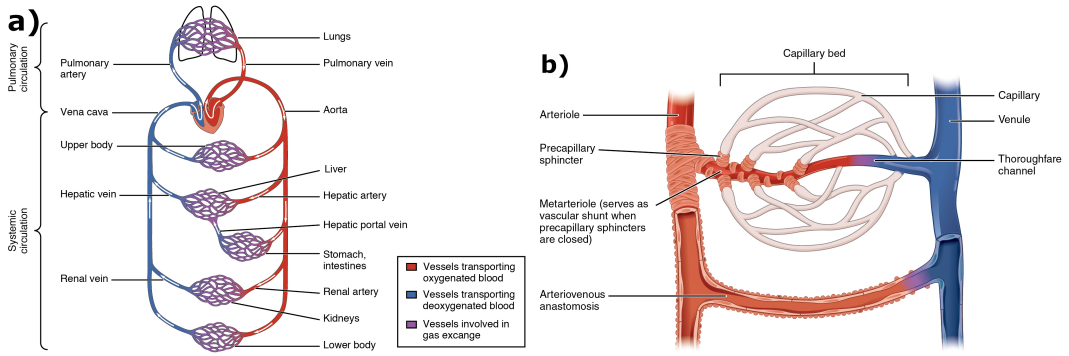

Figure 1.7: Illustration of a) the cardiovascular system and b) focus on a part of the microvascular system. Blue represents the deoxygenated blood and red the oxygenated blood. Illustrations from Anatomy & Physiology, http://cnx.org/content/col11496/1.6/, Jun 19, 2013.

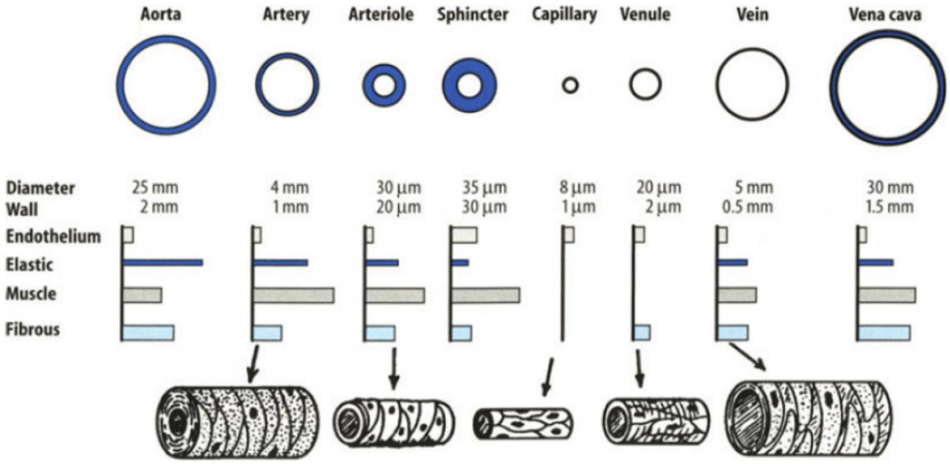

Figure 1.8: Main characteristics of the different vessels in the blood circulatory system. Reprinted from Lim H. W., Wortis, and Mukhopadhyay [30].

minute [29]. While the flow is highly pusatile in veins and arteries ($\alpha > 3$) due to heart beats, it is widely attenuated in microcirculation ($\alpha < 0.03$) and is generally overlooked.

Microcirculation and specificities

In general, the blood flow in microvessels can be considered as laminar as there are few sources of turbulence and because of the predominance of viscosity forces (as the Reynolds number is low, in most cases flows in the microcirculation are considered to be governed by the Stokes equation and inertia is neglected . However punctual events can interfere, like the passage of a white blood cell (WBC) through a capillary, although they are much less common than RBCs. As explained previously, the WBCs are bigger than RBCs and by flowing through capillaries smaller than them, the flow resistance will temporarily increase. In slightly bigger vessels, a phenomen of margination of the

WBCs has been observed and its implications has been studied in the work of Chachanidze [31]. That being said, we generally consider the steady-state flow.

Poiseuille flow In this case, Poiseuille Sutera and Skalak [32] established one of the principal laws of microfluidics for a flow in a cylindrical tube :

$$Q = \frac{\pi R^4}{8l\mu}\Delta P \tag{1.2}$$

where Q is the volumetric flowrate, R the radius of the tube, l the length of the tube, μ the dynamic viscosity of the fluid and ΔP the pressure difference between the two ends of the tube, and its derivative establishing the well-known parabolic profile of velocity :

$$u(r) = \frac{G}{4\mu}\left(R^2 - r^2\right) \tag{1.3}$$

where r is the distance from the center of the tube in a cross-section, and $G = \Delta P/l$.

This law is only valid for a Newtonian fluid and therefore can describe the behavior of blood in the bigger vessels as stated previously but in microcirculation it can only describe the carrier fluid, plasma with no suspended particles.

Migration and Fåhræus effect Due to hydrodynamic interactions between the vessel wall and the cells, the distribution of RBCs in a cross-section is not uniform. The RBCs tend to migrate toward the center of the vessel, creating a zone close to the wall without cells called the cell-free layer (CFL) or cell-deplated layer to consider the few cells that can punctually be there. A direct consequence of this distribution, combined with the parabolic velocity profile, is that the velocity of the RBCs will be higher than the average velocity of the fluid. As a consequence of mass conservation (both plasma and RBC fluxes must be conserved),Fåhræus [33] then observed that the hematocrit in microcirculation, H_t, is lower than the inlet hematocrit in macrocirculation, called discharge hematocrit H_D (Figure 1.9), where the distribution of cells is quasi-homogeneous. An empirical relation has been established by Pries, Secomb, Gaehtgens, *et al.* [34], where the size of the vessel intervenes in the H_T/H_D ratio.

Fåhræus-Lindqvist effect Fåhræus and Lindqvist [35] established that, due to the existence of the CFL, the apparent viscosity of blood is lower in microcirculation than in macrocirculation. The apparent viscosity of blood is defined through the Poiseuille law of Equation 1.2 as the viscosity of an equivalent Newtonian fluid that would exhibit the same flow rate to pressure ratio. This observation was then confirmed in multiple studies, summarized by Pries, Neuhaus, and Gaehtgens [36] (Figure 1.10). The qualitative explanation is

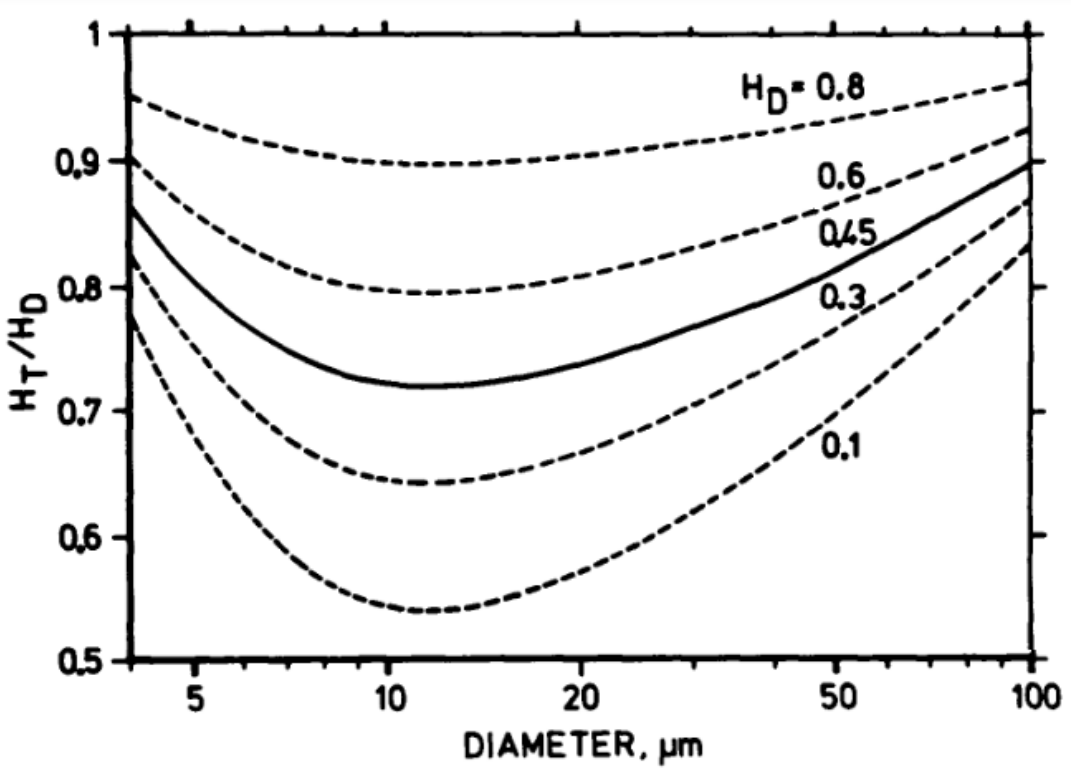

Figure 1.9: Fåhræus effect : ratio between the inlet hematocrit H_D and the hematocrit in the tube H_T as a function of the tube diameter. Reprinted from Pries, Secomb, Gaehtgens, *et al.* [34].

that the CFL acts as a lubricant, reducing the apparent viscosity. However in capillaries smaller than 5 µm, RBCs, bigger than the diameter, squeeze into the vessel and there is no CFL, which results in a sudden increase of friction and apparent viscosity.

Bistability of RBCs in flow

As previously stated, the RBCs are highly deformable, which leads to specific behaviors in microcirculation. Considering a straight channel, depending on the confinement and the shear rate, several shapes and behavior have been observed and simulated (Figure 1.12 (a)). In a specific range of constriction levels (between 0.4 and 0.75), which is the ratio between the diameter of the capillary and the diameter of the cell, and shear rate [37] a phenomenon of bistability occurs (Figure 1.11).

Indeed, from the various shapes an RBC can take, two are predominant : the slipper and the parachute shapes (Figure 1.12 (b)). Slippers are highly asymmetrical and are off-centered of the channel. They are characterized by a rounded head at the front of the RBC and an off-centered tail. They appear at high velocities. In the case of a 10×12 µm channel [39], or a 10×8 µm channel (Figure 1.12), they are dominant at 5 mm/s and higher velocities. Parachutes are, on the opposite, symmetrical and positioned in the center of the channel. They have a parabolic head, with a cavity behind. When the cross-section

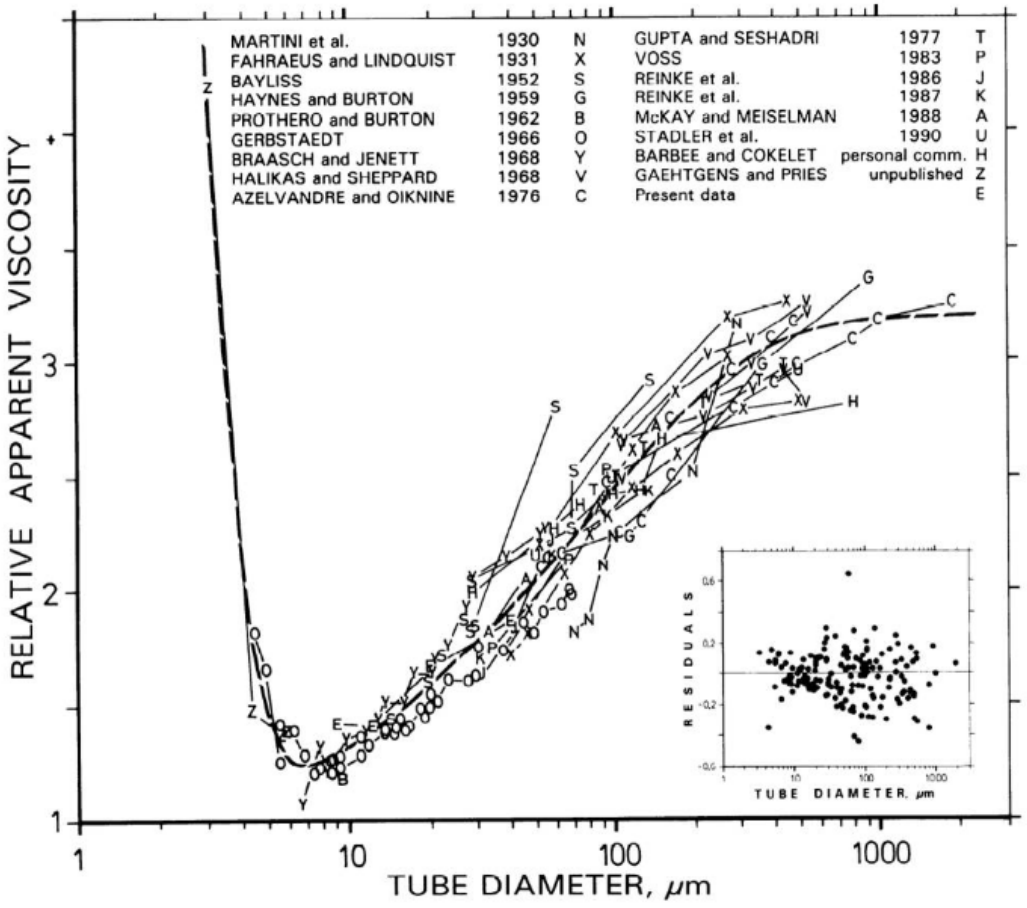

Figure 1.10: Fåhræus-Lindqvist effect : Change in relative apparent viscosity of a 45 % Ht RBCs solution circulating depending on the diameter of the tube. Reprinted from Pries, Neuhaus, and Gaehtgens [36]

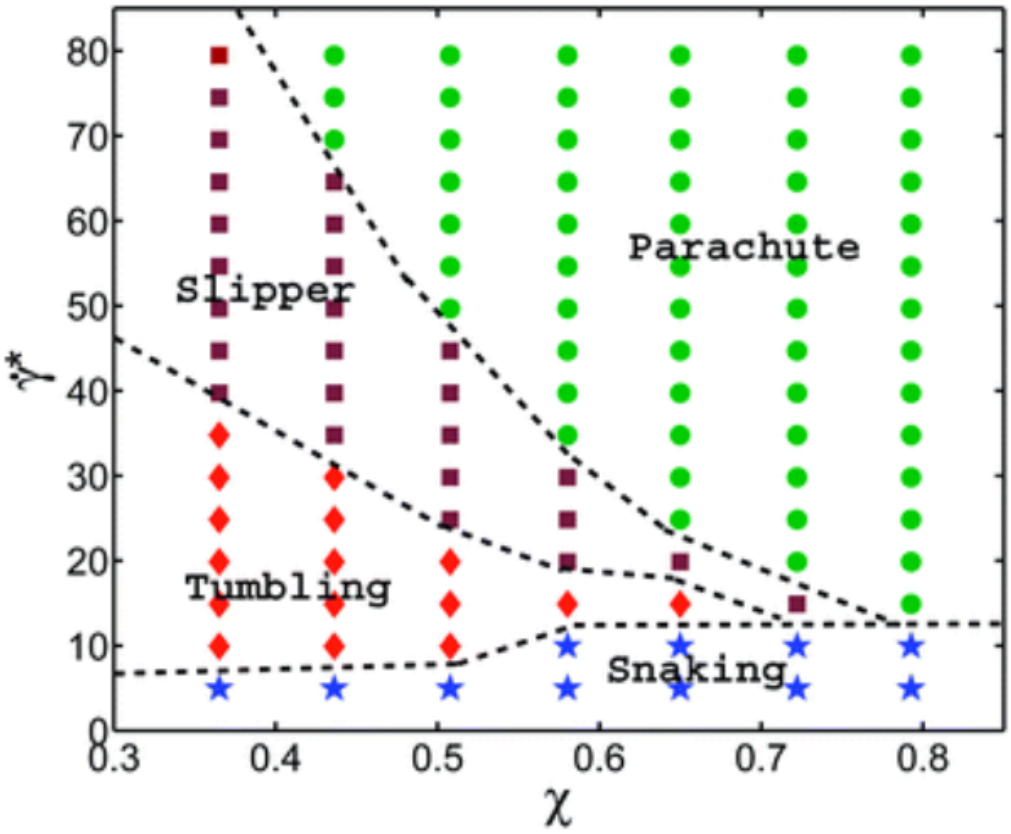

Figure 1.11: Phase diagram of RBC dynamics states for a 3D simulation of flow in a cylindrical channel depending on the flow strength characterized by the shear rate $\dot{\gamma}^*$ and the confinement χ. The symbols depict performed simulations, with the RBC states: parachute (green circles), slipper (brown squares), tumbling (red diamonds) and snaking (blue stars) discocytes. The phase-boundary lines are guides the eye. Reprinted from Fedosov, Peltomäki, and Gompper [37].

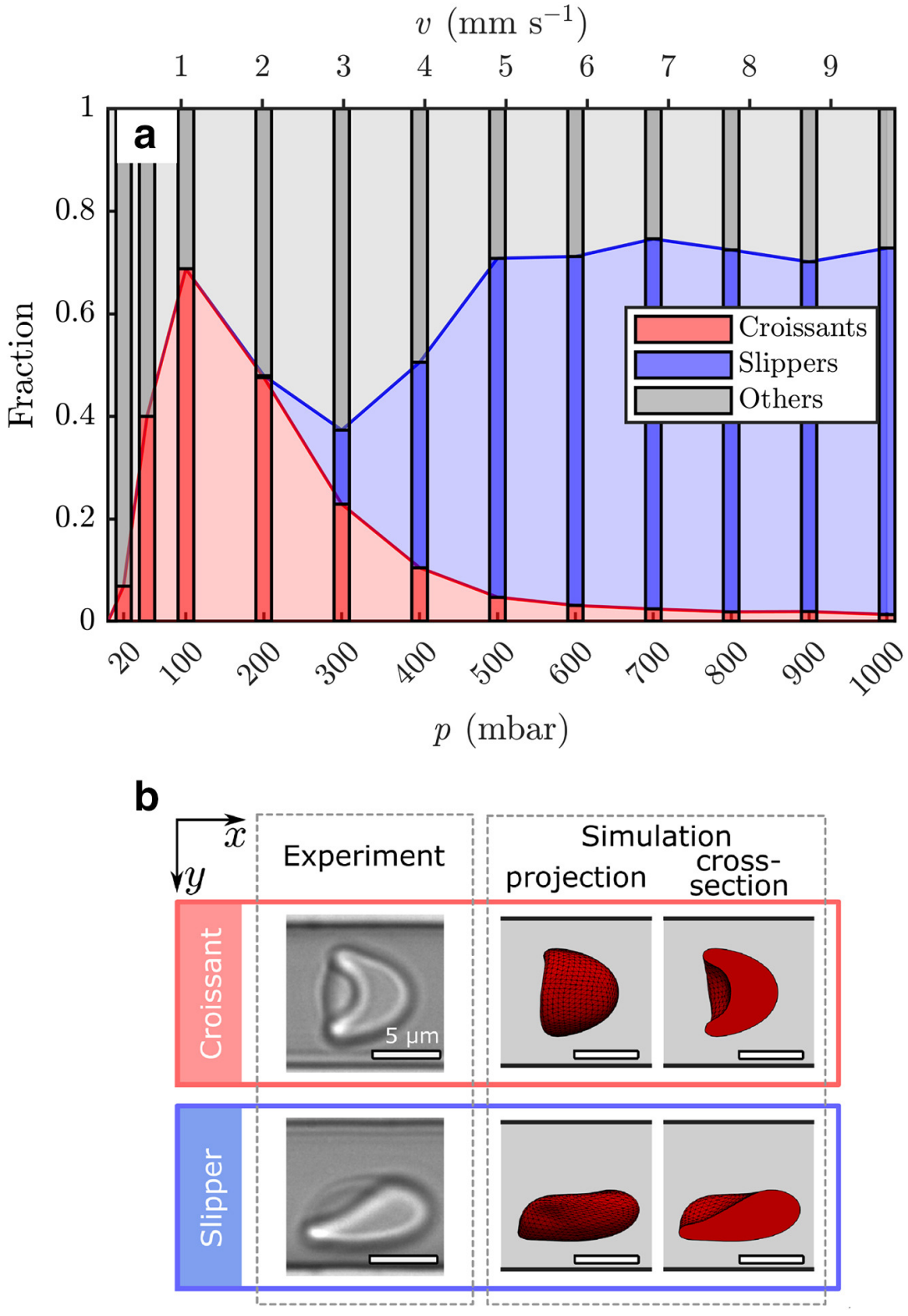

Figure 1.12: Influence of velocity or pressure on RBC shape in flow in rectangular 10×8 µm microfluidic channels. (a) Fraction of RBC shapes as a function of the applied pressure drop (bottom axis) and the mean cell velocity (top axis). (b) Representative examples of a croissant (top) and a slipper (bottom) for experiments with p = 100 mb and p = 600 mb, corresponding to cell velocities of $v \approx 1$ mm.s^{-1} and $v \approx 5.8$ mm.s^{-1}, respectively. The simulation snapshots are obtained at similar velocities. The flow is in x direction, and the scale bars represent a length of 5 µm. Reprinted from Recktenwald, Graessel, Maurer, *et al.* [38].

of the channel is a rectangle instead of a disk or a square, the parachutes are flattened and look more like croissants. They are dominant at 1-2 mm/s. The shape of the RBCs will obviously depend on their flexibility. Yet the density of RBCs increases when they age, and their deformability decreases with density [40]. They have a lifespan of approximately 120 days, until they eventually are not deformable enough to squeeze in the blood capillaries and are eliminated by the macrophages in the spleen and liver.

Chapter 2

Distribution of aggregated red blood cells at a microbifurcation

2.1 Introduction

2.1.1 Motivation

Considering the size of a blood capillary and the characteristics of the flow, microcirculation is assumed to follow a laminar regime. In the *in vitro* experiment we designed, the width of the channel is $w = 23$ µm and the carrier phase is water so we consider the density $\rho = 1000\, kg \cdot m^{-3}$ and the viscosity $\mu = 0.001\, kg \cdot m^{-1} \cdot s^{-1}$. The maximum studied velocity is $u = 25\, mm \cdot s^{-1}$. Thus the maximum Reynolds number will be $Re = \rho.u.w/\mu = 0.575 < 1$.

When a suspension of particles flows through a bifurcation in a microfluidic flow as is the case in blood microcirculation, the two outlet branches are not symmetric in the general case, whether for geometrical reasons (angle and width of the channels) or because the flow rates are different due to different pressures or flow resistances.

If the particles are small compared to the channel diameter and are homogeneously distributed in the inlet branch, they can be considered as flow tracers that simply follow fluid streamlines and the distribution of particles in the outlet branches simply follows the distribution of flow rates. Therefore, in this limit case, the particle concentration remains homogeneous after the bifurcation as would a dye concentration. This is generally the case in large blood arteries or veins where the hematocrit is close to the systemic hematocrit everywhere.

On the contrary, it is known, especially in blood flows, that in the case of non-symmetrical bifurcations, the hematocrit (volume fraction in red blood cells) can be different in the two outlet branches. This was first revealed by the pioneering work of Poiseuille [5] who showed that the red blood cell distribution is very heterogeneous in the capillaries and that there is a depletion layer with no red blood cells in the vicinity of the walls, usually called the Cell-Free Layer (CFL) or Cell-Deplated Layer (CDL). The heterogeneity of this distribution is a consequence of an asymmetric separation of red blood cells at

bifurcations. Model experiments in microfluidics have shown that in general, for perfectly symmetrical bifurcations where the two outlet branches are locally geometrically identical but flow rates are different in these two branches (for example because the outlet pressures or branch lengths are different), the hematocrit is higher in the branch of higher flow rate, a phenomenon called Zweifach-Fung effect [41][42]. If the asymmetry of the bifurcation outlet flow rates is such that one branch receives only a quarter of the inlet flow rate, the hematocrit in that branch may fall to zero, i.e. only plasma from the CFL of the inlet branch goes to the low flow-rate outlet branch. A number of in-vivo studies [43], as well as studies on model systems [44] or numerical simulations [45] have been devoted to this phenomenon. It is strongly influenced by the configuration of the particles or blood cells that arrive at the bifurcation [46], which may even lead in some situations to inversion of the partition [47]. These phenomena are crucial for the distribution of red blood cells at the scale of a capillary network [48].

Several experimental and numerical studies have shown that RBC aggregation has an influence on the structure of blood flow in small channels in ranges of fibrinogen (or Dextran) plasma concentrations that cover physiological ranges in healthy or pathological situations. For instance, aggregation tends to stabilize red blood cell clusters in capillaries [13] and leads to an increase of the CFL thickness in channel flow. This effect result in a lower effective viscosity of the blood, as the CFL acts like a lubrication layer [49][50]. The combination of these structural and rheological changes, as well as the cohesion between flowing cells, is therefore expected to influence the behavior of RBCs at a bifurcation and the distribution of the hematocrit in capillary networks. Previous experiments have shown that the breakup or survival of RBC aggregates flowing through a bifurcation is governed by a subtle balance between hydrodynamic forces and aggregation forces with consequences on the way RBCs are split between the outlet branches [51][52]. A suggested generic feature seems to be that when hydrodynamic forces are not sufficient to break aggregates, the Zweifach-Fung effect is enhanced. In addition, the reduction of the CFL thickness observed associated to aggregation [49] should also enhance this hematocrit partitioning effect. A few recent studies have focused on the influence of aggregation on the distribution of RBCs in bifurcations made of relatively large channels compared to the RBC size (100 µm or more) [53][54][55].

Sherwood, Kaliviotis, Dusting, *et al.* [55] have studied the T-bifurcation of a large and flat channel with a cross-section of 100×40 µm. Their work has shown that a concentration of 5 g/L of Dextran 2000 kDa affects the distribution of hematocrit in the daughter branches. The aggregation induced by Dextran amplifies slightly the heterogeneity of the distribution and reduces the number of RBCs flowing through the lower velocity branch, which results in a maximal variation of 2 % (Figure 2.1). A direct comparison of their results with other studies is problematic because there is no study on the aggregating force depending on the concentration of Dextran 2000 kDa. Additionally, the size and flat shape of the channel do not align with the physiological range

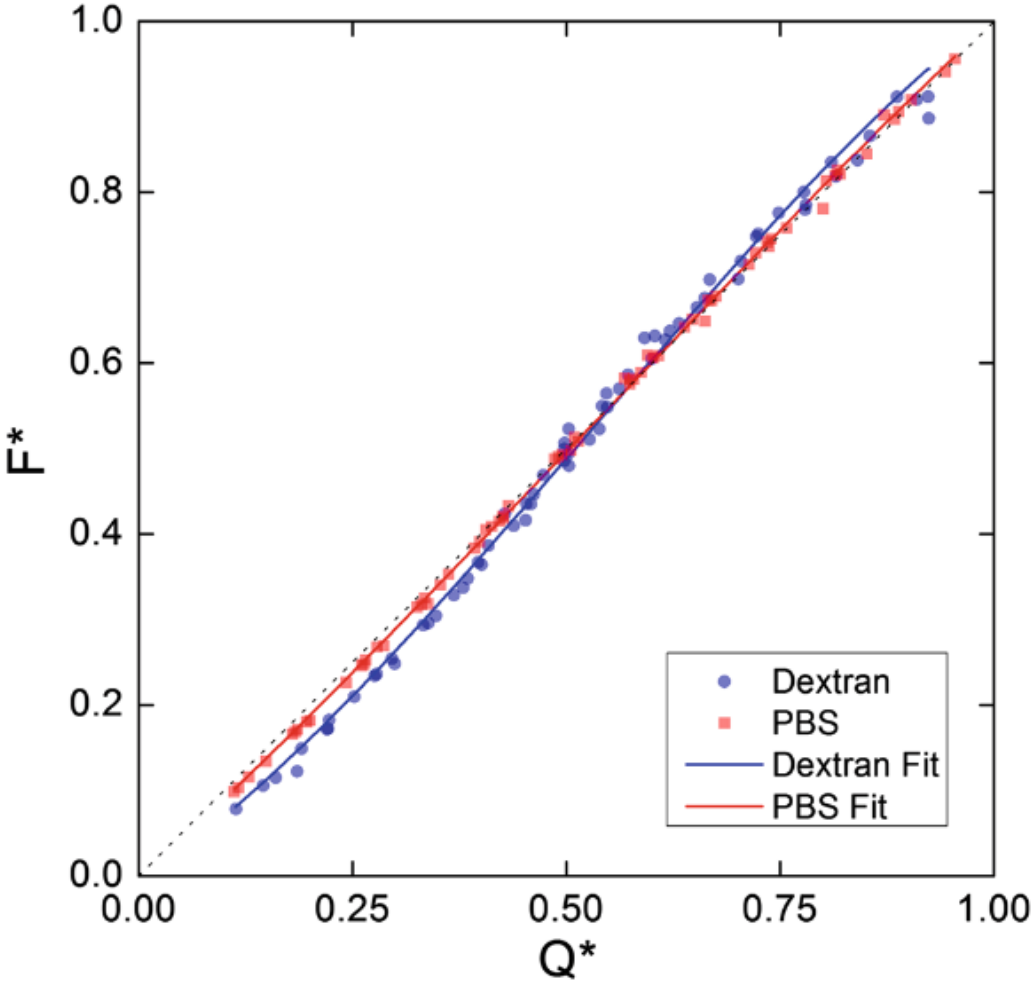

Figure 2.1: Measures of the flux of RBCs in one daughter branch normalized by the total flux of RBCs in both daughter branches as a function of the flow rate of blood in the same branch normalized by the total flow rate of blood in both daughter branches in a T-bifurcation with a cross-section of 100×40 µm, in PBS without aggregation (red) and with Dextran-induced aggregation (blue). The lines are sigmoid fits. Reprinted from Sherwood, Kaliviotis, Dusting, *et al.* [55].

for microcirculation. Although an higher effect of the CFL is to be expected in smaller channels, there has been no systematic study of this phenomenon in channel networks that are relevant to the microcirculation (channel diameter lower than 20-30 µm), despite its likely strong influence on blood perfusion in microcirculatory networks, oxygen delivery and the possible consequences of hyper-aggregability in pathological cases.

In this chapter, we present a study on the distribution of RBC suspensions at a model microfluidic bifurcation and provide results on the influence of the interaction energy, hematocrit and flow rate distribution on the asymmetry of RBC distribution in the outlet branches.

2.1.2 Problem statement and background

We chose to focus on a microfluidic bifurcation with a fixed, symmetric geometry (one inlet branch with a roughly square cross-section and two identical, symmetric outlet branches with the same cross-section), fed by a RBC suspension with controlled aggregation strength while the flow rates in the different branches are controlled through imposed pressure boundary conditions. The main objective is to characterize the Zweifach-Fung effect (phase separation at the bifurcation) as a function of the imposed flow rate difference in the outlet branches, aggregation strength and inlet hematocrit in order to quantify the influence of aggregation on the hematocrit distribution at the outlets.

Empirically, for suspensions of RBCs or other particles with no aggregation, it has been shown that the relationship between FQ_e the ratio of particle fluxes in the two outlet branches and FQ_b the ratio of global suspension flow rates in these outlets follows an approximately sigmoid $FQ_e = S(FQ_b)$ behavior [34][46]:

$$FQ_e = \frac{1}{1 + e^{-FQ_b}} \tag{2.1}$$

Note that without phase separation, these two ratios would simply be equal, translating the fact that particles behave as passive tracers. Pries, Secomb, Gaehtgens, *et al.* [34] proposed the following improved relation between FQ_e the ratio of the flux of RBCs in each daughter branch and FQ_b the ratio of the flow of blood in each daughter branch :

$$FQ_e = \begin{cases} 0 & \text{if } FQ_b \in [0, X_0] \\ f(FQ_b) = \dfrac{1}{1+e^{-\left[A+B\times logit\left(\frac{FQ_b - X_0}{1-2X_0}\right)\right]}} & \text{if } FQ_b \in]X_0, 1-X_0[\\ 1 & \text{if } FQ_b \in [1-X_0, 1] \end{cases} \tag{2.2}$$

where :

$$logit(x) = ln\left(\frac{x}{1-x}\right) \tag{2.3}$$

and A, B and X_0 are parameters that depend *a priori* on the geometry of the bifurcation, inlet hematocrit and flow rate. A reflects the possible asymmetry of the curve due to geometric differences between the outlet channels (different angles or hydraulic diameters), and should be close to 0 in our case. X_0 defines the range of flow rate ratios $]X_0, 1 - X_0[$ for which RBCs flow through both daughter branches. In other words, outside this range, all RBCs go through the same daughter branch. Thus X_0 is connected to the existence of a cell-free layer in the inlet branch and is an increasing function of the CFL width. B represents the sigmoid-like curvature of the relation and the sharpness of the transition and indicates the intensity of the phase separation phenomenon : $B = 1$ means a linear relation (no phase separation), $B > 1$ means phase separation takes place, and when $B \to +\infty$ the relation is a step function (all cells go to the same outlet branch).

In one of their papers, Pries, Secomb, Gaehtgens, *et al.* [34] establish general expressions for parameters A, B and X_0 as a function of the diameters (µm) of the daughter branches, D_α and D_β, of the mother branch, D_f, and of the hematocrit in the mother branch, Ht. Empirically, it establishes :

$$A = \frac{-6.96}{D_f} \times \ln\left(\frac{D_\alpha}{D_\beta}\right) \tag{2.4}$$

$$B = 1 + 6.98\frac{1 - Ht}{D_f} \tag{2.5}$$

$$X_0 = \frac{0.4}{D_f} \tag{2.6}$$

These relations were established from a statistical study of *in vivo* observations on bifurcations in rat's mesentery [34] without independent control of the various parameters (inlet hematocrit, geometry of the bifurcation, flow rate distribution). Furthermore, the RBC aggregation level was not imposed or controlled. Therefore the expressions they obtained (Equations 2.4–2.6) only represent an average behaviour over a large variety of situations. Ideally, the specific influence of different parameters should be reflected by different expressions for A, B, X_0. In the following, and to highlight the influence of RBC aggregation on hematocrit separation at bifurcations, we will assume that the general form of the separation law (Equation 2.2) still holds, while determining sets of paramters (A, B, X_0) from specific experiments.

In the following, we first present the experimental setup, methods and protocols used in this *in vitro* experiment to control the flow, sample properties and make local hematocrit and velocity measurements. We then follow by presenting results in which we studied the distribution of the hematocrit at the bifurcation by varying the ratio of outlet flow rates, for different levels of RBC aggregation and hematocrit. We then provide conclusions on this work, their implications on blood microcirculation and suggestions for further studies.

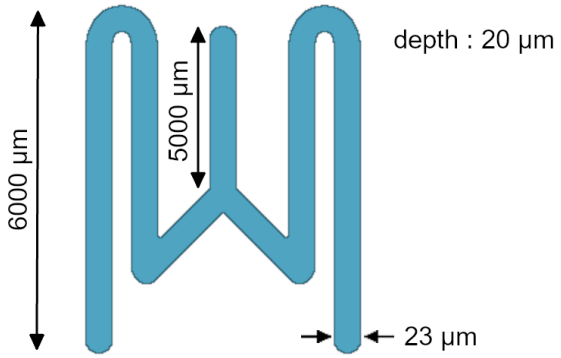

Figure 2.2: Microfluidic channel design, not to scale. The width of the channels is 23 µm, the distance between the inlet (top) and the bifurcation is approximately 5 mm and the distance between the bifurcation and the outlets (bottom) is approximately 12 mm.

2.2 Experimental setup and sample preparation

2.2.1 Microfluidic chip

The utilization of microfluidics allows for the manipulation of fluid in channels with dimensions on the micrometer scale. Soft lithography techniques, allowing Polydimethylsiloxane (PDMS, a silicone elastomer) based microfabrication, are commonly employed in the construction of microfluidic chips due to their cost-effectiveness, ease of replication, and versatility in design. This technique is typically utilized in the creation of two-dimensional (2D) channel configurations, but the potential for three-dimensional (3D) structures also exists through the use of multi-layered PDMS superimposition or modulation of light exposure during the fabrication process. Additionally, PDMS is an ideal material for microfluidic chip fabrication due to its biocompatibility, transparency, and gas permeability.

A microfluidic channel design, as depicted in Figure 2.2, was employed in our experiments. The chip features a symmetrical Y-junction bifurcation, in which all branches possess a width of 23 µm and a constant depth of 20 µm. The angle between both outlet branches is 90 °. The large disks correspond to the inlet and outlets connections of the chip. To improve stability and facilitate precise control of flow rate ratios through pressure regulation, serpentine structures were incorporated to increase the length and hydraulic resistance of the outlet branches.

Microfabrication of the mold

The fabrication process of a microfluidic chip follows the steps of the classic soft-lithography technique described in Figure 2.3. The pattern of the channels is first created utilizing a computer-aided design software, able to produce vectorial drawings, such as AutoCAD, or through the use of Dilasesoft

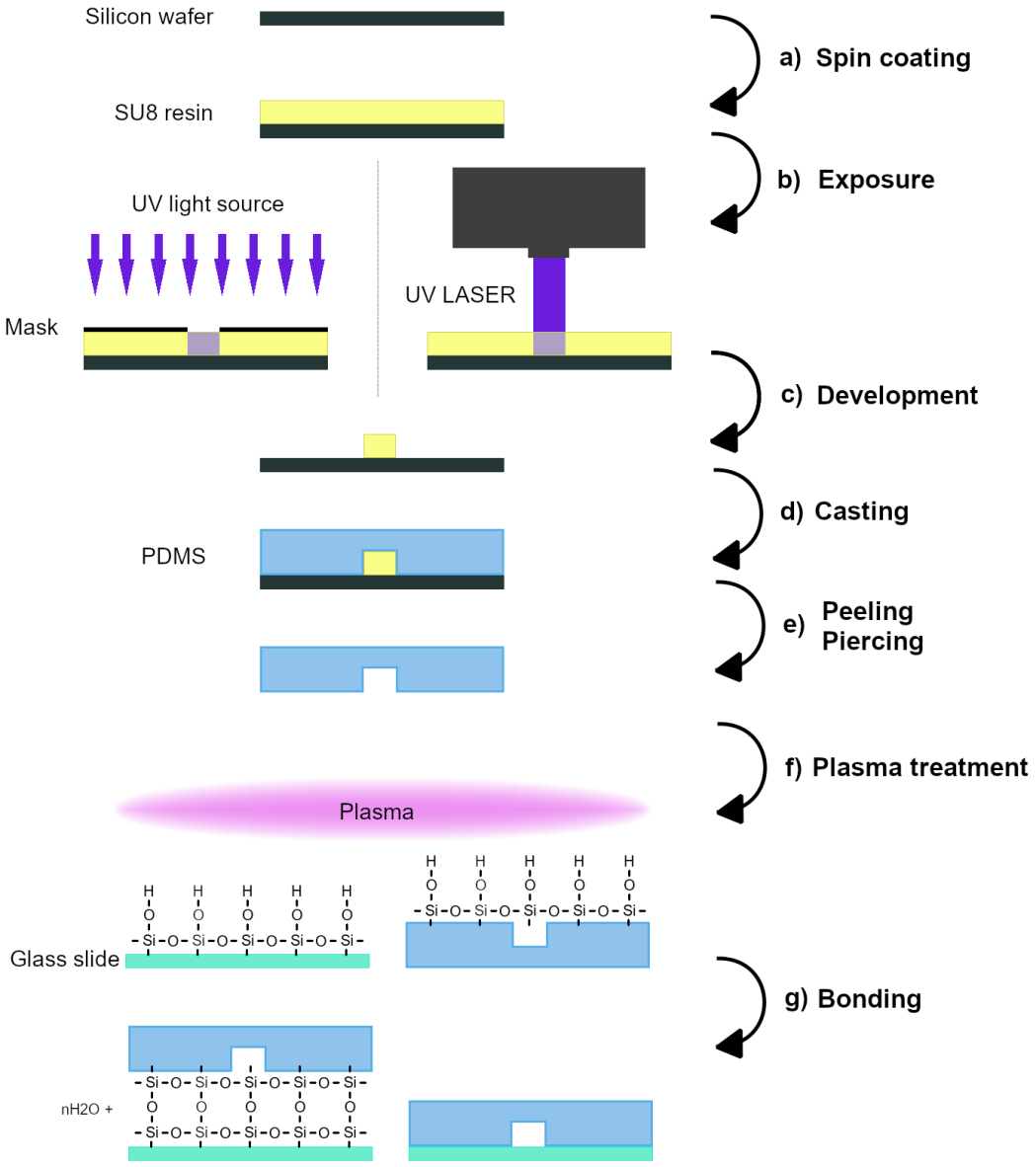

Figure 2.3: Steps of the microfabrication process by photolithography. (a) A layer of 20 µm of photosensitive resist SU8 is spread by spin-coating on a silicon wafer. (b) The chosen parts of the resist are exposed to UV to polymerize, either using a photomask with the design of the channels, or by directly inscribing the channels with a LASER beam. (c) The parts of the resist not exposed to UV are dissolved. The result is the mold. (d) A 1:10 mixture of curing agent and PDMS is poured on the mold and reticulates at 70 °C. (e) Once hardened, the PDMS is removed from the wafer and pierced at the inlets and outlets of the channels. (f) The oxidation of the surfaces using a plasma (from air or from oxygen) enables the chip sealing by (g) bonding the PDMS to a glass slide. The mold can be used multiple times to make more PDMS chips by doing again steps (d)-(g).

integrated into the LASER direct photolithography system described below. A photolithography method, a widely used and well documented technique in the microfluidics field for its high precision at the microscopic scale [56], is then employed to fabricate a mold of the pattern. Here, we recall the main steps. The process begins with the spin-coating of a negative photosensitive resist, SU8 (SU8-2025, Microchem), on a silicon wafer to create a homogenous layer of a controlled thickness (here 20 µm). The pattern is then inscribed into the resist through the use of a UV LASER beam (wavelength 405 nm, diameter 1 µm) of the direct LASER photo-lithography equipment (KLOE Dilase 250). The exposed regions of the resist undergo polymerization, while the unexposed regions are dissolved during development. The resulting mold can then be utilized multiple times for single-use PDMS microfluidic chip productions.

Fabrication of the PDMS device

To produce the PDMS microfluidic chip, a mixture of a curing agent (cross-linker) and PDMS (Sylgard 184 from DOW-Corning) is poured onto the mold with a volume ratio of 1:10. To remove air bubbles and thus ensure proper channel formation and mixture homogeneity, the filled mold is placed in a vacuum chamber prior to being cured in an oven at 70 °C where the PDMS cross-links and hardens overnight. The PDMS slab is then cut and peeled off the mold and punched at the inlets and outlets of the chip. To seal the chip, the PDMS slab is bonded to a glass slide through plasma treatment, removing hydrocarbon groups from both the PDMS and glass surfaces to create a Si-O-Si covalent bond. The chip is subsequently heated at 70 °C for 15 min to enhance the bond strength.

2.2.2 Blood sample preparation

Stock solutions

All solutions used in experiments are based on Phosphate-Buffered Saline (PBS), an isotonic (i.e. which has the same osmotic pressure as the internal medium of the cells, see Figure 2.4), water-based buffer solution with a pH equal to 7.4. The buffer solution is prepared from powder tablets (Sigma-Aldrich, REF P4417) dissolved into 200 mL of purified and deionized water.

Bovine Serum Albumin (BSA) is a protein extracted from cow's blood and used here to prevent the adhesion of the RBCs on the different surfaces of the tubes, tubing and microchip. The solution is made by dissolving 100 mg of BSA crystals (Sigma-Aldrich, REF A7906) into 10 mL of PBS, thus obtaining a 1 % mass-volume ratio.

The aggregating agent used to tune the aggregation force in our experiments is Dextran 70 kDa (Dex70) as in previous studies [13][57]. To make a 60 mg/mL solution, 600 mg of Dex70 powder, produced by Leuconostoc mesenteroides, (Sigma-Aldrich, REF D8821) are dissolved into 10 mL of PBS. This Dextran

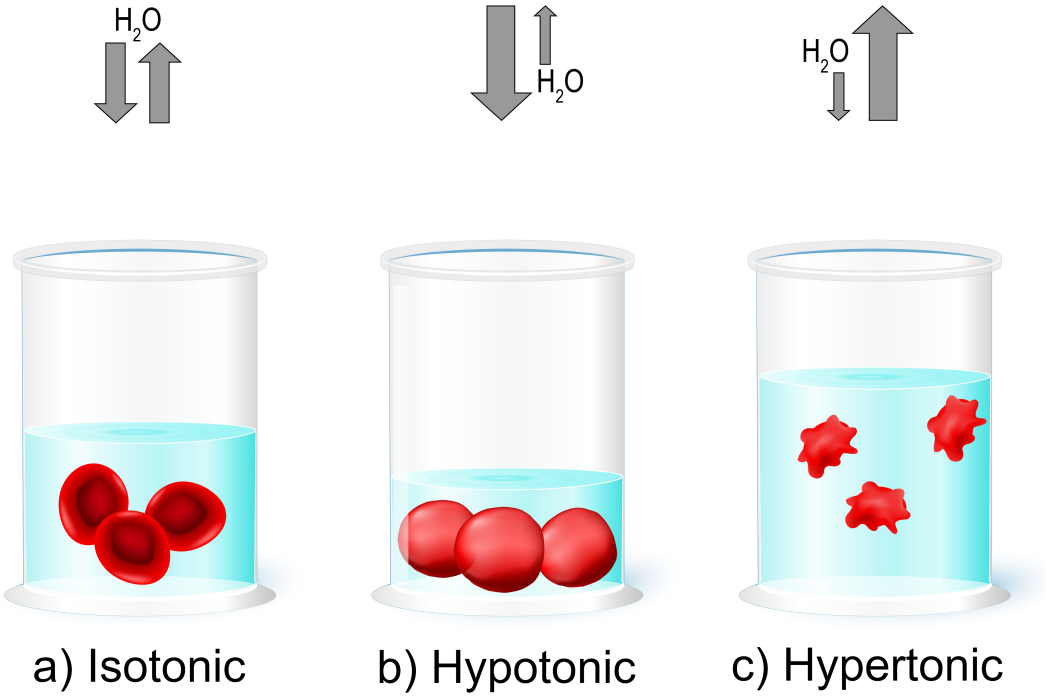

Figure 2.4: Illustration of the effect of tonicity on RBCs. (a) In an isotonic medium, the RBCs take their usual discocyte shape at rest. (b) In a hypotonic medium, the osmotic flow goes toward the cytosol. The RBCs take the shape of spherocytes or stomatocytes. (c) In a hypertonic medium, the osmotic flow goes toward the external medium. The RBCs shrink and take the shape of echinocytes.

stock solution is then used to make more dilute Dextran solutions when preparing the final samples.

All stock solutions are kept at 4 °C in accordance with the supplier recommendations.

Blood

The blood is supplied by the French blood establishment (Etablissement Français du Sang, EFS). For each order, 2.7 mL of blood are taken from an anonymous donor in a citrated (citrate acts as an anticoagulant) tube 3 to 4 days before the delivery. After the withdrawal, the blood sample is tested for several pathologies : HIV, HTLV I-II, Hepatitis B, Hepatitis C and syphilis. Once received, the sample is kept at 4 °C, for one day most of the time and up to two days, in order to avoid an excessive evolution of RBCs properties [58].

After several trials and adjustments, the following protocol was established to prepare 4 mL of diluted RBCs at different concentrations. To extract only washed RBCs from the sample, 1.5 mL of full blood is centrifuged at 500 rcf in an Eppendorf tube, for 3 to 5 min, to separate cells from plasma (Figure 1.1). The supernatant (yellowish plasma) and the buffy coat, composed of white blood cells and platelets, are then removed and replaced by PBS. The solution is mixed by gently inverting the tube several times. Then the centrifugation step and the replacement of the supernatant with fresh PBS are repeated two more times. After the last centrifugation, a certain volume of packed RBCs is taken from the bottom of the tube, depending on the desired hematocrit (Ht) in the final sample (between 0.5 % and 7 %), and suspended in a solution containing PBS and the aggregating agent Dex70 at different concentrations (final concentration between 20 mg/mL and 50 mg/mL) from a 60 mg/mL stock solution, depending on the desired aggregation force. The experiments without aggregation refer to 0 mg/mL of Dex70. To prevent the adhesion of the RBCs to channel walls, BSA is added from a 1 % (1 g/100 mL) stock solution for a final concentration of 0.1 %. Thus, for instance, for a sample with 2.5 % Ht and 30 mg/mL of Dex70, 100 µ L of packed RBCs are suspended in a solution containing 400 µ L of 1 % BSA, 2 mL of 60 mg/mL Dex70 and 1500 µ L of PBS.

2.2.3 Experimental set-up

The experiments are conducted by passing the red blood cell sample through a microfluidic bifurcation depicted above (Figure 2.2). The sample is pumped from a 15 mL tube (Falcon, REF : 352097) using an air pressure controller (Elveflow, REF : OB1), with pressures around 100 mb. PTFE tubing (adtech, REF : BIOBLOCK/14) with an internal diameter of 0.8 mm is used to connect the sample tank to the inlet of the microfluidic chip and to connect each outlet to its waste tank (Figure 2.5). In the experiment, we independently control the pressure in the three inlet and outlet tanks. Creating a pressure drop by keeping the pressure in the waste tanks lower than the one in the sample tank

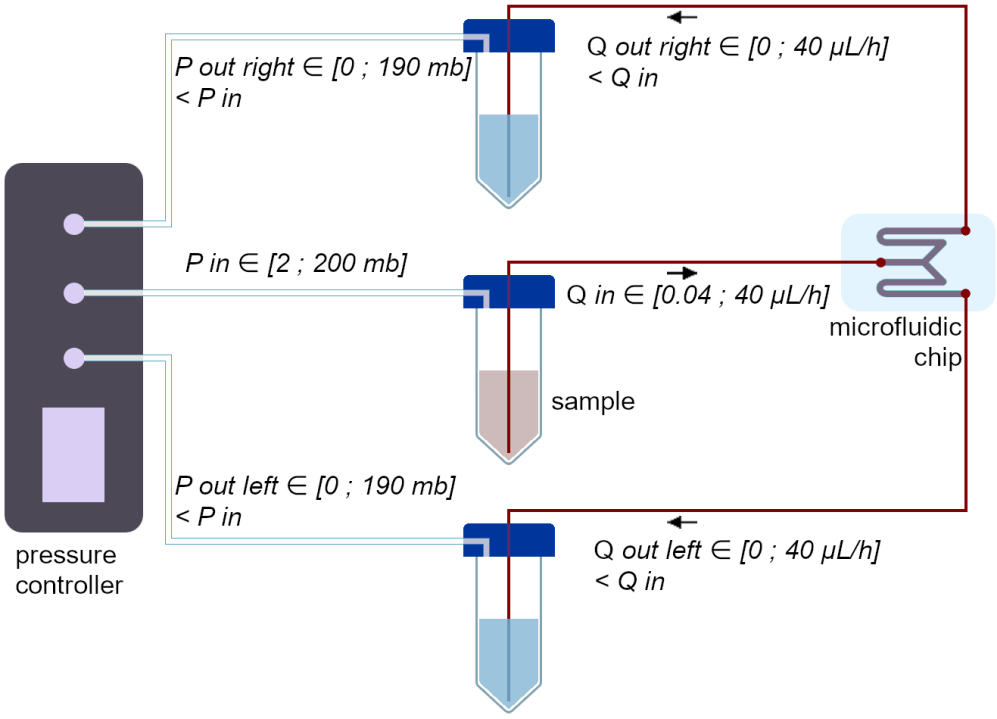

Figure 2.5: Connection diagram of the experimental set-up. The pressure controller is connected to the sample and waste tanks via soft tubing and using adaptor caps. The pressure is applied inside the tanks. From the sample tank, the RBCs is pushed by the air pressure through PTFE tubing towards the inlet of the microfluidic chip. The sample is observed under microscope while flowing through the chip. The outlets of the chip are connected to the waste tanks, half-filled with distilled water beforehand, to collect the used sample. The pressure in the tanks are controlled as previously to ensure the pressure drop between the inlet and the outlets.

generates a flow. The flow-rate ratio between the daughter branches is tuned by modifying the pressures at the outlets while modifying the pressure at the inlet will change the total flow-rate in the chip. In order to better control the pressures at work, the PTFE tubings are filled with 1 % BSA beforehand, and the waste tubes are half-filled with the same volume of distilled water.

The observation is made with an inverted microscope (Olympus IX71) working in bright field mode with a white light source (halogen lamp), using a 4-fold objective (Olympus Plan N, Numerical Aperture : 0.10, Objective Field Number : 22) and a camera (ImagingSource, DFK 23UM021, sensor CMOS, pixel size = 3.75×3.75 µm) recording at 117.65 fps.

2.3 Flux metrology

The data analysis consists in determining the flux of RBCs going in each daughter branch as a function of the distribution of the total flow imposed by the pressure control. We define the flux of RBCs with the following relation :

$$F = Q.\overline{Ht} \tag{2.7}$$

where Q is the flow rate in the branch and $\overline{Ht}$ is the spatial mean hematocrit (volume ratio of RBC) in the branch.

Both Q and $\overline{Ht}$ have to be determined by image processing from the recordings. The processing has been semi-automatized using Python and the techniques used to derive the hematocrit and flow rates are described in the following.

2.3.1 Segmentation

When the concentration of RBCs is low enough, with all the cells distinguishable, which occurs around a hematocrit of 2 %, the most accurate way to measure the concentration is to count them. First, a convolution filter is applied to the video, using the $filter2D$ function from the $OpenCV$ python library, to remove the pattern due to the camera sensor (Figure 2.6). The pixels on the camera are grouped four by four, thus the kernel for the filtering has the same size :

$$\left\{ \begin{array}{cc} 1 & 1 \\ 1 & 1 \end{array} \right\} * \frac{1}{4}$$

Then, the background picture is determined by keeping the maximum light value that each pixel takes during the recording. Indeed, the background is composed of the walls of the channels, the specks of dust and the defects which are all fixed items. The cells, however, shall not affect the background. As they absorb light, when a cell passes, the light intensity is lower at this position. Keeping the maximum light value ensures measuring it from a frame without a cell at this position. The background is then subtracted from all the frames.

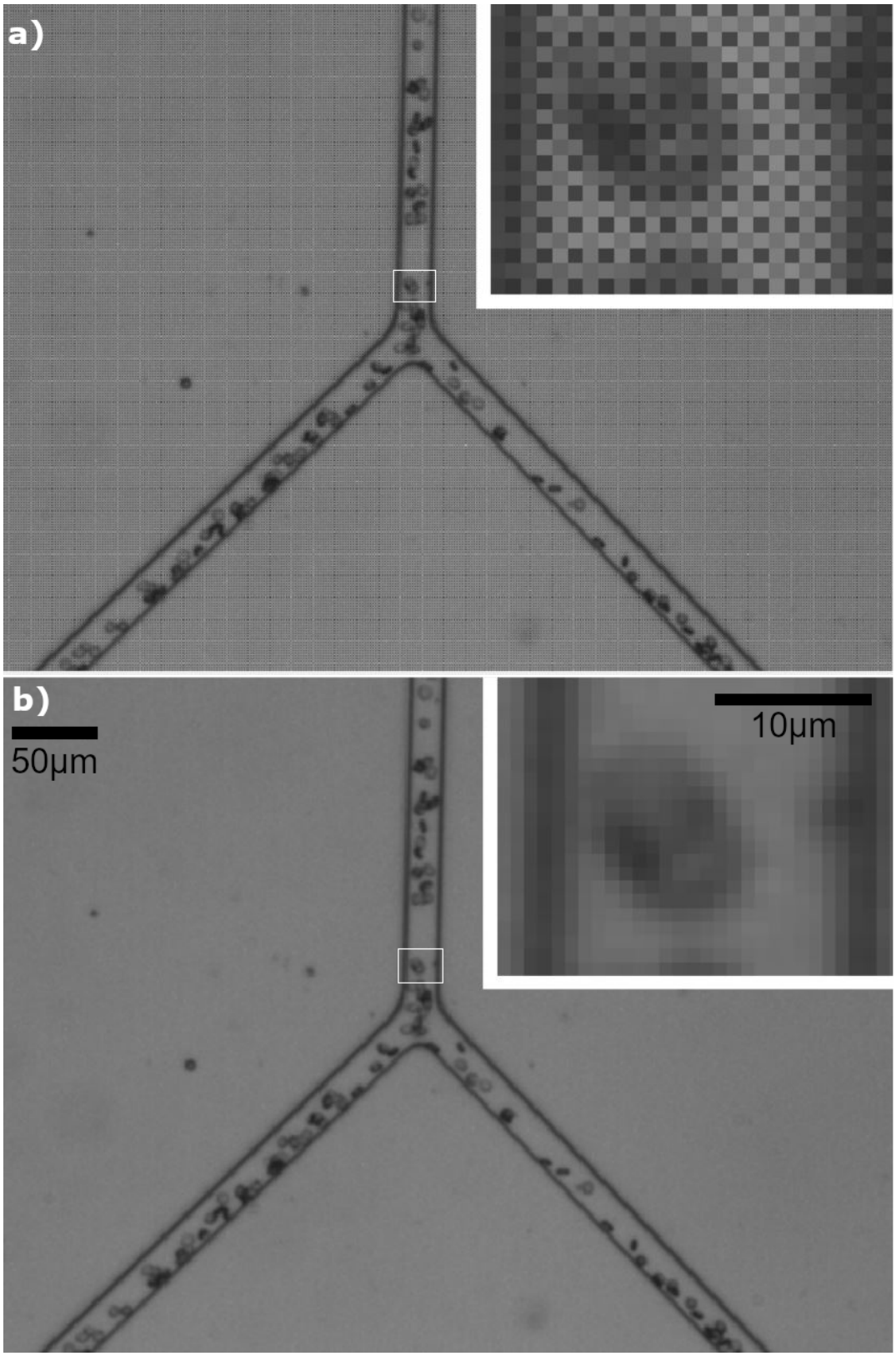

Figure 2.6: Frame extracted from a recording of RBCs going through the bifurcation. a) Raw picture from the camera and magnification inset of the inlet channel. b) Same picture after convolution filtering.

Next, the frames are binarized by threshold and segmented using the function *morphology* from the image processing library *skimage*. The number of cells of each cluster in the branches is deduced using a histogram in such a way that intervals of area are defined for a single cell ($[C1_{min}, C1_{max}]$), a cluster with two cells ($[C2_{min}, C2_{max}]$) and a cluster with three cells ($[C3_{min}, C3_{max}]$). Above $C3_{max}$, an approximate number is assessed using the following linear relation :

$$N_{RBC} = \left\lfloor 3\frac{A - C1_{min}}{C3_{max} - C1_{min}} \right\rfloor \tag{2.8}$$

where N_{RBC} is the number of RBCs in the cluster and A is the area in pixels of the cluster. Thus, when $A = C1_{min}$, $N_{RBC} = 0$ and when $A = C3_{max}$, $N_{RBC} = 3$.

Then, the mean hematocrit $\overline{Ht}$ in each branch follows the relation :

$$\overline{Ht} = \frac{V_{RBC}}{V_b.N_f} \sum_{i=1}^{N_f} N_{RBC_i} \tag{2.9}$$

where $V_{RBC} = 90$ µm^3 is the mean volume of a RBC, V_b is the volume of the branch, N_f is the number of frames in the studied recording and N_{RBC_i} is the number of RBCs in the branch on the i^{th} frame.

2.3.2 Hematocrit measurements

When the hematocrit of RBCs is higher than 2 %, the counting method becomes irrelevant as the probability of overlap of RBCs increases, leading to a significant error. Thus we chose to employ a method based on the transmission of light intensity by the RBCs. There are several phenomenons acting when light goes through a RBCs mixture. First, the hemoglobin present in the RBCs absorbs the light according to a Beer-Lambert law [59], especially at wavelengths around blue and green [60]. Second, the RBCs, as a micrometer-sized particles suspension with a refractive index that is higher than the suspending medium, disperse and diffract the light. However it has been empirically established [61][62] that, despite this complex combination of absorption and dispersion, the transmitted part of the light going through a blood sample follows a Beer-Lambert like relation, for hematocrit up to 20 %, *i.e.* it behaves as a purely absorbing medium although the effective absorptivity cannot be simply related to the absorptivity of hemoglobin: :

$$I_t = I_0.\exp\left(-\epsilon.l.Ht\right) \tag{2.10}$$

where I_0 is the incident light intensity, I_t the transmitted light intensity, ϵ the effective absorptivity of the RBC, $l = 20$ µm the thickness of the sample and Ht the concentration of RBCs.

We can then rewrite equation 2.10 as follows :

$$\frac{Ht}{Ht_0} = -ln\left(\frac{I_t}{I_0}\right) \tag{2.11}$$

with $Ht_0 = \frac{1}{\epsilon.l}$.

Ht_0 can be determined by using reference pictures at low concentrations when both the light intensity and the hematocrit are known. The values at higher hematocrit can thus be extrapolated.

In practice, the same convolution filter as for lower hematocrits is applied to the recording. Nonetheless, the concentration of RBCs is too high to compute the background picture the same way than previously, as the channels are always filled with cells. Therefore we chose to record a short video (100 frames) when the chip is only filled with a BSA and Dex70 solution at the same concentrations than the sample. To minimize the white noise, the background picture is made by taking the temporal median value of the video for each pixel. As there is often a slight movement of the chip under the microscope during the experiment, between two recordings, we re-aligned the background picture with the video. For that, we use the *OpenCV* library. First we binarize both the background picture and the first frame of the video runing the *adaptiveThreshold* function, then we clean them using *remove_small_holes* from the *skimage.morphology* library. Finally, we find the translation and rotation between them using the *findTransformECC* function and we run the *warpAffine* function to re-align them.

We then apply the relation 2.11 on each pixel :

$$\frac{Ht}{Ht_0} = -ln\left(\frac{I_{sample}}{I_{ref}}.\frac{I_{ref_0}}{I_0}\right) \tag{2.12}$$

where I_{sample} is the pixel value on the frame of the recording, I_0 the pixel value on the background, I_{ref_0} the reference intensity on the background and I_{ref} the reference intensity on the frame. The reference intensities are used to suppress the intensity temporal variability due to the camera and the experimental set-up, and are determined by taking the spatial mean intensity of an empty reference zone, in a corner of the region of interest, on the background and the frame respectively.

We obtain a map of $\frac{Ht}{Ht_0}$ such as in Figure 2.7. The final measured values are the spatial and temporal mean of $\frac{Ht}{Ht_0}$ in the mother branch and in both daughter branches of the bifurcation. Ht_0 can be determined for each set of experiment by performing a low hematocrit recording. The actual Ht is computed using the segmentation process, then $\frac{Ht}{Ht_0}$ is computed with the process described just above, leading to know Ht_0 by a simple cross product. This value can then be used to extrapolate the hematocrit for higher cell concentrations.

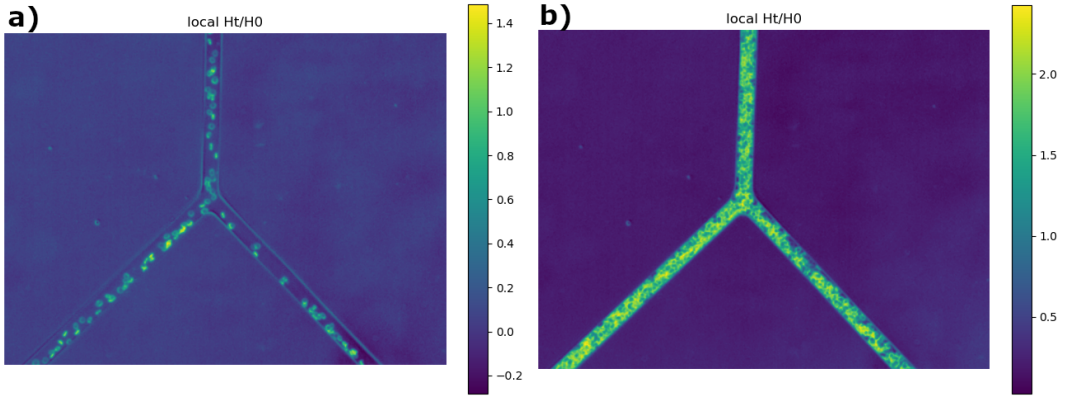

Figure 2.7: Map of the computed Ht/H0 on a bifurcation for a) a previously determined inlet hematocrit of 2 % using the segmentation method and b) an extrapolated inlet hematocrit of 16 %.

2.3.3 Velocity and flow rate measurements

As the flow is imposed through pressure control in the experiment and since the effective viscosity varies in channels due to hematocrit variations and aggregation, the flow rates in the different branches of the channel are not directly imposed. It is therefore necessary to measure the actual flow rate in each branch. For that, a velocimetry technique based on image processing is implemented. In order to measure the velocity, we use a method of time correlation that has been used in previous studies of RBCs suspensions in microfluidic flows, the dual-slit technique [61][63]. As its name suggests, it relies on the optical observation of two slits $s1$ and $s2$ at two different positions in the channel, the second slit being further in the channel than the first, according to the flow direction (Figure 2.8). As the cells pass by a slit in the channel, they modify the transmitted light intensity, leading to a varying signal over time, $S_1(t)$ from the first slit and $S_2(t)$ from the second slit.

$$S_1(t) = \sum_{(i,j)\in s1} frame_t(i,j) S_2(t) = \sum_{(i,j)\in s2} frame_t(i,j) \tag{2.13}$$

where $s1$ and $s2$ are the sets of pixels contained in the first and second slit respectively, and $frame_t$ the frame at the time t from the video. If the distance and the time separating the two slits in a straight channel are low enough, we can consider the same pattern of cells passing through the second slit will lead to nearly the same light modulation, as their configuration will stay the same. Then the technique consists in deriving the delay between both signals by locally comparing both signals by time-correlation, whose equation is :

$$C_n(\Delta t) = \sum_i S_{1n}(i + \Delta t) \times S_2(i) \tag{2.14}$$

where Δt is the studied time delay, expressed in number of frames, S_{1n} is the n^{th} sample of S_1 with the size $correlation_{window}$, such as :

$$S_{1n} = S_1[n; n + correlation_{window}] \tag{2.15}$$

We determine $\Delta t_M(n)$, the Δt such as $C_n(\Delta t_M(n)) = max(C_n)$, *i.e.* the abscissa of the maximum of the correlation. The length of the signal used for the correlation is defined here by the length of each sub-signal taken from the first slit to correlate with the whole signal from the second slit and thus extract the delay and then the velocity with the formula :

$$u_{dualslit}(n) = \frac{d.f}{\Delta t_M(n)} \tag{2.16}$$

where d is the distance between the two slits and f is the frame rate. The sub-signal from the first slit is then shifted one frame forward, keeping the same length and is correlated to the signal from the second slit, extracting a new velocity. This is done for all the sub-signals until the end of the signal from the first slit is reached. The result is an array of velocities (one for each sub-signal) and we keep the mean velocity over time of $u_{dualslit}(n)$ as the best approximation for the velocity of the cells in the channel during the experiment. This velocity is determined in each channel of the bifurcation for each recording.

When applying the dual-slit technique, several parameters have to be fit to get an accurate result, depending on experimental conditions namely the concentration of RBCs and the velocity range. Those parameters are the width w of the slits, the distance d between the two slits, the length $correlation_{window}$ of the signal used for the correlation and the delay range. They are determined empirically for each set of experiment, by trial and error, taking into account the following characteristics.

Width of the slits : The slits have to be wide enough compared to the frame rate and the velocity so the distance traveled by the cell between two frames is equal to or less than the width w of the slits. This ensures that all the cells are a least once in each slit. Thus :

$$w > \frac{u}{f} \tag{2.17}$$

where f is the frame rate and u is an approximation of the velocity made manually on one cell from the recording. In the few cases the approximation would be too low compared to the resulting velocity and the slit too thin to match this requirement, the width is adjusted and the processing is computed again to get a more accurate result.

However, if the slits are too wide, the signals will be a superposition of more fingerprints of moving cells remaining longer in the slit and whose arrangement may change when they do not all have the same velocity. This may make the signals from the first slit and from the second too different from each other to find significant correlations.

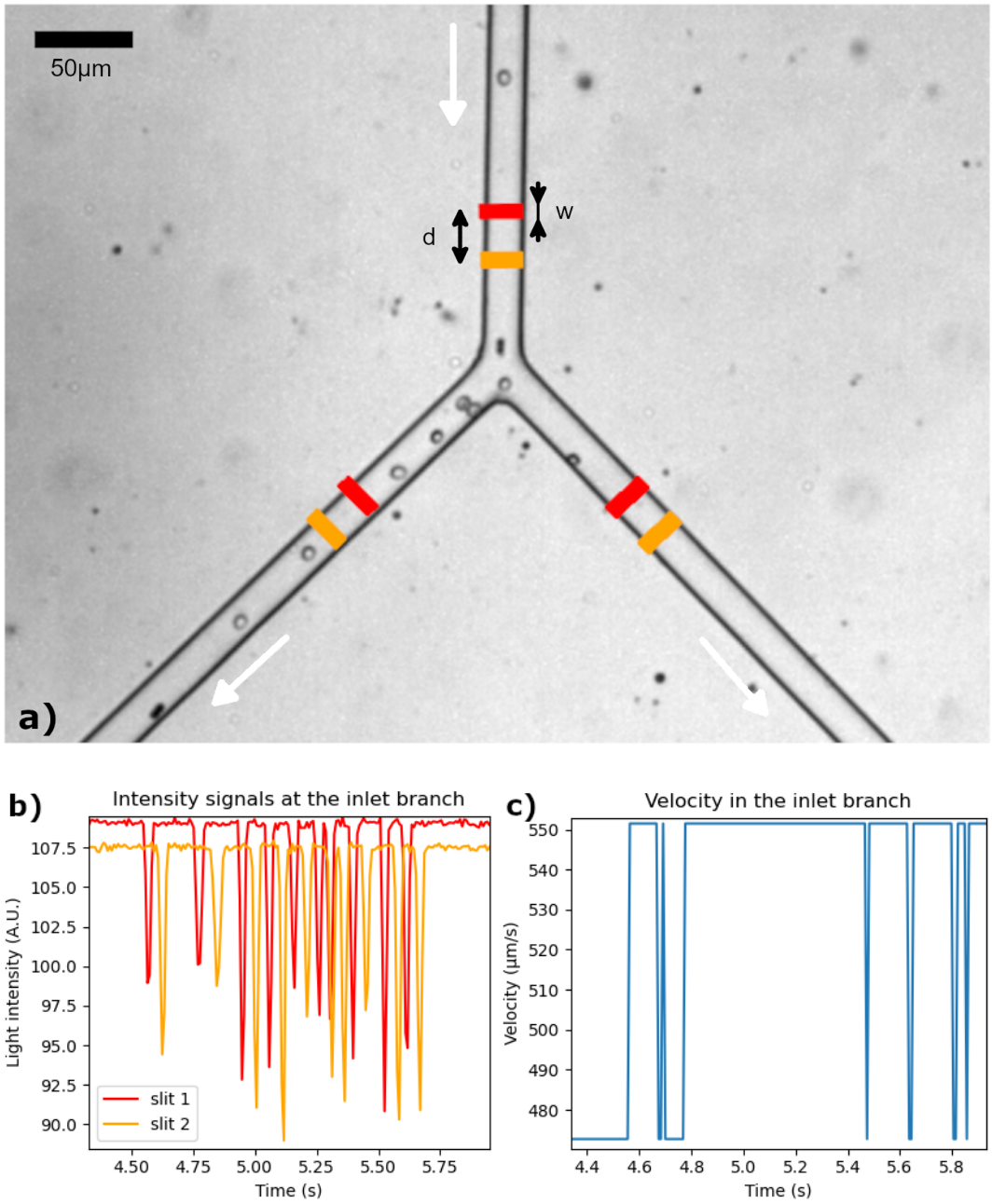

Figure 2.8: Illustration of the dual-slit technique. a) Frame from a recording. The white arrows indicate the sense of the flow. The velocity of the cells is measured in each channel. The red slits are the first encountered by the cells in each channel, the orange slits are the last. They all have the same width w, and the slits in the same channel are separated by a distance d. b) The sum of the intensity of each pixel in the slit is summarized and noted for each frame of the recording. A reversed peak in this example corresponds to the passage of a RBC in front of the slit. c) The instant velocity of the RBCs is generated by extracting the delay between the two signals. Finally, the mean of the velocity signal is considered as the velocity flow in the center of the channel.

Distance between the slits : In the same way, the bigger the distance between the two slits is, the more the arrangement of the cells varies between them. However, the measurement uncertainty is lower when the distance is higher. Indeed, the absolute uncertainty for any distance measurement is $\Delta d = \frac{1}{2}\ px = \frac{1}{2}.\frac{size_{sensor}}{magnification} = \frac{1}{2}.\frac{3.75}{4}\ \mu m = 0.47\ \mu m$. The absolute uncertainty for time measurement in our case is half the time between two frames so $\Delta t = \frac{1}{2}.\frac{1}{f} = \frac{1}{2}.\frac{1}{120}\ s = 0.004\ s$. We can define the uncertainty of the result of a division by :

$$\begin{aligned}
\Delta u &= \frac{1}{2}.(u_{max} - u_{min}) \\
&= \frac{1}{2}.\left(\frac{d+\Delta d}{t-\Delta t} - \frac{d-\Delta d}{t+\Delta t}\right) \\
&= \frac{1}{2}.\frac{(t+\Delta t)(d+\Delta d) - (t-\Delta t)(-\Delta d)}{(t-\Delta t)(t+\Delta t)} \\
&= \frac{1}{2}.\frac{2t.\Delta d + 2d.\Delta t}{t^2 - (\Delta t)^2} \\
&\sim \frac{1}{t} \sim \frac{1}{d}
\end{aligned} \tag{2.18}$$

Thus the uncertainty is inversely proportional to the distance used for the measure.

Length of the sub-signal : On one hand, if the sub-signal is too short, the pattern may not be unique and fit with several passages of cells on the second slit. On the other hand, the longer the sub-signal, the fewer trials of correlation are possible, making the resulting mean velocity less robust to noise.

Roman [61] shows that the velocity obtained using the dual-slit method equals the maximum velocity in a channel with a square cross-section, *i.e.* the velocity at the center of the parabolic-like velocity profile in a microfluidic channel (see part 1.2.2 Fluid dynamics). As previously stated, we aim to determine and study the influence of the flow rate Q, which cis related to the velocity by :

$$Q = w.d.\overline{u} \tag{2.19}$$

where d is the thickness of the channels, w the width of the channels and $\overline{u}$ the spatial mean velocity of the fluid in a section of the channel. As $w = 23$ µm and $d = 20$ µm are constant and the same for every channel of our bifurcation, the flow rate is then directly proportional to the mean velocity. Moreover, in our geometry the ratio between the maximum and the mean velocity is a constant. Indeed, in our straight microfluidic channel configuration, the Reynolds number is small and gravity is negligible (RBCs sedimentation is small compared to flow velocities), therefore the Navier-Stokes equation reduces to the unidirectional Stokes equation for an incompressible fluid :

$$\frac{\partial^2 u}{\partial y^2} + \frac{\partial^2 u}{\partial z^2} = \frac{1}{\mu}\frac{dp}{dx} \tag{2.20}$$

where μ is the viscosity of the fluid, p is the pressure in the channel and x is the axial vector parallel to the direction of the flow.

As this equation is linear, the solution u follows $u_{max}/\overline{u} = K$, where K is a constant depending only on the geometry of the channel [64]. For a straight channel with a circular section, $K = 2$ and in the case of a flat geometry ($w >> d$), $K = \frac{3}{2}$. In our case, for a rectangular section :

$$\frac{u_{max}}{\overline{u}} = K = \frac{48}{\pi^3}\frac{\sum_{n=1,3,5,\ldots}^{\infty}(-1)^{(n-1)/2}\left[1 - \frac{1}{cosh(n\pi b/2a)}\right] \times \frac{1}{n^3}}{1 - \frac{192a}{\pi^5 b}\sum_{n=1,3,5,\ldots}^{\infty}\frac{tanh(n\pi b/2a)}{n^5}} \tag{2.21}$$

where $a = \frac{w}{2}$ and $b = \frac{d}{2}$

The section of the channel is the same in each of the three branches of the bifurcation. The multiplicative constant is thus the same for the velocities in each branch. As previously said, the value given by the dual-slit technique corresponds to the maximum velocity in the channel. This means that the velocity in a daughter branch, normalized by the velocity in the mother branch, is the same, whether we consider the maximum velocities or the mean velocities, as is the flow rate in a daughter branch normalized by the flow rate in the mother branch.

2.4 Results

We aim to study the effect of aggregation on the known phase separation that occurs at microbifurcation. As previously stated (paragraph 2.1.1), the main cause for this phenomenon is the existence of the CFL, which we can directly observe in our recordings at low hematocrit. Indeed, our experiments follows the laminar regime, as the maximum Reynolds number is $Re = \rho.u.w/\mu = 1000 \times 25000.10^{-6} \times 23.10^{-6}/0.001 = 0.575 < 1$. We chose the density ρ and viscosity μ of the carrier phase, water. Figure 2.9 illustrates the average path of RBCs by showing the standard deviation of the image pixel value over 1000 frames (around 9 s). Thanks to the great length of the mother branch of the bifurcation, RBCs reach an equilibrium position at the center of the channel, with symmetrical CFLs on both sides. After the bifurcation, the RBCs follow trajectories according to the laminar flow and thus are off-centered toward the inner walls before eventually (further in the daughter branches) reaching again the center of the channel. Thus, after the bifurcation the CFLs are wider near to the outer walls.

The effect of aggregation can be seen qualitatively by comparing the fluxes of RBCs in daughter branches with and without aggregation, for a same flow rate ratio, as depicted in Figure 2.10. For approximately the same inlet hematocrit and for a flow rate ratio of 0.30 between the left branch and the right

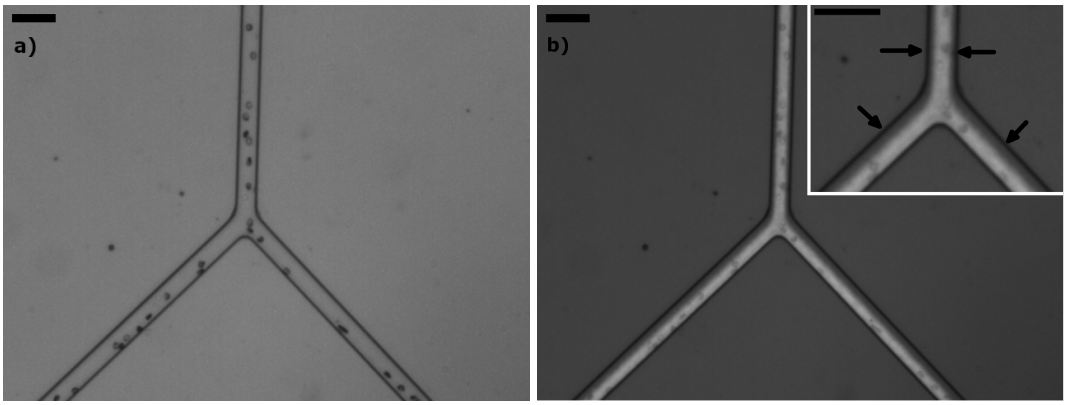

Figure 2.9: RBCs flowing through the microfluidic bifurcation. The picture (b) is a super-imposition of the picture (a) and the map of the standard deviation of pixel value over the full recording. We can visualise how the RBCs are centered in the mother branch, while they are close to the inner walls in the daughter branches. This highlights the cell-free layer (darker parts in the channels pointed by the arrows). The black scale is 50 µm long.

branch, the amount of RBCs going to the low flow rate branch is visibly lower when there is aggregation. Indeed, a quantitative measurement shows that the ratio of RBCs fluxes without aggregation is equal to 0.17, and is lower, equal to 0.13 when adding 30 mg/mL of Dex70.

Figure 2.11 show the studied ranges of inlet Ht and inlet velocities of RBCs. The Ht spans from 0 % to 16 %, with 90 % of the measurements below an Ht of 2 %. The velocity span from 27 µm/s to 28 mm/s, with 90 % of the measurements below 6 mm/s. We can roughly assume the shear rate $\dot{\gamma}$ at the wall by :

$$\dot{\gamma} = \frac{8u}{w} \tag{2.22}$$

Thus the shear rate is comprised between 10 s^{-1} and 10 000 s^{-1}, with 90 % of the measurements below 2 000 s^{-1}.

Figure 2.12 shows the results for 3 experiments ($N = 42$, $N = 17$ and $N = 41$ measurements respectively) without aggregation (blue) and for 2 experiments ($N = 49$ and $N = 52$ measurements respectively) with aggregation induced by 30 mg/mL of Dex70 (red). If blood was a perfect Newtonian fluid, then the result would be a straight line with a slope of 1, with $A = 0$, $B = 1$ and $X_0 = 0$. Naturally, and as we previously mentioned in paragraph 1.1.2, General rheological behavior of blood, the presence of cells and proteins disturbs such behavior. In a case where there is no aggregate and if we consider only the cell-free marginal layer model, where we assume there is no RBC in a layer of the size of the radius of an RBC r_{RBC}, that is roughly 4.0 µm. In this case, then $A = 0$, $B = 1$ and $X_0 = r_{RBC}/w \simeq 4.0/23 \simeq 0.17$. The relation between the normalized flux of RBCs and the normalized flow of blood is then linear, from the threshold $FQ_b = X_0$ to $FQ_b = 1 - X_0$. This simplified model corresponds to the piece-wise linear curve shown in Figure 2.12 (a).

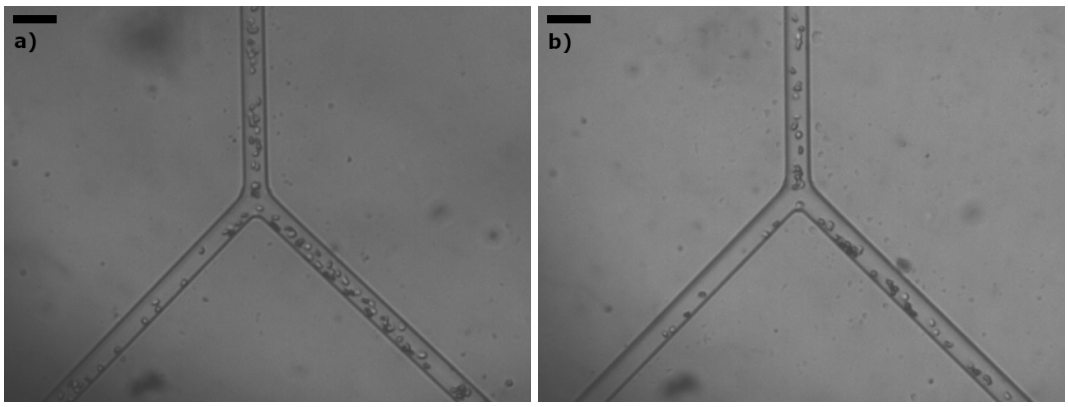

Figure 2.10: Typical example of the distribution of RBCs going through the bifurcation a) without and b) with aggregation in a dilute case. The black scale is 50 µm long. The ratio of the velocity in the left branch over the right branch is 0.30 in both cases. The flux of RBCs is however different, $J = 0.17$ without aggregation, $J = 0.13$ with aggregation, which illustrates that the aggregation enhances the phase separation (Zweifach-Fung effect) between the two branches.

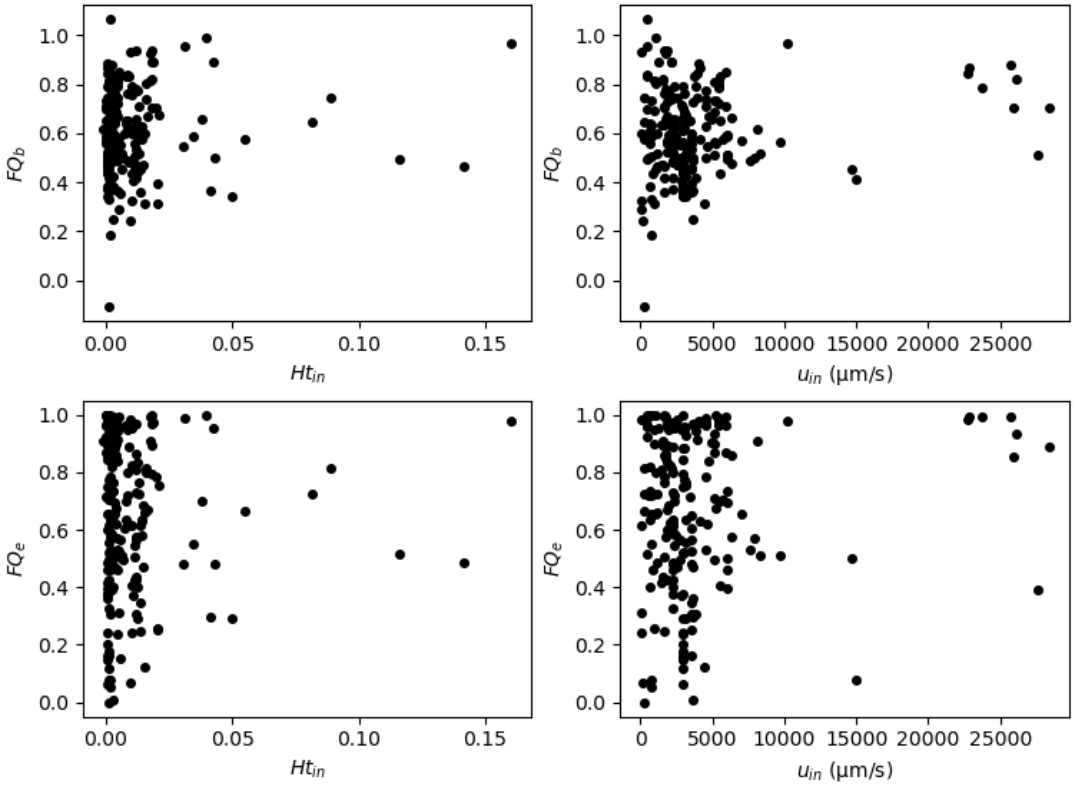

Figure 2.11: Variability of FQ_e and FQ_b depending on u_{in} and Ht_{in}. We notice there is no significant bias from the inlet velocity or hematocrit in the ranges we studied.

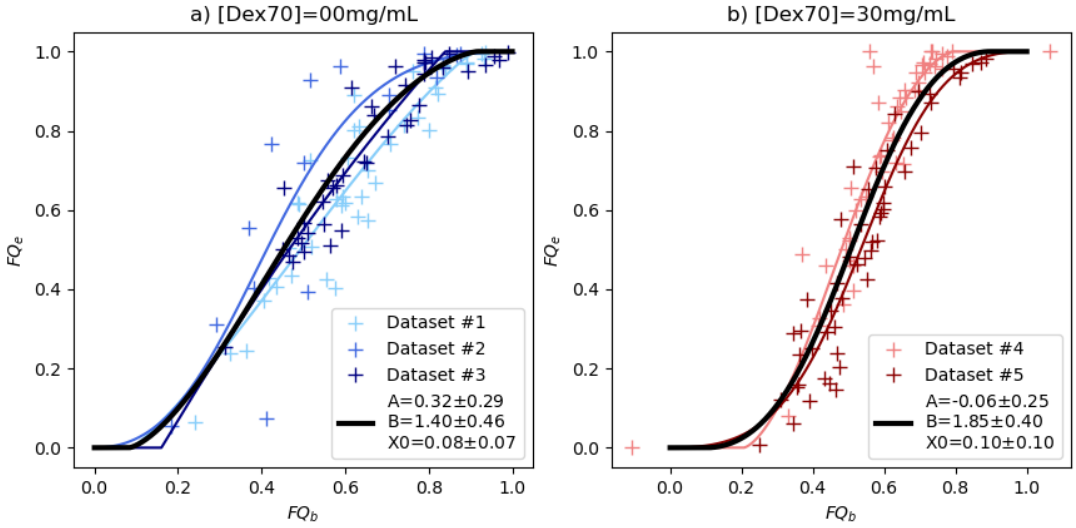

Figure 2.12: Measures of the flux of RBCs in one daughter branch normalized by the total flux of RBCs in both daughter branches, FQ_e, as a function of the flow rate of blood in the same branch normalized by the total flow rate of blood in both daughter branches, FQ_b. The black thick curves are the models corresponding to the equation 2.2, whom A, B and X_0 are the mean of the fitting parameters of each dataset (thin colored curves). a) Without aggregation for 3 different samples and chips with the same geometry ($N = 42$, $N = 17$ and $N = 41$ measures respectively). b) With aggregation [Dex70]=30 mg/mL for 2 different samples ($N = 49$ and $N = 52$ measures respectively).

The model proposed by Pries *et al.* (Equations 2.2 to 2.6) is more accurate than the simple model of the cell-free marginal layer. Their sigmoidal relation fits with the observed measurements, however depending on the conditions, their parameters are not always appropriate.

According to equations 2.4-2.6 established by Pries, Secomb, Gaehtgens, *et al.* [34] and defining D_f as the equivalent diameter of our channels with a rectangular cross-section, using the definition of hydraulic diameter [64], by $D_f = 4\mathcal{A}/P = 23 \times 20 \times 2/(23+20) = 21.4\ \mu m$ with $\mathcal{A}$ the area of the cross-section and P its perimeter, $A = 0$ as $D_\alpha = D_\beta$ in our case; $B = 1.32$ and $X_0 = 0.0187$. The measurements in a case without Dextran, and so without aggregation, match the theoretical model from Pries, Secomb, and Gaethgens [43] (Figure 2.13). However, with Dextran, then the sigmoid is more distinct and measured data deviate from the theoretical model.

To analyse more quantitatively the influence of aggregation on phase separation, we chose to observe the slope of the curve following Pries's model. Indeed, analyzing the slope of the sigmoid at the inflection point, which depends on all the parameters, allows for comparing the different curves in an easily understandable way. The higher the slope, the more pronounced the heterogeneity of the distribution and the more pronounced the Zweifach-Fung effect. Based on the equation 2.2, the slope equation is :

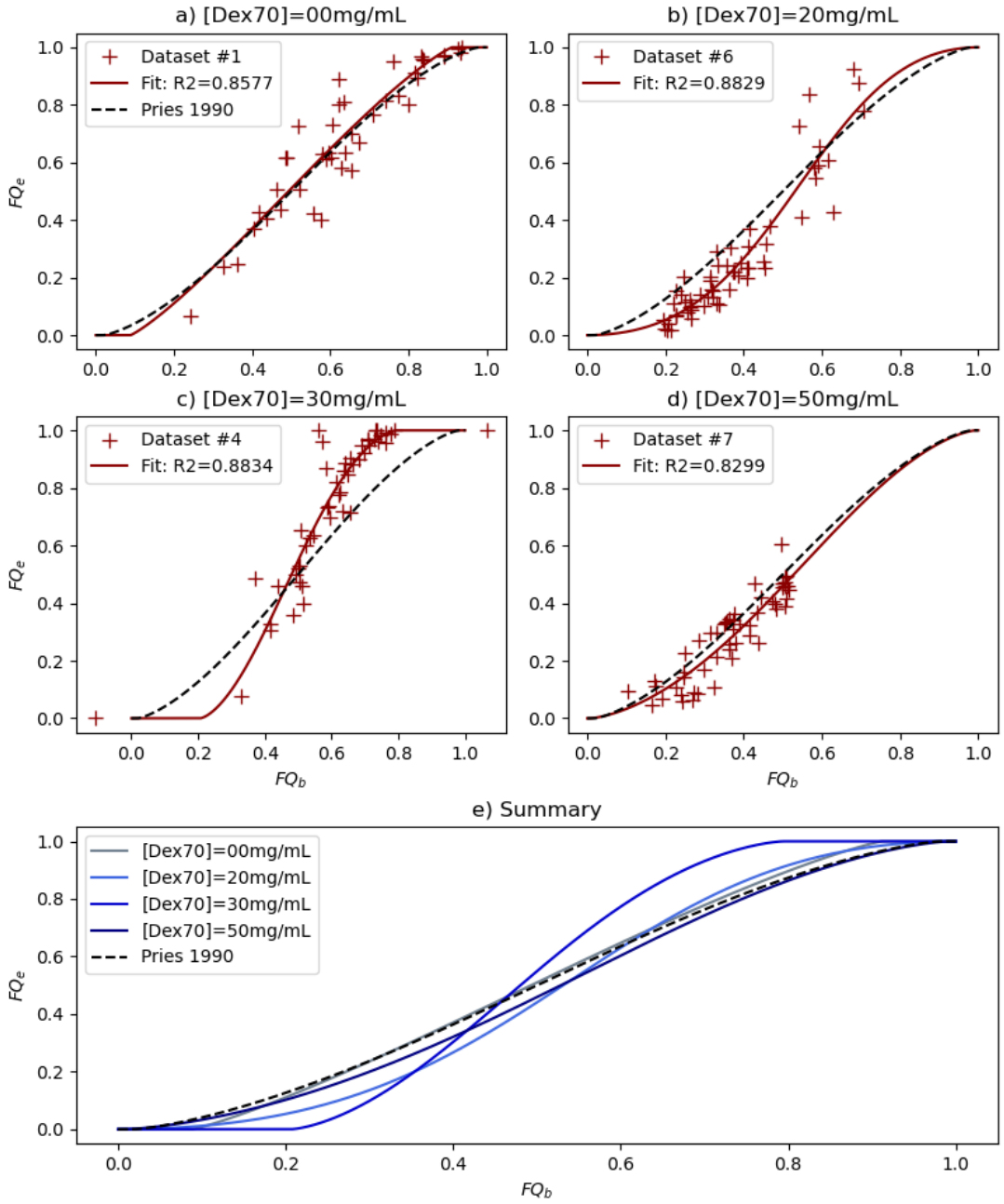

Figure 2.13: Comparison for different concentrations of Dextran 70 kDa of the flux of RBCs in one daughter branch normalized by the total flux of RBCs in both daughter branches, FQ_e, as a function of the flow rate of blood in the same branch normalized by the total flow rate of blood in both daughter branches, FQ_b. a) Without Dex70, b) [Dex70]=20 mg/mL, c) [Dex70]=30 mg/mL, d) [Dex70]=50 mg/mL. e) Comparison of sigmoidal fits using Eq.2.2 for different Dex70 concentrations. The dashed line represents the theoretical values using Pries, Secomb, Gaehtgens, *et al.* [34] model, with A=0, B=1.32, X_0=0.0187, D_f=21.4 µm, Ht=0.01

$$\frac{df(FQ_b)}{dFQ_b} = \frac{B\,(2X_0-1)}{(FQ_b-X_0)\,(X_0+FQ_b-1)} \times \frac{e^{-\left[A+B\times logit\left(\frac{FQ_b-X_0}{1-2X_0}\right)\right]}}{\left(e^{-\left[A+B\times logit\left(\frac{FQ_b-X_0}{1-2X_0}\right)\right]}+1\right)^2} \quad (2.23)$$

and the second derivative is :

$$\frac{d^2f(FQ_b)}{dFQ_b^2} = \frac{-B\,(2X_0-1)}{(FQ_b-X_0)^2\,(X_0+FQ_b-1)^2} \times \frac{e^{-\left[A+B\times logit\left(\frac{FQ_b-X_0}{1-2X_0}\right)\right]}}{\left(e^{-\left[A+B\times logit\left(\frac{FQ_b-X_0}{1-2X_0}\right)\right]}+1\right)^3} \times \left\{e^{-\left[A+B\times logit\left(\frac{FQ_b-X_0}{1-2X_0}\right)\right]}\left[-2B\,(2X_0-1)\right] + \left(e^{-\left[A+B\times logit\left(\frac{FQ_b-X_0}{1-2X_0}\right)\right]}+1\right)\left[B\,(2X_0-1)-1+FQ_b\right]\right\} \quad (2.24)$$

Although, to find the inflection point, finding the analytical expression of the root of the second derivative of $f(FQ_b)$ for any A, B, X_0 is exceedingly complex, looking for a numerical value of the said root for a specific set of parameters is more straightforward, using the python function *fsolve* from the library *scipy*. Knowing the FQ_b value of the inflection point, we can then compute the slope of f.

Table 2.1 provides a comprehensive summary of the diverse experimental conditions, fit parameters, and slopes at the inflection point for the various datasets. Notably, the parameter X_0, which is linked to the presence of the CFL, demonstrates an intriguing trend, exhibiting a peak at a Dex70 concentration of 30 mg/mL (Figure 2.14). It is worth mentioning that X_0 does not directly reflect the width of the CFL, as the intensity of heterogeneity in the distribution of RBCs relies also on the other parameters of the sigmoid curve. Examining the slope a of the curve at the inflection point, which depends on all these parameters, reveals a clear increasing trend as the Dex70 concentration increases up to 30 mg/mL, followed by a maximum around this concentration and then a subsequent decrease as Dex70 concentration further increases. Several sources [28][19][57] agree on such a bell-shape in the relation between the Dextran 70kDa concentration and the aggregation force. However, the values and the concentration of Dex70 associated with the maximal aggregation force appear to exhibit some variation based on factors such as temperature, measurement techniques, and hematocrit. Specifically, while Flormann, Aouane, Kaestner, *et al.* [57] reported a higher aggregation at 50 mg/mL of Dex70, Neu and Meiselman [28] and Steffen, Verdier,

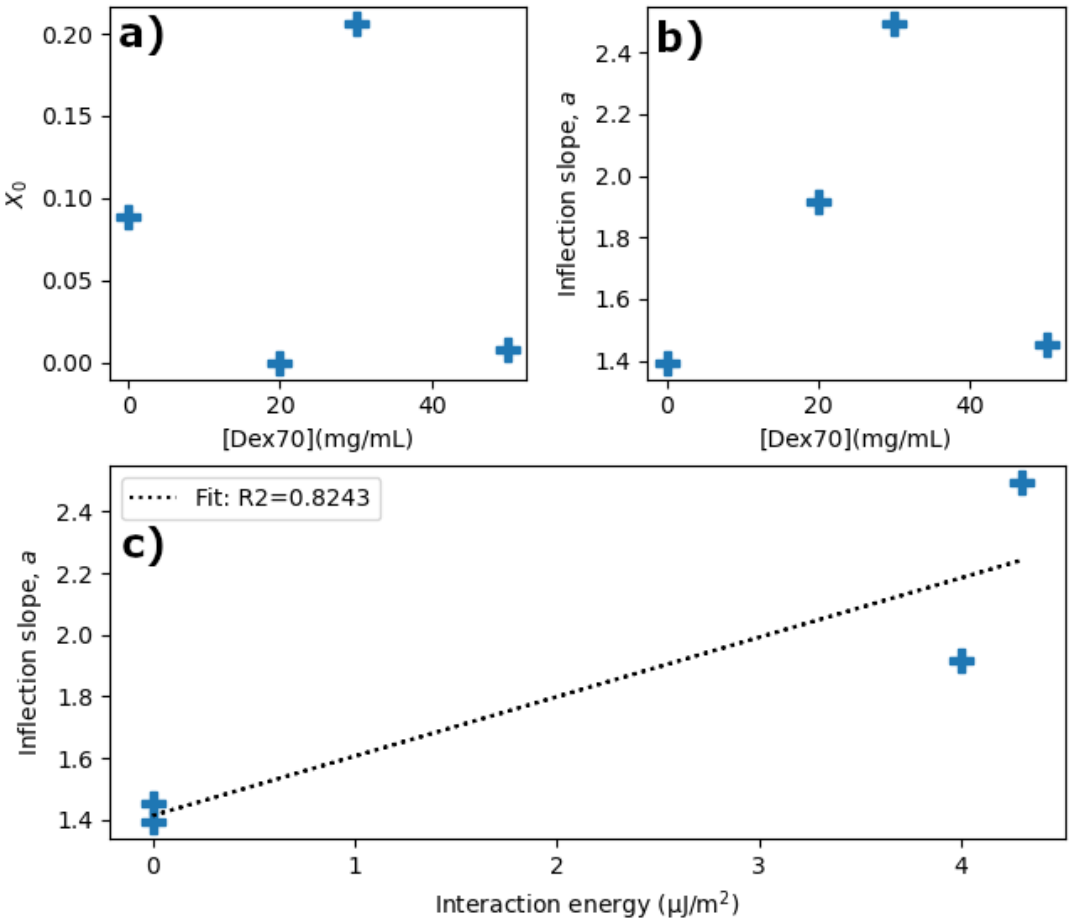

Figure 2.14: Influence of aggregation on the sigmoidal fit parameters. a) Fit parameter X_0 according to equation 2.2 as a function of the Dex70 concentration. Slope of the sigmoidal fits at the inflection point for the different concentration of Dex70, b) as a function of the Dex70 concentration and c) as a function of the interaction energy of aggregation according to Neu and Meiselman [28]. The dashed line is guide for the eye.

Dataset #	A	B	X_0	**slope**	**sample** Ht **(%)**	**[Dex70] (mg/mL)**	**Donnor**
Pries	0	1.323	$1.870{\cdot}10^{-2}$	1.374	1	-	-
1	$3.983{\cdot}10^{-2}$	1.146	$8.834{\cdot}10^{-2}$	1.394	1	0	A
2	$7.227{\cdot}10^{-1}$	2.037	0.000	2.122	0.5	0	B
3	$2.047{\cdot}10^{-1}$	1.009	$1.603{\cdot}10^{-1}$	1.469	5	0	C
Mean	$3.224{\cdot}10^{-1}$	1.397	$8.287{\cdot}10^{-2}$	1.720	-	0	-
4	$1.977{\cdot}10^{-1}$	1.453	$2.060{\cdot}10^{-1}$	2.493	1	30	D
5	$-3.118{\cdot}10^{-1}$	2.255	0.000	2.268	2	30	E
Mean	$-5.708{\cdot}10^{-2}$	1.854	$1.030{\cdot}10^{-1}$	2.336	-	30	-
6	$-2.383{\cdot}10^{-1}$	1.905	0.000	1.915	1	20	F
7	$-1.642{\cdot}10^{-1}$	1.420	$7.465{\cdot}10^{-3}$	1.452	7	50	F

Table 2.1: Comparison of numerical values describing the distribution of RBCs at the bifurcation. A, B and X_0 are the fit parameters according to equation 2.2. The slope represents the slope of the fitting curve at the inflection point, described by equation 2.23. The sample Ht is the hematocrit in the inlet tank. [Dex70] is the concentration of Dextran 70kDa in the inlet tank. The rows named "Mean" indicate the mean fit parameters A, B and X_0 for a same concentration of Dextran and the slope of the theoretical fitting curve using these fit parameters.

and Wagner [19] observed the maximal aggregation at 30 mg/mL, aligning well with our observations on RBCs distribution.

As source of comparison, Neu and Meiselman [28] offer a model with the same characteristics by considering the depletion interaction and the electrostatic interaction between two RBCs, depending on the Dex70 concentration (Figure 1.6). Using this model, Figure 2.14 (bottom) shows the slope of the sigmoid at the inflection point depending on the approximated interaction energy. As previously stated, the higher the slope, the more pronounced the Zweifach-Fung effect is. We notice that when the interaction energy between two RBCs increases, then the aggregated cells will go more largely through the daughter branch with the higher velocity.

2.5 Discussion

Thanks to our *in vitro* approach, by tuning the pressure drops at the outlets, we mimic different layouts of capillaries network after the bifurcation. The relation between the ratio of flux of RBCs and the ratio of flow rates in the outlets being non linear, we have highlighted the Zweifach-Fung effect in this kind of configuration, by imposing asymmetrical pressures at the outlets. In agreement with our speculation, we have demonstrated, by varying the concentration of Dex70 in our medium, that the magnitude of this effect is strongly influenced by RBC aggregation : the Zweifach-Fung effect is amplified when the aggregation between RBCs is stronger.

Although the size and aspect ratio (20×23 µm) of our microbifurcation are closer to a physiological configuration than in previous studies of the effect of aggregation on the RBC distribution [65], the channels are still slightly wider than capillaries of the microcirculation (typically between 5 to 10 µm). As by nature the Zweifach-Fung effect is more pronounced when the ratio of particle size to channel size increases, we suspect that the effect we observed in our specific case would be even stronger in smaller capillaries. Furthermore our microfabrication method limits the channel geometry to rectangular or square sections, which not fully replicate physiological conditions, where circular sections are more appropriate. Although the channel edges could influence the cell-free layer and the resulting numerical values, the extent of their impact in a capillary of this size remains uncertain. While the underlying trend is expected to persist, it becomes pertinent to explore various shapes and sizes of channels to quantify potential differences.

Our experiments have been limited at relatively low hematocrits (<15 %) notably by the refraction that can occur when several RBCs overlap on the transverse axis, which became frequent at higher Ht. In order to experiment at higher Ht, it could be considered to use a fluorescent cell dye such as fluorescein. The presence of a dye on the cells membrane would potentially modify the aggregation but would presumably be a more accurate measure of the Ht. Thus creating a calibration curve between the measurement on the equipment in brightfield and in fluorescence would allow to adjust our measures made with the Beer-Lambert like relation. Additionally, the use of a blue light source or a filter could enhance the contrast, as hemoglobin absorbs light at the same wavelength, potentially cancelling this effect.

It is noteworthy to mention that in the present study, we have focused on a symmetrical Y bifurcation configuration. Although this design allowed us to investigate the influence of Dextran-induced aggregation on RBC distribution, we acknowledge that the effect of different geometries and angles of bifurcation remains unexplored. In future investigations, employing the same analytical methodology, we could systematically study the impact of these parameters on RBC distribution within microbifurcation networks, where the succession of bifurcations and junctions could lead to new behavior (Figure 2.15).

Compared to physiology, the dimensions of our channel is closer to the size of a venule (diameter $\approx$ 20 µm), about two times the width of a capillary. The mean of our studied velocities, and therefore shear rate, of RBCs are slightly higher than those observed in venules (2 mm/s) and blood capillaries (1 mm/s), yet our experiment covers the physiological ranges and does not present any significant bias from the inlet hematocrit and the velocities applied to the observed fluxes of RBCs ratio (Figure 2.11). Higher shear rate means the clusters of RBCs are more likely to break [67][68]. Although these previous work assume a minimal aggregation in capillaries because of the high shear rate, our analysis demonstrated that aggregation still occurs in such conditions, and affects the microcirculation. This is in accordance with previous works [69][57].

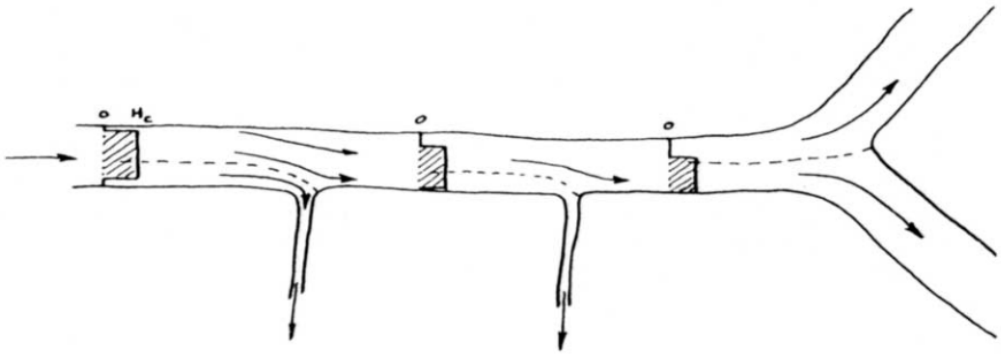

Figure 2.15: Blood flow through a series of small diameter arterial-type bifurcations, showing an idealized hematocrit distribution at various axial positions. Reprinted from Cokelet and Meiselman [66].

Preliminary experiments have been conducted on *in vitro* capillary networks with channels of varying widths, including 20 µm wide channels [52] and others of different widths [53]. These investigations have consistently highlighted the intrinsic heterogeneity of RBC distribution within such networks, arising partly from the existence of a CFL even in the absence of aggregation. The findings of our study suggest that this effect is further amplified depending on the level of aggregation. Moreover, theoretical studies focused on microcirculatory networks have postulated that the flux of RBCs can dynamically vary over time, giving rise to curious behaviors such as oscillations or bistability states [70][71]. Their simulations account for the spatial and temporal variation of viscosity, influenced by the mean hematocrit in a cross-section and the laws governing plasma skimming at bifurcations. Given the demonstrated influence of aggregation on these dynamics, our findings can potentially modify and refine these theoretical models. Consequently, in pathological scenarios involving altered RBC aggregation or variations between individuals, the multistability and oscillation states behavior in blood microcirculation could be significantly impacted. This paves the way for understanding and interpreting blood flow dynamics in complex microvascular systems, shedding light on the potential implications of RBC aggregation in various physiological and pathological contexts.

Chapter 3

Image processing in flow cytometry: RBC shape classification by a deep-learning technique

3.1 Introduction

Cytological blood analysis is a versatile method of diagnosis for various diseases such as anemia or thrombocytosis [72], through the examination of the concentration, the morphology or the labeling of the different blood cells. Those inspections are often realized by hand, on a relatively small sample volume of blood. In the case of the detection of rare cells, as circulating tumor cells (CTCs), the risk of a false negative diagnostic is not negligible. Consequently, there has been a surge of interest for the development of automatized processes. One can identify and compare two approaches : recording of flowing cells through microscopy and methods such as cytometry. Both approaches rest on the analysis of flowing cells in microchannels.

Flow cytometers are very powerful tools for high throughput cell analysis, achieving count rates of up to 10^6 cells per second [73]. For detection, single cells flow through a capillary and pass a highly localized optical excitation spot. Scattering and fluorescence signals, for fluorecent cytometers, are then collected by well-aligned lenses and routed to different light sensors to differentiate measurement parameters such as forward- and side-scattering as well as the optical wavelength in case of fluorescence. Eventually, the combination of these parameters gives information on the cell type and/or its characteristics. Coulter counter [74] achieves detection of cells using impedance variations and recent adaptation uses radio frequency [75]. Due to their size and mechanical susceptibility, high throughput flow cytometers (HTFCs) are restricted to laboratory use ensuring well-defined environmental conditions. Besides costs, size and susceptibility, HTFCs lack the ability of single-cell imaging due to the optical measurement principle. For this reason, complementary solutions such as scanning microscopy or imaging flow cytometers exist [76]. However, these techniques are highly limited in throughput due

to mechanical actuation or the frame rate of state-of-the-art cameras. For instance, imaging flow cytometers achieve maximum event rates of 10^4 s^{-1} [77][78][79] under specific conditions, even if this threshold can be overcome by performing parallelization [80][81].

To overcome the throughput limitation due to the camera, techniques using a simple light sensor appeared during the past decade using a pulsed LASER as light source and a sophisticated optical set-up [82][83][84], which in principle could allow to improve acquisition rates by several orders of magnitude. We here propose a concept which combines an optical spatial amplitude modulation scheme with artificial intelligence to simultaneously allow for high throughput single-cell detection and shape reconstruction in microfluidic flow.

Our approach follows a low cost, highly robust implementation, requiring a minimum of optical elements. The technique could potentially be integrated into a disposable microfluidic chip. The key idea of our method is to use a binary amplitude mask consisting of transparent (1) and opaque (0) areas, which is placed in between a microfluidic channel and a light sensor (Figure 3.1 (a)). The setup is illuminated by a collimated light source similar to a brightfield microscope.

Some studies consider a similar light modulation and machine learning reconstruction approach, using a camera [85][86] or time-consuming sequential scanning procedures with digital masks [87]. In addition, while the object must be almost static using these techniques, we take advantage of a moving object to perform the scanning. When passing the detection zone, the light intensity is spatially modulated by means of refraction and attenuation according to the shape and structural details of the cell and the particular pattern of the slits mask. Thus, the obtained signal for each passing cell corresponds to the correlation of its brightfield image and the particular pattern of the mask. These "fingerprints" encode the main morphological characteristics, allowing the recognition of each passing object although fine image details are widely waived. Therefore, any sophisticated relay optics can be relinquished and a fast photodiode is sufficient to receive the highly simplified, intensity-modulated signals.

A deep learning convolutional neural network (CNN) was built by Kihm, Kaestner, Wagner, *et al.* [88] in order to classify, from their pictures, RBCs according to their shape. They were able, thanks to the use of convolution kernels, to extract geometrical features from the shapes of the cells. Their ANN allocates a shape score to the input pictures to set them on a shape spectrum, from slipper to croissant (see paragraph 1.2.2) including intermediate shapes. Our first goal was to automatically classify the RBCs in a similar way, from the fingerprints described above, instead of the pictures of the cells. Then we pushed the concept one step further by using a comparable approach to find back the shape of the cells from the fingerprints.

The modulated signal from the light sensor is decoded by means of a deep learning artificial neural network (ANN) for cell image reconstruction at high

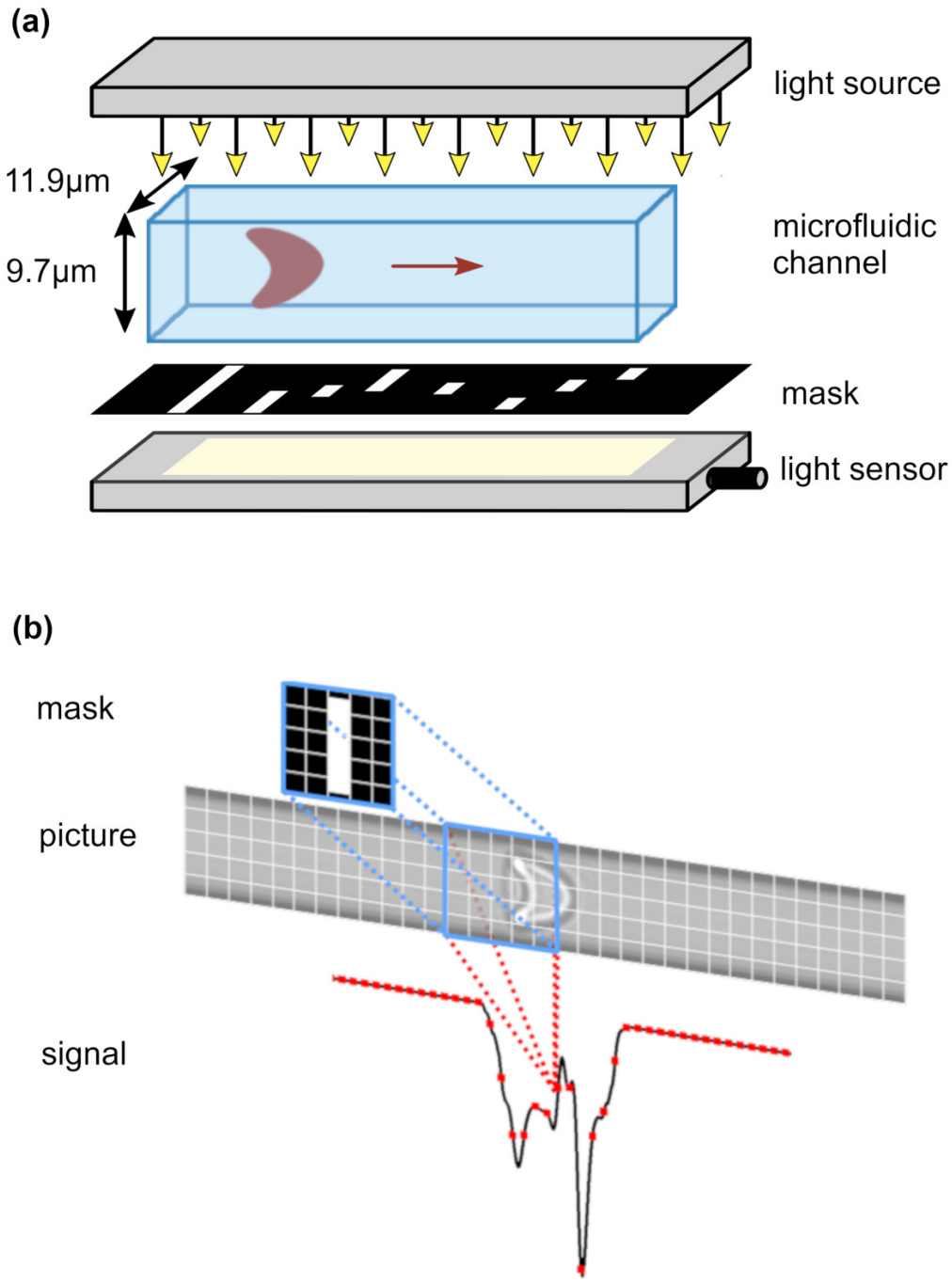

Figure 3.1: Illustration of the signal acquisition. a) Single cells in a microfluidic channel of size 11.9 $\mu m \times 9.7\,\mu m$ are passing the optical detection zone. In the simulated setup, the cells are illuminated by a collimated light source and the transmitted light is modulated by a binary amplitude mask that is placed in between the channel and a simple light sensor. b) To implement a mimicked binary mask between the cell and the sensor, we superimpose a black pattern onto the respective bright-field image. Simulating the signal obtained from a light sensor is equivalent to integrating the light intensity of all pixels of the image. The image is then shifted of a distance Δx while the mask remains in the same position to retrieve the new global light intensity as if the cell is crossing the field of view. In our case, this process is equivalent to computing the horizontal correlation between the picture and the mask.

level of detail. This approach can be compared to replicating auto-encoders which, for instance, are used for "deepfake" [89] or texture swapping [90]. The mask acts as an encoder to compress the cell morphology to obtain a characteristic fingerprint or feature map. In contrast, the ANN acts as a decoder to recover the cell image. Therefore, the ANN mimics the optical transfer function of a real microscope, including optics and camera. Once the system is trained according to a real setup, further implementations can be highly simplified, relinquishing any sophisticated optics. This promises a high potential for miniaturization. Moreover, the method allows for high throughput sample imaging, which is limited by the bandwidth of the sensor, the sample rate of the data acquisition system and the expected signal-to-noise-ratio.

3.2 Materials and methods

A major part of this work has been published in our article Martin-Wortham, Recktenwald, Lopes, *et al.* [91].

Most of the study in this chapter is based on pictures of single RBCs flowing through a straight microchannel. A complete image dataset, containing normalized pictures of croissant-shaped or slipper-shaped RBCs and various intermediate shapes, was made by Kihm, Kaestner, Wagner, *et al.* [88] to create an automatic shape classifier for RBCs. Those standardized pictures are well-suited for the training of an ANN, therefore the development of our image reconstruction ANN is based on them. Unless specified otherwise, the following paragraphs in 3.2 describe from Kihm, Kaestner, Wagner, *et al.* [88] the experiment to obtain these pictures.

3.2.1 Chip design and fabrication

The geometry of the microfluidic chip contains an inlet, an outlet, and several parallel channels of different width in between. All the images for this study were taken in the same channel, whose width was 12 µm and depth was 10 µm. This configuration provides a constriction factor for which two equilibrium shapes of RBCs appear, which is well-suited to illustrate the image reconstruction. From the chip design, a mold was made using photolithography, in a similar way as in part 2.2.1. The first step consisting in pouring the resin on a wafer is the same. The UV exposure, however, varies. Here, a UV opaque mask is placed between the resin and a UV light source. The pattern of the channels is drawn in negative on the mask, making it transparent to UV. The exposed parts polymerize as previously described and remain after developing, leading to a mold ready to be used for PDMS molding.

Epoxy molds During the development and test of our CNN, we used pictures to generate the fingerprints. In order to check if this approach is close enough to reality, we tested our process on videos of cells circulating in the same channel as was used to produce the reverence (training) database. The

chips in these experiments were fabricated using an epoxy replica of the original silica mold. From a PDMS cast of the channels, we can make a replica mold with Epoxy [92]. As Epoxy is cheaper and sturdier than a silica wafer, it highly increases the re-usability of the mold. Briefly, this consists in pouring the two Epoxy reactants (R123 resin and R614 hardener) in a petri dish and placing the PDMS cast face down on the Epoxy. Few days later the Epoxy has hardened, the PDMS can easily be removed and the new Epoxy mold can be used as if it was a silica and resin mold, by filling it with new PDMS for the chip. More information about the replication protocol can be found in the work of Heuzé, Collin, Terriac, *et al.* [92].

3.2.2 Blood sample preparation

In the work of Kihm, Kaestner, Wagner, *et al.* [88], the RBCs used for the experiment are extracted from human blood. A drop of blood is taken from the donor using a sterilized needle, commonly used by patients with diabetes. The drop is put in a 1.5 mL Eppendorf tube with 1 mL of PBS. The sample is then centrifuged at 1500 rcf for 5 minutes. The supernatant and the buffy coat are replaced by PBS. This step is repeated two more times to clean the RBCs of platelets, WBCs and proteins. Packed RBCs are taken from the bottom of the tube and resuspended at 1 % hematocrit (Ht) in a solution of PBS and BSA 0.1 % (see more about BSA at paragraph 2.2.2).

3.2.3 Experimental set-up

The RBCs are pumped through the microfluidic chip using a pressure driver (Elveflow OB 1Mk II) at different pressure drops. PTFE tubing is used to connect the tank to the microfluidic chip. The observation is made with an inverted microscope and a 60-fold oil-immersion objective (Nikon CFI Plan Fluor, NA = 1.25, and a camera (Fastec HiSpec 2G) recording at 400 fps [88].

3.2.4 Picture normalization

Kihm, Kaestner, Wagner, *et al.* [88] normalize their images by cropping them at a size of 90×90 px. The top and bottom borders of the pictures are then smoothed using a Tukey window. Finally, pixel values are re-scaled so that 1 % of the lowest pixel values saturate at 0 and 1 % of the highest saturate at 255.

3.2.5 Brightfield and darkfield approach

In order to test an alternative method for imaging and to evaluate the sensitivity of the method to different types of illumination that may be implemented in final applications, we selected a second approach that simulates darkfield microscopy. Whereas brightfield microscopy permits most of the light to pass through the sample, darkfield imagery blocks most of the transmitted light

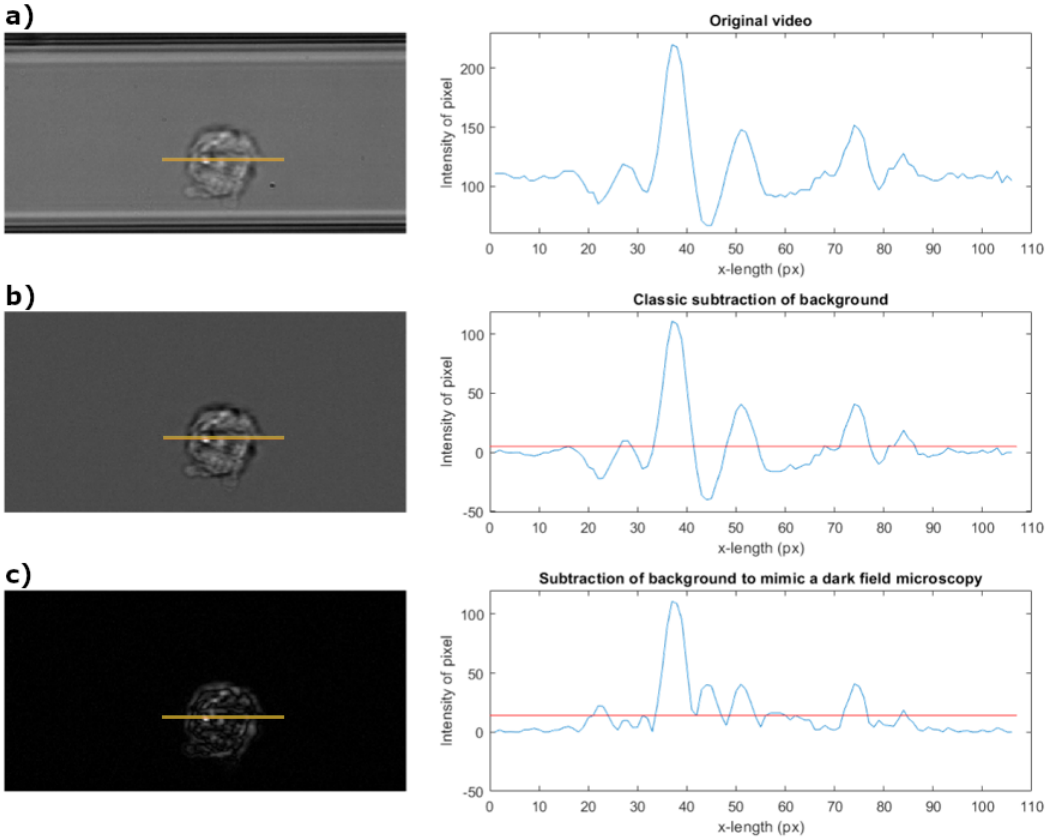

Figure 3.2: Methods of background subtraction from a) a video frame of a damaged leukemia cell leading to a mimicked b) brightfield or c) darkfield picture. The signals on the right are the intensity levels on the respective cross-sections, marked in yellow on the pictures. The red thresholds represent the mean signal value from the brightfield cross-section and the darkfield cross-section respectively.

and only allows oblique light rays to pass through the sample. This configuration results in a highly contrasted image with a dark background. In this case, the processing slightly differs. We have simulated a darkfield image from a brightfield one through the implementation of a computational algorithm that subtracts the image's median and takes the absolute values of the resulting difference (Figure 3.2).

3.2.6 Comparison between picture and video

We are studying moving cells in a stable state (steady shape). Therefore, the morphology and position of the cell will significantly remain the same during its passage in front of the ROI. Hence, instead of using heavy videos of RBCs flowing in the channel, we create a virtual sequence of sub-images from a single picture of the cell, by shifting the cell forward, with a step of one pixel (0.13 µm). It effectively consists in replacing a time sequence obtained by recording cells traveling across the measurement window by a scan of a fixed image from front to back along the flow direction. To validate this process of creating signals from pictures of RBC instead of videos, we compared

the signals obtained with the slit mask from pictures of parachute RBCs using correlation and from recordings of RBC actually flowing through the channel. We then used a very high speed camera (Photron, Fastcam SA5). We chose to make this comparison in darkfield as we noticed characteristic elements of the curves are more distinguishable for the naked eye than in brightfield. Figure 3.3 shows that the signals from the videos exhibit high frequency variations, due to the noise of the camera. The sampling frequency between videos and pictures differs because of the differences in processing. On one hand, the sampling frequency from videos is defined by the frequency of the camera (10 000 fps). On the other hand, the sampling frequency of the pictures' signals relies on the spatial resolution of the camera (0.16 µm/px). Despite these differences, for a similar number of studied RBCs, the fingerprints, represented by the mean signals, are sensibly the same. Indeed, the distinctive elements of the fingerprints for the parachute RBCs, *i.e.* the two peaks with an increase of amplitude, remain identifiable and the mean curves from the single pictures are in range of the standard deviation envelope of their corresponding signals from full videos. Therefore the approximation made by using pictures and correlation to simulate the signals is close to what would be obtained by using videos.

3.3 Mask for classification

The underlying principle of our technique relies on the use of a mask, positioned between the channel and the sensor, to encode the visual information of a cell passing the detection zone. This mask, consisting of opaque and transparent regions, will spatially modulate the transmitted light, resulting in signals that exhibit a strong dependence on the specific pattern of the mask, as well as the intrinsic properties and velocity of the passing cell. This part describes the design process employed to chose a mask pattern capable of generating unique fingerprints, enabling the classification of RBCs based on their morphological characteristics.

3.3.1 Mask simulation

This study serves as a proof-of-concept, necessitating the utilization of a high-speed camera to accurately assess the results by comparison between the classification of the fingerprints and the classification of the actual pictures of the cells. Furthermore, in order to conveniently evaluate various mask patterns during the different steps of this work, a simulation approach is employed during the post-processing stage, avoiding the fabrication of multiple masks.

Correlation To simulate the presence of the binary modulation mask in between the channel and the sensor, we pixelwise multiply the binary mask pattern (black and white) with each sub-image from the ROI. Thus, optically blocked areas are multiplied with zero and non-blocked areas are multiplied with one. Subsequently, the sensor signal of a virtual photodiode is obtained

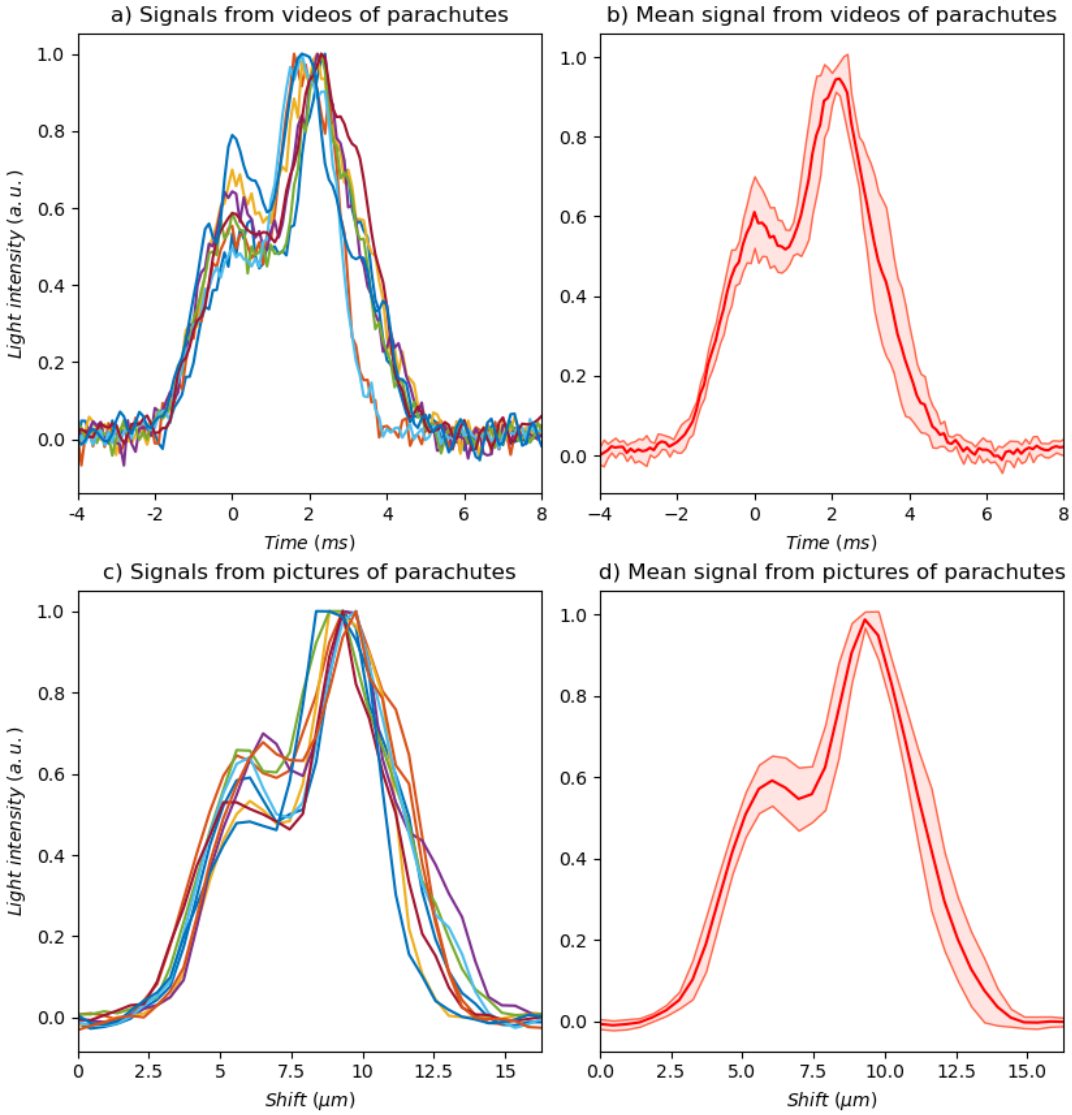

Figure 3.3: Comparison of parachute signals obtained from videos and from pictures, in darkfield, using a 3-pixel (0.4 µm) wide slit mask. a) Signals obtained by numerically superimposing a mask on 8 videos of parachute shaped RBCs flowing in the channel. b) Mean signal from a) where the semi-transparent envelope represents the standard deviation. c) Signals obtained by mimicking, with an increasing shift, the trajectory of 9 parachute shaped RBCs from pictures. d) Mean signal from c) where the semi-transparent envelope represents the standard deviation.

by integrating the intensity over all pixels of each masked sub-image, corresponding to the total transmitted light of the mask. By shifting the cell picture by Δx relative to each sub-image in the x-direction, the movement of the cell is simulated (Figure 3.1 (b)). For each discrete shift, a new intensity value results and the obtained sequence corresponds to the correlation signal $S(\Delta x)$, which is defined as :

$$S(\Delta x) = (M \otimes Y)(\Delta x) = \sum_{j=0}^{W_c-1} \sum_{i=0}^{L_c-1} M(i + \Delta x, j) \times Y(i, j) \tag{3.1}$$

where M denotes the array representation of the binary mask and Y the cell sub-image. L_c corresponds to the length of the cell image and W_c to its width in pixels. Δx denotes the relative shift. The variations of the correlation result, due to border effect, known as correlation transients are suppressed by padding with the median of the image. Additional signal parts due to padding are then truncated after correlation. The resulting correlation sequence, or fingerprint, has a length of $L_m + L_c - 1$, where L_m corresponds to the length of the mask.

Since the cell-characteristic fingerprint $S(\Delta x)$ highly depends on the used binary mask design M, we use several mask patterns to test our approach (Figure 3.4). As we want to compare the efficiency of the patterns for the same field of view, all masks exhibit the same size of 90 px (width) $\times$ 256 px (length) or 11.9 μm $\times$ 33.8 μm.

Final signals The signals $S(\Delta x)$ in Figure 3.4 are generated for six different mask designs and tested with 50 different parachute shapes of RBC (red) as well as 50 different slipper shapes (blue) in brightfield. The statistical mean value for these stable shapes is plotted as a solid line for each mask and cell type, the respective standard deviation is indicated as a semi-transparent envelope.

All signals tend to decrease in amplitude when the RBC enters the ROI. This is due to the fact that the light is refracted and attenuated with respect to the void case. It is remarkable that depending on their features and symmetries some masks create similar waveforms for parachutes and slippers, (Figure 3.4 (a), (c)-(e)), while other patterns create signals which are clearly different (Figure 3.4 (b), (f)).

3.3.2 Signals classification by convolution

The first design truly considered was the single slit, because of its simplicity and the noticeable difference between the signals for the parachute RBCs and the slipper RBCs in darkfield (Figure 3.5 (a)).

As a further examination, we attempted to automatize the classification of the cell shape using the fingerprint obtained from the picture and correlation, using the single slit mask (Figure 3.5). A reference fingerprint was made

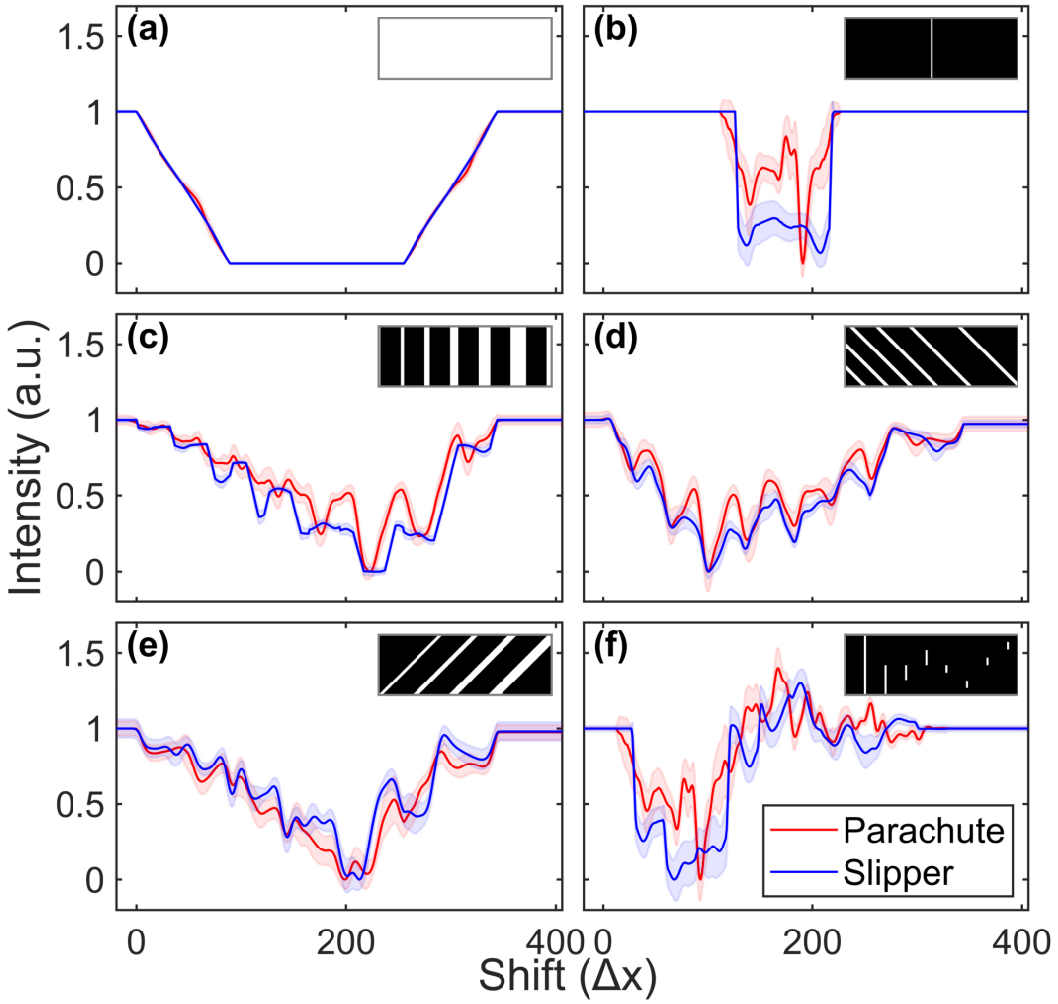

Figure 3.4: Characteristic fingerprints from red blood cells crossing the binary modulation mask. The shown signals express the average of each 50 parachutes (red) slippers (blue), the standard deviation is indicated by a semi-transparent envelope. The mask patterns used are : a) blank (no mask), b) 3-pixel slit (0.4 µm), c) chirp, d) tilted stripes, e) tilted chirp, f) barrel organ.

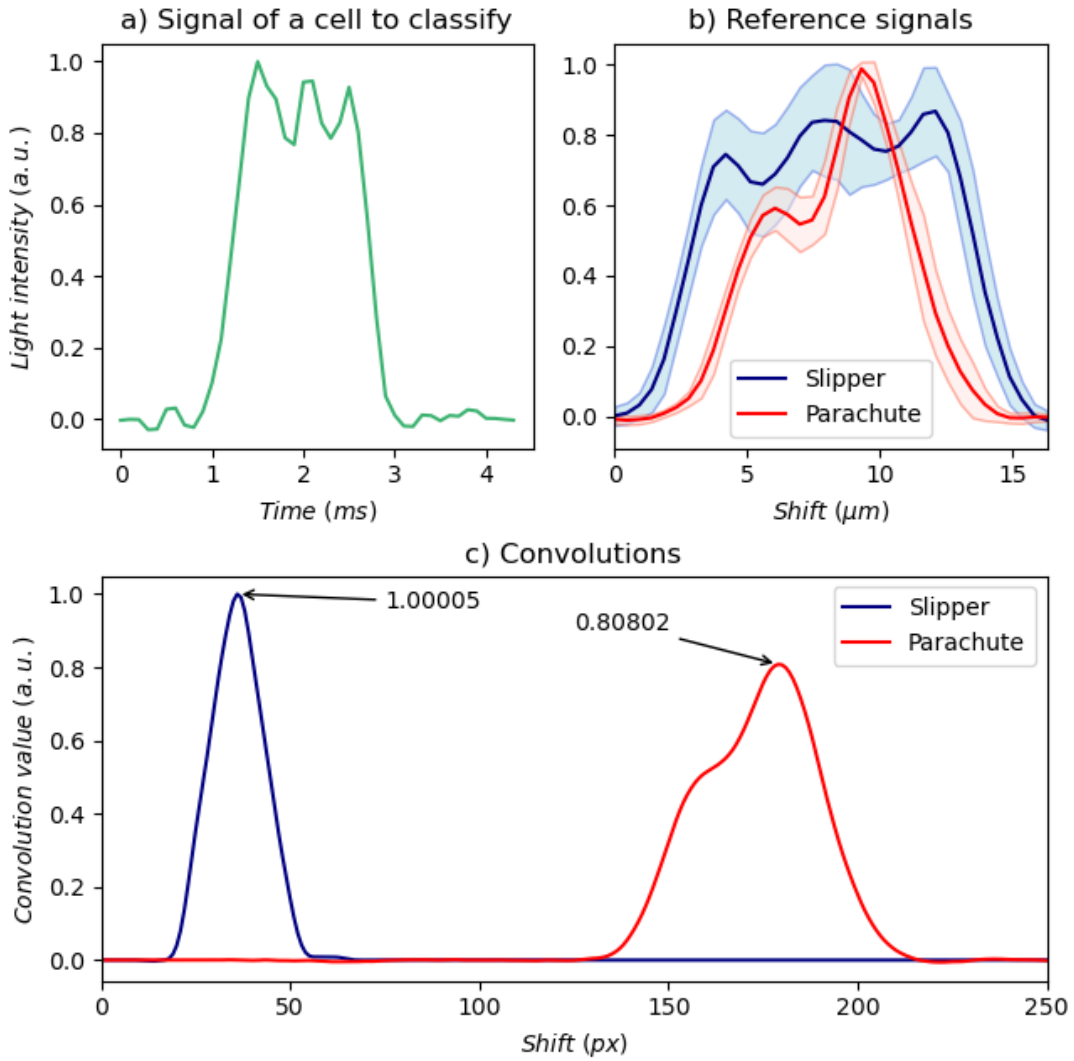

Figure 3.5: Classification of a cell signal by comparison with reference signals using convolution. a) The signal is computed from a cell picture, using the 3-pixel width slit mask, in darkfield. b) Reference signals from RBC crossing the single slit mask, in darkfield, obtained from the mean of 10 pictures of parachute RBCs (red) and 10 pictures of slipper RBCs (blue) all in the same focal plane. The semi-transparent envelopes represent the respective standard deviation. c) The convolution between the signal of the sample cell and each reference is computed. The convolution with the parachute reference signal (red) has been shifted on the x-axis for readability. The maximum of each convolution is the fitting score in the respective category (slipper or parachute), corresponding to equation 3.3. The cell is classified in the category with the highest score.

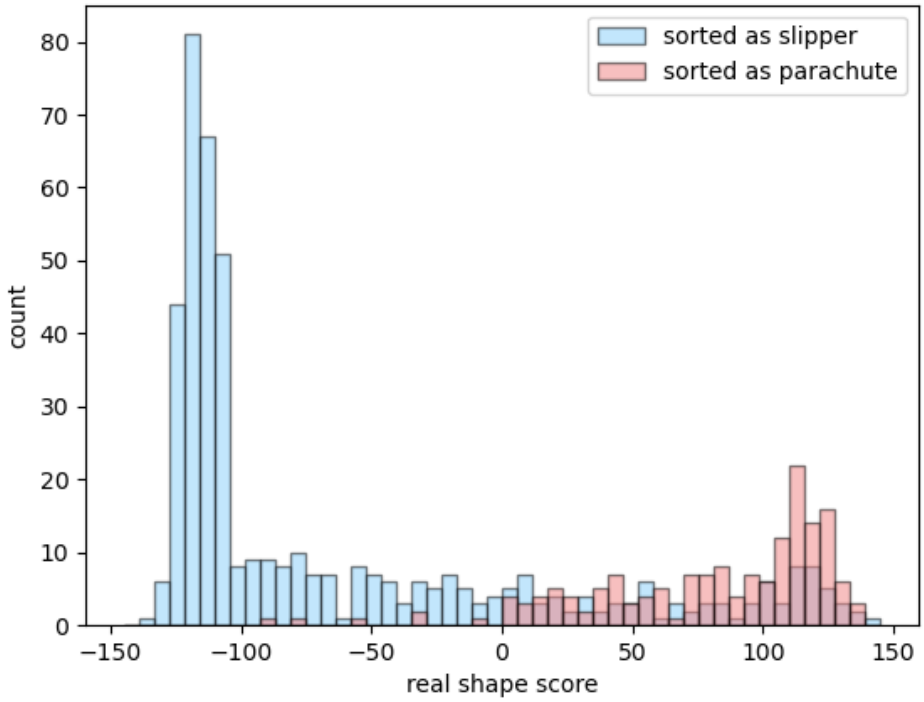

Figure 3.6: Histogram of the RBCs classified as slipper (blue) and as parachute (red) depending on the shape score given by the CNN of Kihm, Kaestner, Wagner, *et al.* [88]

for both equilibrium shapes of RBCs, by taking the mean of 10 signals from parachute RBCs and the mean of 10 signals from slipper RBCs, manually picked for their characteristic and representative shape. These reference fingerprints are compared by convolution to the signal of the RBC whose shape is to be determined. The formula for the convolution is the following :

$$S * R(x) = \sum_{j=max(1,x+1-n)}^{min(x,m)} S(j) \times R(x-j+1) \tag{3.2}$$

where $S(x)$ is the signal from the sample RBC, $R(x)$ is the reference fingerprint for parachute or slipper respectively, m is the length of S, n the length of R. The final fitting values kept to compare the cell to a parachute and to a slipper are the maximum of the convolution with the reference of a parachute and slipper respectively, normalized using the auto-convolution of each signal :

$$fitting\ score = \frac{max(S * R(x))}{\sqrt{max(S * S(x)) \times max(R * R(x))}} \tag{3.3}$$

The cell is sorted in the shape group for which it has the highest fitting value. The sorting was made on 619 pictures of cells. As we can notice on Figure 3.6, this method can accurately sort 100 % of the "perfectly" shaped slippers, meaning slippers with a score under -116.6 in Kihm, Kaestner, Wagner, *et al.* [88] and 69 % of the "perfectly" shaped parachutes, with a score above 116.6. The rate of correctly sorted cells drops as soon as the non-perfectly shaped cells are considered, the method failing to sort the cells in the group they are the closest to, even when the human eye can clearly identify them. While the use of a reference signal and convolution could be done for intermediate shapes as well, by creating multiple categories based on score intervals, the accuracy of the method would only decrease when the number of groups increases.

3.3.3 Signals classification by ANN

To sort the cells according to their shapes more precisely, we built an artificial neural network (ANN) inspired by the one used in Kihm, Kaestner, Wagner, *et al.* [88], where they give a shape score to the RBCs based on their pictures. Instead, our new classifier ANN is based on the fingerprints of the RBCs, following a sequential architecture. The classifier is composed of an input dense layer having the size of the fingerprints, *i.e.* $length_{picture} + length_{mask} - 1 = 90 + 256 - 1 = 345$, with *ReLU* activation removing negative values, and an output dense layer of size 1 giving the shape score. More explanations about this kind of architecture are detailed in paragraph 3.4.1, which describes a more complex architecture used for our image reconstruction.

The classifier has been trained according to the following procedure. The training data set is generated from the reference signals determined previously for two purposes : to enrich the number of signals and to avoid possible outliers. A number D of signals of each category is randomly generated

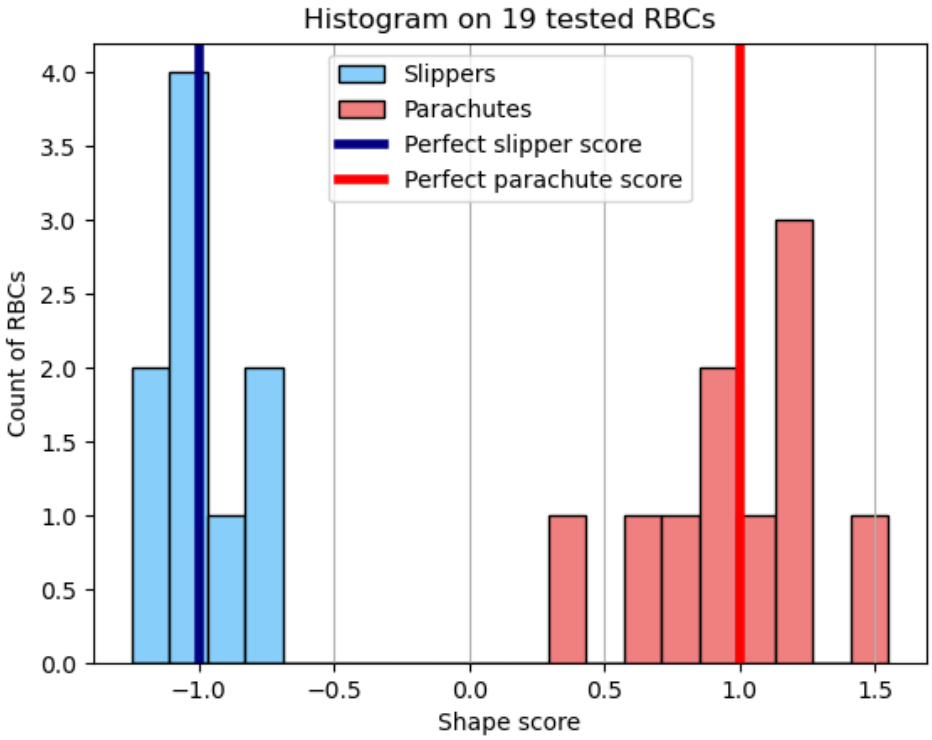

Figure 3.7: Histogram of the shape scores given by the classifier ANN to 9 real slippers (light blue) and 10 real parachutes (light red). The blue and red lines indicate the positions for the perfect slipper shapes (-1) and parachutes (+1). The classifier was trained for $D = 20$, using darkfield pictures and the 3-pixel slit mask.

following a Gaussian distribution around the reference, with a variance equal to the standard deviation of the reference. Each curve thus generated is approximated by a 13^{th} degree polynomial. Then, the data set of each category is augmented by making linear combinations between two of the D polynomials. At this point, a group of curves corresponding to "perfect" slippers (whose shape score is +1) and a group corresponding to "perfect" parachutes (whose shape score is -1) have been generated. In order to include intermediate shapes of RBCs, we made the rough assumption that an intermediate shape between a slipper and a parachute will lead to an intermediate signal between the signals of slippers and the signals of parachutes. This hypothesis allow us to virtually cover a continuum range of shapes and scores instead of a finite number of shapes. We thus generate a panel of signals, coupled with their respective shape score, covering the entire range of shape scores between -1 and 1 by making linear combinations between a slipper signal and a parachute signal. Those associations of signal and score are fed to the ANN for the training. The validation step uses a different set of signal-score pairs, generated using the same process.

Figure 3.7 presents the test of a classifier trained with darkfield signals, obtained with the 3-pixel slit mask. The training signals were generated from those presented in Figure 3.5 (b), creating randomly $D = 20$ training signals for the parachutes and the same number for the slippers. The classifier was tested on a small sample of clearly identifiable parachute (N=10) and slipper (N=9) RBCs. As it was the case with classification by convolution, the processing can sort efficiently the slippers from the parachutes.

However, once again the precision is lacking to include intermediate shapes. The best assumption is that the process to make the fingerprints loses too much data from the pictures. To improve the results, we focused on making more complex designs of the mask, to enrich the signals, and on using AI not to sort the cells but to regain more data from the fingerprints.

3.4 Mask optimization for image reconstruction

The slit mask used previously was picked arbitrary from a primary study of the reference signals. In order to pick the most efficient mask design, it is necessary to make an extensive study of different mask designs. In addition, we also aim at evaluating the possibility to reconstruct RBC images from a mask signal. To assess the efficiency of each pattern, distinct ANNs for image reconstruction have been trained and additionally evaluated regarding the respective learning performance and image quality after reconstruction.

3.4.1 Architecture of the multilayer perceptron neural network

As ANN, we employ a multilayer perceptron neural network which is realized with Keras (TensorFlow back end). The ANN is composed of an input

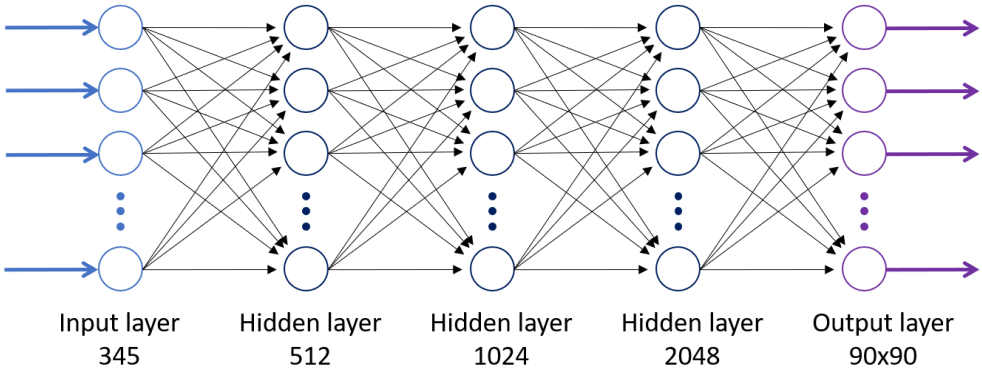

Figure 3.8: ANN architecture

layer of size 345 (length of $S(\Delta x)$ for each cell), three hidden layers which consist of 512, 1024, and 2048 neurons and an output layer of size 8100 which corresponds to the number of pixels on each reconstructed image (90 px $\times$ 90 px) (Figure 3.8).

The three inner layers are each composed of three sublayers : (1) A fully connected dense layer with transfer function $f(X) = W.X + B$, where W denotes the corresponding weights matrix, X the input vector and B the bias of each neuron, (2) a *LeakyReLU* layer [93] with a transfer function corresponding to $f(x_i) = 0.2 \times x_i$ if $x_i < 0$ and $f(x_i) = x_i$ otherwise, where x_i represent the components of X, and (3) a batch normalization layer [94].

3.4.2 Results depending on the mask pattern

Training and validation losses

For training, we use "Adam" [95] as an optimizer. As a loss function, the mean squared error (MSE) is employed which is calculated according to :

$$MSE = \frac{1}{L_p \times W_p \times P} \sum_{k=1}^{P} \sum_{j=0}^{W_p-1} \sum_{i=0}^{L_p-1} (Y_k(i,j) - \hat{Y}_k(i,j))^2 \tag{3.4}$$

where L_p and W_p correspond to the length and the width of the output image. P denotes the total number of training and validation pictures, $Y_k(i,j)$ is the intensity of pixel (i,j) of the k^{th} input image. Similarly, $\hat{Y}_k$ denotes the k^{th} predicted image.

In total, 1853 randomly selected images are used for training, and 618 are selected for validation. Table 3.1 shows the MSE of the training and validation loss for the 1000^{th} iteration and a batch size of 100 of the respective masks. Indicatively, the time required for the training for one mask is one hour on a 2.40 GHz single-core CPU.

Mask's name	Training loss	Validation loss
Blank	3.09×10^{-3}	9.82×10^{-3}
3-pixel width slit	1.64×10^{-3}	12.7×10^{-3}
Growing stripes	1.99×10^{-3}	9.66×10^{-3}
Tilted stripes	1.17×10^{-3}	5.09×10^{-3}
Growing tilted stripes	1.23×10^{-3}	5.89×10^{-3}
Barrel organ	0.893×10^{-3}	3.45×10^{-3}

Table 3.1: Comparison of the ANN training progress of certain mask types. It is apparent that modulation schemes with x- and y-components (lower three) perform better as they present lower training and validation losses than such with x-modulation only (upper three). From the tested masks, the barrel organ mask shows the best training performance.

Quality assessed using image classification

The different masks were designed considering the quality of image reconstruction and the validation loss. Among various modulation patterns, which were tested in the first place (*e.g.* slit, chessboard pattern, disc), the slit type was the most promising. To increase the complexity of the modulation scheme, over time, more and more slits have been added and their width and spacings have been varied. Besides better exploitation of the field of view, masks with a larger spatial extent and certain complexity resulted in better image reconstruction and lower validation loss (*e.g.* growing stripes as in Figure 3.4 (c)). However, masks that are invariant in the vertical (y) direction only modulate the light intensity in the x-direction (horizontal information), which results in poor image reconstruction, especially for asymmetric cells as by construction vertical information is flattened.

A demonstration of this is found in Figure 3.9 where the top row shows a representative selection of different original images, the middle row the reconstructions from a 3-pixel wide simulated slit mask (feature size of approximately 0.4 μm), and the bottom row the reconstructions from the barrel organ mask (which is not symmetric with respect to the x-axis). If the ANN reconstructs the image of a waveform obtained from a slipper by means of an x-symmetric mask, the output image is a superposition of both, bottom and top located slippers (Figure 3.9 (left, middle line)). In agreement with intuition, the signal from a vertically symmetric mask cannot see vertical asymmetries and will lead to vertically symmetric reconstructions, even if they are irrealistic. To ensure that the mask exhibits modulation in both x- and y-directions (vertical information), we rotated the openings (*e.g.* tilted stripes) or used vertical slits of different lengths or positions (*e.g.* barrel organ). Resulting modulation signals obtained from these mask types encode more information on the cell geometry in two dimensions, and the reconstructed images show lower distortions and fewer ambiguities.

As a consequence, the barrel organ mask shows the lowest training and validation losses and therefore promises the best reconstruction properties among

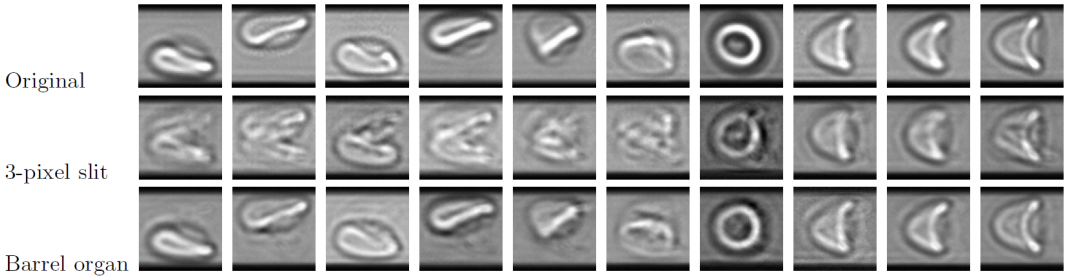

Figure 3.9: Original (top) and reconstructed images (middle, bottom) of red blood cells moving through a 11.9 $\mu m \times 9.7\ \mu m$ micro-channel. Using a simple 3-pixel wide slit mask (middle), the reconstruction results in image ambiguities, especially for cells that are located asymmetrically with respect to the horizontal axis off-axis. Due to the spatial modulation in x- and y-direction, cell fingerprints obtained from the barrel organ mask contain more spatial information (x- and y-direction) of the cell shape and reconstructed images show clearly higher prominence. This is in accordance with the better training convergence shown in Table 3.1. For both shown cases, the ANN is trained for a total of N=1000 iterations and a batch size of 100. All original pictures are taken from the supplementary material of Kihm, Kaestner, Wagner, *et al.* [88].

all tested candidates. This assumption is confirmed by the reconstructed images (Figure 3.9) which shows the lowest distortions and the best agreement with the original images.

In a further evaluation step, we benchmarked the reconstructed images of the barrel organ mask (best-performing mask) using the toolbox written by Kihm, Kaestner, Wagner, *et al.* [88]. This toolbox allows for the automatic classification of RBCs in flow to obtain a so-called "phase diagram", which shows the distribution of cell shapes within a dataset. The tool is based on a pre-trained convolutional neural network (CNN), assigning a shape-depending score to each observed RBC. In this context, a numerical value of -127 is the target score for a slipper, and +127 is the target score for a parachute. An intermediate score corresponds to a transition shape in between these stable configurations.

Figure 3.10 (a) shows the comparison of 3090 original and reconstructed images from our approach, which have undergone classification by the CNN-based toolbox. On the x-axis, the evaluation values of the original images are shown, and the y-axis shows the corresponding scores for the reconstructed images. A perfect reconstruction would lead to exactly the same score (pink line) and, therefore, to the same statistical distribution (Figure 3.10 (d)). However, the coefficient of determination between the distribution scores R^2 = 0.76, i.e., the fraction of variance unexplained (FVU), corresponds to 24 %. In contrast, 76 % of cells are approximated correctly after reconstruction. By applying the same thresholds as in the work of Kihm, Kaestner, Wagner, *et al.* [88], 52 % of the cells originally classified as parachutes and 54 % of cells originally classified as slippers remain in the same class after reconstruction. Figures 3.10 (b) and 3.10 (c) illustrate an example of a cell that is wrongly

classified. Here, the ANN added internal patterns to the cell image during reconstruction. As the CNN relies on local convolutions within the image, the variations created by artifacts highly affect the assigned score and, thus, the accuracy of the classification. It can be expected that more sophisticated reconstruction methods, e.g., using generative adversarial networks (GANs), could lead to better results since image reconstructions are closer to the corresponding real images.

3.5 Conclusion

In summary, we investigated and simulated an advanced, label-free imaging method without the need for sophisticated optics. We reconstructed images from RBCs in microfluidic flow using simple cell fingerprints originating from intensity modulated signals which are generated by using a binary slit mask. The method employs an artificial neural network for image reconstruction from simple waveforms, which could be recorded by a fast photodiode. The upper limit of the framerate is restricted by the velocity of the cells and the bandwidth of the photodiode. Considering a spacing of 33.8 µm between two cells, which is equal to the length of the mask, the device can reach a throughput of 29 586 cells/s for a cell velocity of 1 m/s and 295 858 cells/s for 10 m/s. The spacing of 33.8 µm is to ensure that only one cell crosses the ROI at a time. However, this distance might be reduced if certain mask patterns exist, which can handle multiple cells in the field of view. Nevertheless, those patterns must first be identified and tested. The sample rate is given by the minimal feature size of the mask. If the cell velocity corresponds to 1 m/s and the minimal feature size is 0.4 µm, the time-of-flight corresponds to 0.4 µs. Typically, a minimal oversampling rate of 10X is chosen, resulting in an ADC sample rate of 25 MSPS. If the bandwidth of the photodiode is chosen two times higher than the sample rate of the ADC, a 50 MHz photodiode might be sufficient to detect cells at 1 m/s. For 10 m/s, the ADC frequency corresponds to 250 MSPS, the bandwidth of the photodiode to 500 MHz. It is demonstrated that the particular mask pattern is crucial for the quality of the reconstruction and we found that binary masks with 2D modulation schemes are mandatory to obtain reasonable results. Image reconstruction through light amplitude modulation and machine learning is largely studied in the very recent years. For instance Ota, Horisaki, Kawamura, *et al.* [96] uses an analytical recovery method to reconstruct a low resolution fluorescence image from a one-pixel sensor. Another example is Chen, Su, Liu, *et al.* [85] who uses a camera but highly simplifies the optical setup removing the lenses. In Jiang, Li, Peng, *et al.* [97], a method for image reconstruction of blurry images is proposed, which uses using ANN-based de-noising techniques macroscopic moving objects using a lens and a digital mirror device (containing digital mask pattern). However, in practice, each approach is highly case-dependent. Thus, investigating various methods and applications remains essential to develop a general technique. While we use a CNN for image reconstruction, the field of AI image building is in active

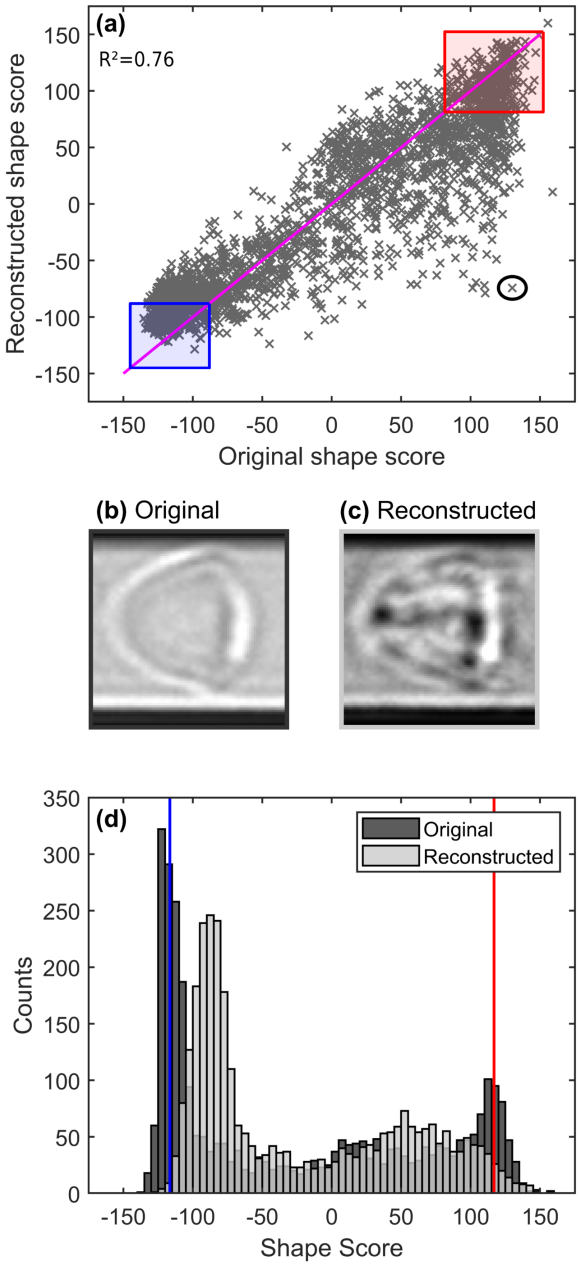

Figure 3.10: a) The scatter plot shows the shape-score given by the CNN for the original cell images (x-axis) and the corresponding reconstructions (y-axis) using the barrel organ mask for modulation. In the case of perfect reconstruction, the data points would be located on the pink line. The blue and red boxes indicate the target area for slippers (-127) and parachutes (+127), and their size is defined by an optimal threshold range ("adapted threshold range"). The marked outlier in (a) is shown in (b) and (c), where (b) is the original image and (c) the poor reconstruction that exhibits many artifacts leading to a wrong shape score. d) shows two histograms of the shape scores given to the original dataset (dark gray) and the reconstructed dataset (light gray). The blue and red lines indicate the positions for the perfect slipper shapes (-127) and parachutes (+127). The information loss due to modulation and the resulting disturbances from reconstruction leads to a less defined, smoothed shape spectrum and causes the distribution maxima to shift closer together. Therefore, dealing with reconstructed data, the threshold ranges must be adapted to take the distortions and different distribution properties into account. The original shape scores and optimal threshold ranges in (a) and the picture (b) are all taken from the article "Classification of red blood cell shapes in flow using outlier tolerant machine learning" by Kihm, Kaestner, Wagner, *et al.* [88].

evolution. A more sophisticated architecture, like using generative adversarial networks, could avoid the typical artifacts from a CNN and lead to better results.

Our approach combines the use of a binary slit mask for the spatial modulation of cell brightfield images of cells in microcapillary flow, and machine learning to recover the cell images from moving cells at high velocities at microscale, without the need for a complex optical set-up. We tested the method using RBCs as model cells which exhibit two stable shape types depending on the flow regime. However, more cell types or even clusters of RBCs could be easily added by providing relevant training data to the network. The technique could further be implemented as part of a lab-on-chip device which is not larger than a matchbox and more complex suspensions such as whole blood could be investigated. Notably, we started to investigate the detection of circulating tumor cells, by differentiating them from white blood cells thanks to their deformation through an hyperbolic nozzle.

A step further into automation, in order for our ANN to adapt more flexibly to the training data mentioned above, could be to integrate the generation step of the mask pattern in the machine learning process. By iteration the mask would converge toward an optimal pattern, suited to training data.

Although cells need no labeling, the system could be trained towards the evaluation of fluorescence signals and the approach could be used for *in-vivo* applications where optical imaging is difficult. Moreover, being able to reconstruct the cell images means that the fingerprints contain all major shape information of the cells. As many applications require cell shape information but not the image itself, the use of fingerprints would be a more efficient and direct way to extract the desired cell parameters [96]. This sets the scene for sophisticated diagnostic applications.

Outroduction

In conclusion, this comprehensive research has delved into two different aspects in the field of blood flow dynamics and analysis of RBCs. The first part of the study explored the impact of aggregation on the distribution of RBCs at microbifurcations. By employing experimental techniques and a multi-physics approach, we examined the behavior of RBCs in flow and its correlation with Dextran-induced aggregation. Our findings revealed that aggregation significantly influenced the distribution of RBCs in microbifurcations, leading to increased non-linearity and heterogeneity in the distribution patterns. The Zweifach-Fung effect demonstrated distinct variation with different concentrations of Dextran 70kDa. This study should be of significant interest for the modeling and understanding of blood dynamics in the microcirculation and its alterations in inflammatory or pathological conditions, as the RBC distribution at bifurcations together with blood effective viscosity in confined channels are the key ingredients of network dynamics.

In the second part of this research, we focused on high-throughput automated image processing of RBCs using optical modulation and artificial neural networks. Our novel technique employed a mask to encode visual information of RBCs passing through the detection zone, facilitating the reconstruction of images without the need for high-speed cameras or elaborate optical setups. By combining optical spatial amplitude modulation and AI, we virtually accomplished image reconstruction and successfully achieved shape recognition of single RBCs with simplicity and efficiency.

Through a multidisciplinary approach integrating biology, fluid mechanics, solid mechanics, and computer science, this work yields insights into the behavior and distribution of RBCs under various conditions. It paves the way for a deeper fundamental understanding of blood flow dynamics in microcirculatory networks and its relevance in clinical contexts. The ability to quantify the effect of aggregation on RBC distribution opens new avenues for studying various physiological and pathological conditions.

Moving forward, this research lays the foundation for future investigations into the impact of geometric parameters, such as channel shapes and bifurcation angles, on RBC distribution and behavior, or the effect of the inlet Ht. While we focused on an elementary unit, one bifurcation, the final aim would be to understand the blood flow in the whole microcirculatory network, conducting such study on a complex succession of bifurcations and junctions closer to physiology.

Furthermore, the proposed AI-based image processing method showcases potential for broader applications in various medical and scientific domains. Characteristics must be considered to build the device that implements our technique, such as the bandwidth and frequency of the diode or the resolution of fabrication of the mask pattern. The conceived ANN can easily be adapted, with the correct training data, to consider cells other than RBCs, or even to analyze clusters of RBCs and thus study aggregation in microflows. As a proof-of-concept study, this work serves as a stepping stone for further advancements and innovations in the study of blood rheology in microcirculation and the analysis of RBC characteristics.

Bibliography

[1] E. T. Gowell, *Amazing Jellies: Jewels of the Sea*. Bunker Hill Publishing, Inc., 2004.

[2] D. Barber, J. Mills Westermann, and M. White, "The blood cells of the antarctic icefish chaenocephalus aceratus lönnberg: Light and electron microscopic observations," *Journal of Fish Biology*, vol. 19, no. 1, pp. 11–28, 1981.

[3] I Virtanen, M Kurkinen, and V.-P. Lehto, "Nucleus-anchoring cytoskeleton in chicken red blood cells," *Cell biology international reports*, vol. 3, no. 2, pp. 157–162, 1979.

[4] K. N. Yap and Y. Zhang, "Revisiting the question of nucleated versus enucleated erythrocytes in birds and mammals," *American Journal of Physiology-Regulatory, Integrative and Comparative Physiology*, vol. 321, no. 4, R547–R557, 2021, PMID: 34378417. doi: 10.1152/ajpregu.00276.2020. eprint: https://doi.org/10.1152/ajpregu.00276.2020. [Online]. Available: https://doi.org/10.1152/ajpregu.00276.2020.

[5] J.-M. Poiseuille, "Recherches sur les causes du mouvement du sang dans les vaisseaux capillaires," *Comptes rendus hebdomadaires des séances de l'Académie des sciences*, vol. 1, pp. 554–560, 1835.

[6] M. H. Lee, C. J. Gisnarian, and K. G. Shann, "Improved estimation of total blood volume can provide a reliable prediction of dilutional hematocrit and oxygen delivery during cardiopulmonary bypass," *The journal of extra-corporeal technology*, vol. 51, no. 2, pp. 67–72, 2019. [Online]. Available: https://www.ncbi.nlm.nih.gov/pmc/articles/PMC6586263/.

[7] J. Feher, "5.10 - the microcirculation and solute exchange," in *Quantitative Human Physiology*, J. Feher, Ed., Boston: Academic Press, 2012, pp. 508–518, isbn: 978-0-12-382163-8. doi: https://doi.org/10.1016/B978-0-12-382163-8.00055-4. [Online]. Available: https://www.sciencedirect.com/science/article/pii/B9780123821638000554.

[8] J. Busher, "Serum albumin and globulin," in *Clinical Methods: The History, Physical, and Laboratory Examinations. 3rd edition*, H. Walker, W. Hall, and J. Hurst, Eds. Boston: Butterworths, 1990, ch. 101. [Online]. Available: https://www.ncbi.nlm.nih.gov/books/NBK204/.

[9] "5 human albumin," in *Transfusion medicine and hemotherapy : offizielles Organ der Deutschen Gesellschaft fur Transfusionsmedizin und Immunhamatologie*, 6, Kager, Ed., vol. 36, 2009, pp. 399–407. [Online]. Available: https://www.ncbi.nlm.nih.gov/pmc/articles/PMC2997295/.

[10] T. E. of Encyclopaedia Britannica, *Globulin*, in *Encyclopedia Britannica*, Britannica. [Online]. Available: https://www.britannica.com/science/globulin (visited on 2022).

[11] R. Asselta, S. Duga, and M. L. Tenchini, "The molecular basis of quantitative fibrinogen disorders," *Journal of Thrombosis and Haemostasis*, vol. 4, no. 10, pp. 2115–2129, 2006. doi: https://doi.org/10.1111/j.1538-7836.2006.02094.x. eprint: https://onlinelibrary.wiley.com/doi/pdf/10.1111/j.1538-7836.2006.02094.x. [Online]. Available: https://onlinelibrary.wiley.com/doi/abs/10.1111/j.1538-7836.2006.02094.x.

[12] M. Roshal, "Chapter 123 - thrombin time and fibrinogen determination," in *Transfusion Medicine and Hemostasis (Second Edition)*, B. Shaz, C. Hillyer, M. Roshal, and C. Abrams, Eds., Second Edition, San Diego: Elsevier, 2013, pp. 793–798, isbn: 978-0-12-397164-7. doi: https://doi.org/10.1016/B978-0-12-397164-7.00123-3. [Online]. Available: https://www.sciencedirect.com/science/article/pii/B9780123971647001233.

[13] M. Brust, O. Aouane, M. Thiébaud, *et al.*, "The plasma protein fibrinogen stabilizes clusters of red blood cells in microcapillary flows," *Sci. Rep.*, vol. 4, p. 4348, 2014.

[14] M. Brust, C. Schaefer, R. Doerr, L. Pan, M. Garcia, P. E. Arratia, and C. Wagner, "Rheology of human blood plasma: Viscoelastic versus newtonian behavior," *Phys. Rev. Lett.*, vol. 110, p. 078 305, 7 2013.

[15] S. Varchanis, Y. Dimakopoulos, C. Wagner, and J. Tsamopoulos, "How viscoelastic is human blood plasma?" *Soft Matter*, vol. 14, pp. 4238–4251, 21 2018. doi: 10.1039/C8SM00061A. [Online]. Available: http://dx.doi.org/10.1039/C8SM00061A.

[16] D. N. Ku, "Blood flow in arteries," *Annual Review of Fluid Mechanics*, vol. 29, no. 1, pp. 399–434, 1997. doi: 10.1146/annurev.fluid.29.1.399. eprint: https://doi.org/10.1146/annurev.fluid.29.1.399. [Online]. Available: https://doi.org/10.1146/annurev.fluid.29.1.399.

[17] S. Chien, "Shear dependence of effective cell volume as a determinant of blood viscosity," *Science*, vol. 168, pp. 977–979, 1970.

[18] M. Tomaiuolo, R. I. Litvinov, J. W. Weisel, and T. J. Stalker, "Use of electron microscopy to study platelets and thrombi," *Platelets*, vol. 31, no. 5, pp. 580–588, 2020, PMID: 32423268. doi: 10.1080/09537104.2020.1763939. eprint: https://doi.org/10.1080/09537104.2020.1763939. [Online]. Available: https://doi.org/10.1080/09537104.2020.1763939.

[19] P. Steffen, C. Verdier, and C. Wagner, "Quantification of depletion-induced adhesion of red blood cells," *Physical Review Letters*, vol. 110, no. 1, Jan. 2013. doi: 10.1103/physrevlett.110.018102. [Online]. Available: https://doi.org/10.1103\%2Fphysrevlett.110.018102.

[20] D. Flormann, "Physical characterization of red blood cells aggregation," PhD thesis, Université Grenoble Alpes; Universität des Saarlandes, Mar. 2017. [Online]. Available: https://www.theses.fr/2017GREAY002.

[21] K.-M. Jan and S. Chien, "Role of Surface Electric Charge in Red Blood Cell Interactions," *Journal of General Physiology*, vol. 61, no. 5, pp. 638–654, May 1973, issn: 0022-1295. doi: 10.1085/jgp.61.5.638. eprint:

https://rupress.org/jgp/article-pdf/61/5/638/1809832/638.pdf. [Online]. Available: https://doi.org/10.1085/jgp.61.5.638.

[22] D. Lominadze and W. L. Dean, "Involvement of fibrinogen specific binding in erythrocyte aggregation," *FEBS letters*, vol. 517, no. 1-3, pp. 41–44, Apr. 2002, issn: 0014-5793. doi: 10.1016/s0014-5793(02)02575-9. [Online]. Available: https://europepmc.org/articles/PMC2819362.

[23] P. Bagchi, P. C. Johnson, and A. S. Popel, "Computational Fluid Dynamic Simulation of Aggregation of Deformable Cells in a Shear Flow," *Journal of Biomechanical Engineering*, pp. 1070–1080, Aug. 2005, issn: 0148-0731. doi: 10.1115/1.2112907. eprint: https://asmedigitalcollection.asme.org/biomechanical/article-pdf/doi/10.1115/1.2112907/6909349/1070_1.pdf. [Online]. Available: https://doi.org/10.1115/1.2112907.

[24] S. Asakura and F. Oosawa, "Interaction between particles suspended in solutions of macromolecules," *Journal of Polymer Science*, vol. 33, no. 126, pp. 183–192, 1958. doi: https://doi.org/10.1002/pol.1958.1203312618. eprint: https://onlinelibrary.wiley.com/doi/pdf/10.1002/pol.1958.1203312618. [Online]. Available: https://onlinelibrary.wiley.com/doi/abs/10.1002/pol.1958.1203312618.

[25] Z. Dogic, K. R. Purdy, E. Grelet, M. Adams, and S. Fraden, "Isotropic-nematic phase transition in suspensions of filamentous virus and the neutral polymer dextran," *Physical Review E*, vol. 69, no. 5, May 2004. doi: 10.1103/physreve.69.051702. [Online]. Available: https://doi.org/10.1103%2Fphysreve.69.051702.

[26] B. Vincent, J. Edwards, S. Emmett, and A. Jones, "Depletion flocculation in dispersions of sterically-stabilised particles ("soft spheres")," *Colloids and Surfaces*, vol. 18, no. 2, pp. 261–281, 1986, issn: 0166-6622. doi: https://doi.org/10.1016/0166-6622(86)80317-1. [Online]. Available: https://www.sciencedirect.com/science/article/pii/0166662286803171.

[27] K. Buxbaum, E. Evans, and D. E. Brooks, "Quantitation of surface affinities of red blood cells in dextran solutions and plasma," *Biochemistry*, vol. 21, no. 13, pp. 3235–3239, 1982, PMID: 6179539. doi: 10.1021/bi00256a032. eprint: https://doi.org/10.1021/bi00256a032. [Online]. Available: https://doi.org/10.1021/bi00256a032.

[28] B. Neu and H. Meiselman, "Depletion-mediated red blood cell aggregation in polymer solutions," *Biophysical Journal*, vol. 83, no. 5, pp. 2482–2490, 2002, issn: 0006-3495. doi: https://doi.org/10.1016/S0006-3495(02)75259-4. [Online]. Available: https://www.sciencedirect.com/science/article/pii/S0006349502752594.

[29] T. Podgorski, "Hemodynamics and hemorheology," in *Biological Flow in Large Vessels*. John Wiley & Sons, Ltd, 2022, ch. 1, pp. 1–41, isbn: 9781119986607. doi: https://doi.org/10.1002/9781119986607.ch1. eprint: https://onlinelibrary.wiley.com/doi/pdf/10.1002/9781119986607.ch1. [Online]. Available: https://onlinelibrary.wiley.com/doi/abs/10.1002/9781119986607.ch1.

[30] G. Lim H. W., M. Wortis, and R. Mukhopadhyay, "Red blood cell shapes and shape transformations: Newtonian mechanics of a composite membrane: Sections 2.5–2.8," in *Soft Matter*. John Wiley & Sons, Ltd, 2008, ch. 2, pp. 139–204, isbn: 9783527623372. doi: https://doi.org/10.1002/9783527623372.ch2b. eprint: https://onlinelibrary.wiley.com/doi/pdf/10.1002/9783527623372.ch2b. [Online]. Available: https://onlinelibrary.wiley.com/doi/abs/10.1002/9783527623372.ch2b.

[31] R. Chachanidze, "Collective phenomena in blood suspensions," Theses, Université Grenoble Alpes [2020-....] ; Universität des Saarlandes, 2018. [Online]. Available: https://www.theses.fr/2018AIXM0632.

[32] S. P. Sutera and R. Skalak, "The history of Poiseuille's law," *Annu. Rev. Fluid Mech.*, vol. 25, pp. 1–20, 1993.

[33] R. Fåhræus, "The suspension stability of the blood," *Physiological Reviews*, vol. IX, pp. 241–274, 1929.

[34] A. R. Pries, T. W. Secomb, P. Gaehtgens, and J. F. Gross, "Blood flow in microvascular networks. experiments and simulation.," *Circ. Res.*, vol. 67, no. 4, pp. 826–34, 1990. doi: 10.1161/01.RES.67.4.826.

[35] R. Fåhræus and T. Lindqvist, "The viscosity of the blood in narrow capillary tubes," *American Journal of Physiology-Legacy Content*, vol. 96, no. 3, pp. 562–568, 1931. doi: 10.1152/ajplegacy.1931.96.3.562. eprint: https://doi.org/10.1152/ajplegacy.1931.96.3.562. [Online]. Available: https://doi.org/10.1152/ajplegacy.1931.96.3.562.

[36] A. Pries, N. Neuhaus, and P. Gaehtgens, "Blood viscosity in tube flow: Dependence on diameter and hematocrit," *Am. J. Physiol.*, vol. 20, H1770–H1778, 1992.

[37] D. Fedosov, M. Peltomäki, and G. Gompper, "Deformation and dynamics of red blood cells in flow through cylindrical microchannels," *Soft Matter*, vol. 10, pp. 4258–4267, 24 2014. doi: 10.1039/C4SM00248B. [Online]. Available: http://dx.doi.org/10.1039/C4SM00248B.

[38] S. M. Recktenwald, K. Graessel, F. M. Maurer, T. John, S. Gekle, and C. Wagner, "Red blood cell shape transitions and dynamics in time-dependent capillary flows," *Biophysical Journal*, vol. 121, no. 1, pp. 23–36, 2022, issn: 0006-3495. doi: https://doi.org/10.1016/j.bpj.2021.12.009. [Online]. Available: https://www.sciencedirect.com/science/article/pii/S000634952103900X.

[39] A. Guckenberger, A. Kihm, T. John, C. Wagner, and S. Gekle, "Numerical–experimental observation of shape bistability of red blood cells flowing in a microchannel," en, *Soft Matter*, vol. 14, no. 11, pp. 2032–2043, Mar. 2018, issn: 1744-6848. doi: 10.1039/C7SM02272G. [Online]. Available: https://pubs.rsc.org/en/content/articlelanding/2018/sm/c7sm02272g.

[40] O. Linderkamp, E. Friederichs, T. Boehler, and A. Ludwig, "Age dependency of red blood cell deformability and density: Studies in transient erythroblastopenia of childhood," *British Journal of Haematology*, vol. 83, no. 1, pp. 125–129, 1993. doi: https://doi.org/10.1111/j.1365-2141.1993.tb04642.x. eprint: https://onlinelibrary.wiley.com/

doi/pdf/10.1111/j.1365-2141.1993.tb04642.x. [Online]. Available: https://onlinelibrary.wiley.com/doi/abs/10.1111/j.1365-2141.1993.tb04642.x.

[41] K. Svanes and B. W. Zweifach, "Variations in small blood vessel hematocrits produced in hypothermic rats by micro-occlusion," *Microvasc. Res.*, vol. 1, pp. 210–220, 1968.

[42] Y. C. Fung, "Stochastic flow in capillary blood vessels," *Microvasc. Res.*, vol. 5, pp. 34–48, 1973.

[43] A. R. Pries, T. W. Secomb, and P. Gaethgens, "Biophysical aspects of blood flow in the microvasculature," *Cardiovasc. Res.*, vol. 32, pp. 654–667, 1996.

[44] S. Chien, C. D. Tvetenstrand, M. A. Epstein, and G. W. Schmid-Schonbein, "Model studies on distributions of blood cells at microvascular bifurcations," *Am. J. Physiol. Heart Circ. Physiol.*, vol. 248, H568–H576, 1985.

[45] J. O. Barber, J. P. Alberding, J. M. Restrepo, and T. W. Secomb, "Simulated two-dimensional red blood cell motion, deformation, and partitioning in microvessel bifurcations," *Ann. Biomech. Eng.*, vol. 36, pp. 1690–1698, 2008.

[46] V. Doyeux, T. Podgorski, S. Peponas, M. Ismail, and G. Coupier, "Spheres in the vicinity of a bifurcation: Elucidating the Zweifach-Fung effect," *J. Fluid Mech.*, vol. 674, p. 359, 2011.

[47] Z. Shen, G. Coupier, B. Kaoui, B. Polack, J. Harting, C. Misbah, and T. Podgorski, "Inversion of hematocrit partition at microfluidic bifurcations," *Microvasc. Res.*, vol. 105, pp. 40 –46, 2016.

[48] P. Balogh and P. Bagchi, "Analysis of red blood cell partitioning at bifurcations in simulated microvascular networks," *Physics of Fluids*, vol. 30, no. 5, p. 051 902, 2018. doi: 10.1063/1.5024783. [Online]. Available: https://doi.org/10.1063/1.5024783.

[49] J. Zhang, P. C. Johnson, and A. S. Popel, "Effects of erythrocyte deformability and aggregation on the cell free layer and apparent viscosity of microscopic blood flows," *Microvascular Research*, vol. 77, no. 3, pp. 265–272, 2009, issn: 0026-2862. doi: https://doi.org/10.1016/j.mvr.2009.01.010. [Online]. Available: https://www.sciencedirect.com/science/article/pii/S0026286209000284.

[50] D. A. Fedosov, W. Pan, B. Caswell, G. Gompper, and G. E. Karniadakis, "Predicting human blood viscosity in silico," *Proc. Nat. Acad. Sci. USA*, vol. 108, pp. 11 772–11 777, 2011.

[51] F. Yaya, "Physical properties of red blood cells in aggregation," Theses, Université Grenoble Alpes [2020-....] ; Universität des Saarlandes, Jan. 2021. [Online]. Available: https://theses.hal.science/tel-03281595.

[52] C. Boucly, T. Podgorski, and G. Coupier, "Distribution d'une suspension de globules rouges á une bifurcation en présence d'adhésion intercellulaire," Internship license thesis, ENS Lyon, 2014.

[53] W. Reinhart, N. Piety, and S. Shevkoplyas, "Influence of red blood cell aggregation on perfusion of an artificial microvascular network," *Microcirculation*, vol. 24, no. 5, e12317, 2017. doi: https://doi.org/10.1111/

micc.12317. eprint: https://onlinelibrary.wiley.com/doi/pdf/10.1111/micc.12317. [Online]. Available: https://onlinelibrary.wiley.com/doi/abs/10.1111/micc.12317.

[54] E. Kaliviotis, J. M. Sherwood, and S. Balabani, "Local viscosity distribution in bifurcating microfluidic blood flows," *Physics of Fluids*, vol. 30, no. 3, p. 030706, 2018. doi: 10.1063/1.5011373. [Online]. Available: https://doi.org/10.1063/1.5011373.

[55] J. M. Sherwood, E. Kaliviotis, J. Dusting, and S. Balabani, "Hematocrit, viscosity and velocity distributions of aggregating and non-aggregating blood in bifurcating microchannel," *Biomicrofluidics*, vol. 6, 024119, pp. –, 2012.

[56] P. Tabeling, *Introduction to Microfluidics*. Oxford University Press, 2005, isbn: 0198568649.

[57] D. Flormann, O. Aouane, L. Kaestner, C. Ruloff, C. Misbah, T. Podgorski, and C. Wagner, "The buckling instability of aggregating red blood cells," en, *Scientific Reports*, vol. 7, no. 1, Dec. 2017, issn: 2045-2322. doi: 10.1038/s41598-017-07634-6. [Online]. Available: http://www.nature.com/articles/s41598-017-07634-6 (visited on 11/07/2018).

[58] A. Merlo, S. Losserand, F. Yaya, *et al.*, "Influence of storage and buffer composition on the mechanical behavior of flowing red blood cells," *Biophysical journal*, vol. 122, no. 2, pp. 360–373, 2023. doi: 10.1016/j.bpj.2022.12.005.

[59] D. F. Swinehart, "The beer-lambert law," *Journal of Chemical Education*, vol. 39, no. 7, p. 333, 1962. doi: 10.1021/ed039p333. [Online]. Available: https://doi.org/10.1021/ed039p333.

[60] P. Liu, Z. Zhu, C.-C. Zeng, and G. Nie, "Specific absorption spectra of hemoglobin at different PO2 levels: potential noninvasive method to detect PO2 in tissues," *Journal of Biomedical Optics*, vol. 17, no. 12, p. 125002, 2012. doi: 10.1117/1.JBO.17.12.125002. [Online]. Available: https://doi.org/10.1117/1.JBO.17.12.125002.

[61] S. Roman, "Écoulements de suspensions concentrées de globules rouges en micro-canaux : étude expérimentale," Theses, Institut National Polytechnique de Toulouse - INPT, Dec. 2012. [Online]. Available: https://hal.science/tel-01692579.

[62] H. Lipowsky, S. Usami, and S. Chien, "In vivo measurements of "apparent viscosity" and microvessel hematocrit in the mesentery of the cat," *Microvascular Research*, vol. 19, no. 3, pp. 297–319, 1980, issn: 0026-2862. doi: https://doi.org/10.1016/0026-2862(80)90050-3. [Online]. Available: https://www.sciencedirect.com/science/article/pii/0026286280900503.

[63] H. Wayland and P. C. Johnson, "Erythrocyte velocity measurement in microvessels by a two-slit photometric method.," *Journal of Applied Physiology*, vol. 22, no. 2, pp. 333–337, 1967, PMID: 6017904. doi: 10.1152/jappl.1967.22.2.333. eprint: https://doi.org/10.1152/jappl.1967.22.2.333. [Online]. Available: https://doi.org/10.1152/jappl.1967.22.2.333.

[64] F. White, *Viscous Fluid Flow* (McGraw-Hill series in mechanical engineering). McGraw-Hill, 1991, isbn: 9780070697126. [Online]. Available: https://books.google.fr/books?id=G6IeAQAAIAAJ.

[65] J. M. Sherwood, J. Dusting, E. Kaliviotis, and S. Balabani, "The effect of red blood cell aggregation on velocity and cell-depleted layer characteristics of blood in a bifurcating microchannel," *Biomicrofluidics*, vol. 6, 024119, pp. –, 2012.

[66] G. Cokelet and H. Meiselman, "Macro- and micro-rheological properties of blood," in *Handbook of Hemorheology and Hemodynamics*, O. Baskurt, M. Hardeman, M. Rampling, and H. Meiselman, Eds., IOS Press, Jan. 2007, pp. 45–71.

[67] S. Chien, R. King, R. Skalak, S. Usami, and A. Copley, "Viscoelastic properties of human blood and red cell suspensions," *Biorheology*, vol. 12, no. 6, pp. 341–346, 1975. doi: 10.3233/bir-1975-12603.

[68] G. Thurston, "Viscoelasticity of human blood," *Biophysical Journal*, vol. 12, no. 9, pp. 1205–1217, 1972, issn: 0006-3495. doi: https://doi.org/10.1016/S0006-3495(72)86156-3. [Online]. Available: https://www.sciencedirect.com/science/article/pii/S0006349572861563.

[69] M. Brust, O. Aouane, M. Thiebaud, *et al.*, "The plasma protein fibrinogen stabilizes clusters of red blood cells in microcapillary flows," *Scientific Reports*, vol. 4, no. 1, 2015, issn: 2045-2322. doi: https://doi.org/10.1038/srep04348.

[70] S. R. Pop, G. Richardson, S. L. Waters, and O. E. Jensen, "Shock formation and non-linear dispersion in a microvascular capillary network," en, *Mathematical Medicine and Biology*, vol. 24, no. 4, pp. 379–400, Oct. 2007, issn: 1477-8599, 1477-8602. doi: 10.1093/imammb/dqm007. [Online]. Available: https://academic.oup.com/imammb/article-lookup/doi/10.1093/imammb/dqm007 (visited on 10/03/2022).

[71] J. B. Geddes, B. D. Storey, D. Gardner, and R. T. Carr, "Bistability in a simple fluid network due to viscosity contrast," *Phys. Rev. E*, vol. 81, p. 046 316, 2010.

[72] B. J. Bain, "Diagnosis from the Blood Smear," en, *New England Journal of Medicine*, vol. 353, no. 5, pp. 498–507, Aug. 2005, issn: 0028-4793, 1533-4406. doi: 10.1056/NEJMra043442. [Online]. Available: http://www.nejm.org/doi/10.1056/NEJMra043442 (visited on 04/10/2020).

[73] T. Sun and H. Morgan, "Single-cell microfluidic impedance cytometry: A review," *Microfluidics and Nanofluidics*, vol. 8, no. 4, 2010, issn: ISSN: 1613-4982, 1613-4990. doi: https://doi.org/10.1007/s10404-010-0580-9.

[74] "Apparatus and method for measuring a dividing particle size of a particulate system," pat., 1967.

[75] D. K. Wood, S. Oh, S. H. Lee, H. T. Soh, and A. N. Cleland, "High-bandwidth radio frequency coulter counter," *Applied Physics Letters*, vol. 87, p. 184 106, 2005. [Online]. Available: https://api.semanticscholar.org/CorpusID:119622121.

[76] D. J. Stephens, "Light microscopy techniques for live cell imaging," *Science*, vol. 300, no. 5616, 2003, issn: ISSN: 00368075, 10959203. doi: https://doi.org/10.1126/science.1082160.

[77] M. Kozubek, S. Kozubek, E. Lukasova, and A. Marec, "High-resolution cytometry of fish dots in interphase cell nuclei," *Cytometry*, vol. 36, 1999. doi: https://doi.org/10.1002/(SICI)1097-0320(19990801)36:4<279::AID-CYTO2>3.0.CO;2-G.

[78] Y. Han, R. Tang, Y. Gu, A. C. Zhang, W. Cai, V. Castor, S. H. Cho, W. Alaynick, and Y.-H. Lo, "Cameraless high-throughput three-dimensional imaging flow cytometry," *Optica*, vol. 6, no. 10, 2019, issn: ISSN: 2334-2536. doi: https://doi.org/10.1364/OPTICA.6.001297.

[79] S. Stavrakis, G. Holzner, J. Choo, and A. deMello, "High-throughput microfluidic imaging flow cytometry," *Current Opinion in Biotechnology*, vol. 55, pp. 36–43, Feb. 2019, issn: 09581669. doi: 10.1016/j.copbio.2018.08.002. [Online]. Available: https://linkinghub.elsevier.com/retrieve/pii/S0958166918300363 (visited on 01/08/2021).

[80] S. C. Hur, H. T. K. Tse, and D. Di Carlo, "Sheathless inertial cell ordering for extreme throughput flow cytometry," *Lab Chip*, vol. 10, no. 3, pp. 274–280, 2010, issn: 1473-0197, 1473-0189. doi: 10.1039/B919495A. [Online]. Available: http://xlink.rsc.org/?DOI=B919495A (visited on 01/12/2021).

[81] A. S. Rane, J. Rutkauskaite, A. deMello, and S. Stavrakis, "High-throughput multi-parametric imaging flow cytometry," *Chem*, vol. 3, no. 4, pp. 588–602, Oct. 2017, issn: 24519294. doi: 10.1016/j.chempr.2017.08.005. [Online]. Available: https://linkinghub.elsevier.com/retrieve/pii/S2451929417303522 (visited on 01/13/2021).

[82] T. T. W. Wong, A. K. S. Lau, K. K. Y. Ho, *et al.*, "Asymmetric-detection time-stretch optical microscopy (ATOM) for ultrafast high-contrast cellular imaging in flow," *Scientific Reports*, vol. 4, no. 1, p. 3656, May 2015, issn: 2045-2322. doi: 10.1038/srep03656. [Online]. Available: http://www.nature.com/articles/srep03656 (visited on 01/13/2021).

[83] K. Goda, A. Ayazi, D. R. Gossett, *et al.*, "High-throughput single-microparticle imaging flow analyzer," *Proceedings of the National Academy of Sciences*, vol. 109, no. 29, pp. 11 630–11 635, Jul. 17, 2012, issn: 0027-8424, 1091-6490. doi: 10.1073/pnas.1204718109. [Online]. Available: http://www.pnas.org/cgi/doi/10.1073/pnas.1204718109 (visited on 01/13/2021).

[84] E. D. Diebold, B. W. Buckley, D. R. Gossett, and B. Jalali, "Digitally synthesized beat frequency multiplexing for sub-millisecond fluorescence microscopy," *Nature Photonics*, vol. 7, pp. 806–810, 2013. doi: https://doi.org/10.1038/nphoton.2013.245.

[85] P. Chen, X. Su, M. Liu, and W. Zhu, "Lensless computational imaging technology using deep convolutional network," *Sensors*, vol. 20, no. 9, p. 2661, May 6, 2020, issn: 1424-8220. doi: 10.3390/s20092661. [Online]. Available: https://www.mdpi.com/1424-8220/20/9/2661 (visited on 01/13/2021).

[86] J. K. Adams, V. Boominathan, B. W. Avants, D. G. Vercosa, F. Ye, R. G. Baraniuk, J. T. Robinson, and A. Veeraraghavan, "Single-frame 3d fluorescence microscopy with ultraminiature lensless FlatScope," *Science Advances*, vol. 3, no. 12, e1701548, Dec. 2017, issn: 2375-2548. doi: 10.1126/sciadv.1701548. [Online]. Available: https://advances.sciencemag.org/lookup/doi/10.1126/sciadv.1701548 (visited on 09/25/2020).

[87] C. F. Higham, R. Murray-Smith, M. J. Padgett, and M. P. Edgar, "Deep learning for real-time single-pixel video," *Scientific Reports*, vol. 8, no. 1, p. 2369, Dec. 2018, issn: 2045-2322. doi: 10.1038/s41598-018-20521-y. [Online]. Available: http://www.nature.com/articles/s41598-018-20521-y (visited on 01/18/2021).

[88] A. Kihm, L. Kaestner, C. Wagner, and S. Quint, "Classification of red blood cell shapes in flow using outlier tolerant machine learning," *PLOS Computational Biology*, vol. 14, no. 6, 2018, issn: 1553-7358. doi: https://doi.org/10.1371/journal.pcbi.1006278.

[89] D. Guera and E. J. Delp, "Deepfake video detection using recurrent neural networks," in *15th IEEE International Conference on Advanced Video and Signal Based Surveillance (AVSS)*, 2018, pp. 1–6. doi: https://doi.org/10.1109/AVSS.2018.8639163.

[90] T. Park, J.-Y. Zhu, O. Wang, J. Lu, E. Shechtman, A. A. Efros, and R. Zhang, "Swapping autoencoder for deep image manipulation," in *ArXiv*, https://arxiv.org/abs/2007.00653, 2020.

[91] J. Martin-Wortham, S. Recktenwald, M. Lopes, L. Kaestner, C. Wagner, and S. Quint, "A deep learning-based concept for high throughput image flow cytometry," en, *Applied Physics Letters*, vol. 118, no. 12, p. 123 701, Mar. 2021, issn: 0003-6951, 1077-3118. doi: 10.1063/5.0037336. [Online]. Available: https://aip.scitation.org/doi/10.1063/5.0037336.

[92] M. L. Heuzé, O. Collin, E. Terriac, A.-M. Lennon-Duménil, and M. Piel, "Cell migration in confinement: A micro-channel-based assay," in *Cell Migration: Developmental Methods and Protocols*, C. M. Wells and M. Parsons, Eds. Totowa, NJ: Humana Press, 2011, pp. 415–434, isbn: 978-1-61779-207-6. doi: 10.1007/978-1-61779-207-6_28. [Online]. Available: https://doi.org/10.1007/978-1-61779-207-6_28.

[93] V. Nair and G. Hinton, "Rectified linear units improve restricted boltzmann machines," in *Proceedings of the 27th International Conference on Machine Learning*, https://www.cs.toronto.edu/fritz/absps/reluICML.pdf, 2010.

[94] S. Ioffe and C. Szegedy, *Batch normalization: Accelerating deep network training by reducing internal covariate shift*, 2015. doi: 10.48550/ARXIV.1502.03167. [Online]. Available: https://arxiv.org/abs/1502.03167.

[95] D. Kingma and J. Ba, *Adam: A method for stochastic optimization*, 2014. doi: 10.48550/ARXIV.1412.6980. [Online]. Available: https://arxiv.org/abs/1412.6980.

[96] S. Ota, R. Horisaki, Y. Kawamura, *et al.*, "Ghost cytometry," *Science*, vol. 360, no. 6394, Jun. 15, 2018, issn: 0036-8075, 1095-9203. doi: 10.1126/

science.aan0096. [Online]. Available: https://www.sciencemag.org/lookup/doi/10.1126/science.aan0096 (visited on 01/13/2021).

[97] W. Jiang, X. Li, X. Peng, and B. Sun, "Imaging high-speed moving targets with a single-pixel detector," *Optics Express*, vol. 28, no. 6, pp. 7889–7897, 2020. doi: https://doi.org/10.1364/OE.387024.

Titel : Erforschung der Dynamik der Aggregation roter Blutkörperchen in der Mikrozirkulation: Ein Ansatz aus Physik und künstlicher Intelligenz

Zusammenfassung : Die Untersuchung der Eigenschaften und des Verhaltens roter Blutkörperchen (Erythrozyten) ermöglicht Einblicke in grundlegende Aspekte des Blutkreislaufs und in spezifische Erkrankungen wie die Erkennung von Entzündungen oder Sepsis anhand der Erythrozytensedimentationsrate, die eng mit der Aggregationsrate verbunden ist. Aufbauend auf dieser grundlegenden und klinischen Bedeutung untersucht diese Doktorarbeit die Erythrozyten in der Strömung in Kapillaren auf mikroskopischer Ebene.

Wir konzentrieren uns zunächst auf die Verteilung der Erythrozyten an einer in vitro-Mikroverzweigung unter Berücksichtigung des Einflusses der durch Dextran eingestellten Aggregationsraten. Experimentelle Untersuchungen zeigen, dass das Vorhandensein von Aggregation die inhomogene Verteilung von Erythrozyten verstärkt und den signifikanten Einfluss von Aggregationskräften auf den beobachteten Zweifach-Fung-Effekt hervorhebt.

Anschließend befassen wir uns mit der Entwicklung eines automatischen Formerkennungssystems für Erythrozyten, das optische Modulation und künstliche Intelligenz einsetzt, um Erythrozyten in der Strömung ohne komplexe Aufbauten zu erfassen. Durch die Verwendung einfacher Zell-Fingerabdrücke, die aus intensitätsmodulierten Signalen abgeleitet werden, die durch eine binäre 2D-Schlitzmaske erzeugt werden, wird eine Bildrekonstruktion von Erythrozyten im mikrofluidischen Fluss erreicht.

Title : Exploring the Dynamics of Red Blood Cell Aggregation in Microcirculation: A Physics and Artificial Intelligence Approach

Abstract: Examining the characteristics and behavior of red blood cells (RBCs) enables insights into fundamental aspects of blood circulation and specific disorders such the identification of inflammation or sepsis via the RBC sedimentation rate, a measure closely associated with aggregation rate. Building upon this fundamental and clinical significance, this doctoral work takes a multiphysics to study the RBCs in flow in capillaries at a microscopic scale.

We first focus on the distribution of RBCs at an \textit{in vitro} micro-bifurcation considering the influence of aggregation rates tuned by Dextran. Experimental investigations demonstrate that the presence of aggregation amplifies the non-homogeneous distribution of RBCs, highlighting the significant impact of aggregation forces on the observed Zweifach-Fung effect.

We then address the development of an automatic shape recognition system for RBCs, using optical modulation and artificial intelligence to capture RBCs in flow without complex setups. By utilizing simple cell fingerprints derived from intensity-modulated signals generated through a 2D binary slit mask, image reconstruction of RBCs in microfluidic flow is achieved.